

12-2015

Plasma catalysis using low melting point metals.

Maria Carreon

Follow this and additional works at: <http://ir.library.louisville.edu/etd>



Part of the [Chemical Engineering Commons](#)

Recommended Citation

Carreon, Maria, "Plasma catalysis using low melting point metals." (2015). *Electronic Theses and Dissertations*. Paper 2335.
<https://doi.org/10.18297/etd/2335>

This Doctoral Dissertation is brought to you for free and open access by ThinkIR: The University of Louisville's Institutional Repository. It has been accepted for inclusion in Electronic Theses and Dissertations by an authorized administrator of ThinkIR: The University of Louisville's Institutional Repository. This title appears here courtesy of the author, who has retained all other copyrights. For more information, please contact thinkir@louisville.edu.

PLASMA CATALYSIS USING LOW MELTING POINT METALS

By

Maria Carreon

B.S., Universidad Michoacana, MEXICO, 2007

M.S., Universidad Michoacana, MEXICO, 2010

A Dissertation

Submitted to the faculty of the

J.B. Speed School of Engineering

In Partial Fulfillment of the Requirements

For the degree of

Doctor of Philosophy in Chemical Engineering

Department of Chemical Engineering

University of Louisville

Louisville, Kentucky, 40292

December 2015

© Copyright 2015 by Maria Carreon

All rights reserved

PLASMA CATALYSIS USING LOW MELTING POINT METALS

By

Maria Carreon

B.S., Universidad Michoacana, MEXICO, 2007

M.S., Universidad Michoacana, MEXICO, 2010

A dissertation approved on

October 30, 2015

by the following Dissertation Committee:

Dissertation Director
Dr. Mahendra K. Sunkara

Dr. Thomas Starr

Dr. Bruce Alphenaar

Dr. Gamini Sumanasekera

Dr. Xiao-An Fu

DEDICATION

This dissertation is especially dedicated to my dear daughter Lucia which support was essential for complete successfully my PhD program. Thank you for your company during the long characterization sessions during the weekends!

Special thanks to my parents and my little sister Lupita for their continuous love and reinforcement.

I would like to acknowledge my two brothers: Guillermo and Moises, great engineers and professors who have been through all these years my role models and mentors. And which continuous guidance had taken me to follow their steps in to Academia.

Last but not least, I would like to give my deepest expression of love and appreciation to my dear husband Enrique for the encouragement that you gave and the sacrifices you made during this graduate program. Thank you for all the support!

ACKNOWLEDGEMENTS

First of all, I want to thank my advisor, Dr. Mahendra Sunkara for his valuable mentoring and support. Also many thanks to my committee members: Dr. Thomas Starr, Dr. Bruce Alphenaar, Dr. Gamini Sumanasekera and Dr, Xiao-An Fu for taking the time to carefully read this dissertation and making invaluable comments since it was presented as a proposal.

I would like to acknowledge all the lab mates I have been working with since joining the CVD lab, specially my good friend Apolo Nambo. Through the five years I spent in this lab, I was able to meet many people from whom I learned a lot, being a great enrichment experience for me. Thanks guys!

Special thanks to Dr. Jacek Jasinski, Dr. Arjun Thapa, Dr. Madhu Menon and Dr. Indira Chaudhuri for all the interesting discussions we had that help to improve the present work.

Last but not least, I would like to acknowledge Patty Lumley and Eunice Salazar for their patience and helped in the registration process and reminders of deadlines through all these years.

ABSTRACT

PLASMA CATALYSIS USING LOW MELTING POINT METALS

Maria Carreon

October 30, 2015

Plasma catalysis is emerging as one of the most promising alternatives to carry out several reactions of great environmental importance, from the synthesis of nanomaterials to chemicals of great interest. However, the combined effect of a catalyst and plasma is not clear. For the particular case of 1-D nanomaterials growth, the low temperatures synthesis is still a challenge to overcome for its scalable manufacturing on flexible substrates and thin metal foils.

Herein, the use of low-melting-point metal clusters under plasma excitation was investigated to determine the effectiveness in their ability to catalyze the growth of 1-D nanomaterials. Specifically, plasma catalysis using Gallium (Ga) was studied for the growth of silicon nanowires. The synthesis experiments using silane in hydrogen flow over Ga droplets in the presence of plasma excitation yielded tip-led growth of silicon nanowires. In the absence of plasma, Ga droplets did not lead to silicon nanowire growth, indicating the plasma-catalyst synergistic effect when using Ga as catalyst. The resulting nanowires had a 1:1 droplet diameter to nanowire diameter relationship when the droplet diameters were less than 100 nm. From 100 nm to a micron, the ratio increased from 1:1 to 2:1 due to differences with wetting behavior as a function of droplet size. The growth

experiments using Ga droplets derived from the reduction of Gallium oxide nanoparticles resulted in silicon nanowires with size distribution similar to that of Gallium oxide nanoparticles. Systematic experiments over 100 °C – 500 °C range suggest that the lowest temperature for the synthesis of silicon nanowires using the plasma-gallium system is 200 °C.

A set of experiments using Ga alloys with aluminum and gold was also conducted. The results show that both Ga rich alloys (Ga-Al and Ga-Au) allowed the growth of silicon nanowires at a temperature as low as 200 °C. This temperature is the lowest reported when using either pure Al or Au. The estimated activation energy barrier for silicon nanowire growth kinetics using Al-Ga alloy (~48.6 kJ/mol) was higher compared to that using either pure Ga or Ga-Au alloy (~34 kJ/mol).

The interaction between Ga and hydrogen was measured experimentally by monitoring pressure changes in a Ga packed batch reactor at constant temperature. The decrease of the pressure inside the reactor when the Ga was exposed to plasma indicated the absorption of hydrogen in Ga. The opposite effect is observed when the plasma is turned off suggesting that hydrogen desorbed from Ga. This experimental observation suggests that Ga acts as hydrogen sink in the presence of plasma. The formation of Ga-H species in the Ga surface and in the bulk as intermediate is suggested to be responsible for the dehydrogenation of silyl radicals from the gas phase and subsequently for selective dissolution of silicon into molten Ga. The proposed reaction mechanism is also consistent with the experimentally determined activation barrier for growth kinetics (~34 kJ/mol). In addition, theoretical simulations using VASP (Vienna Ab-initio Simulation

Package) were used to study atomic hydrogen – molten Ga interactions. The simulation results suggest significant interaction of atomic hydrogen with molten Ga through formation of Ga-H species on the surface and fast diffusion through bulk Ga while supporting the proposed model to explain the Plasma-Ga synergistic effect.

Finally, plasma synthesis of silicon nanotubes using sacrificial zinc oxide nanowire thin film as a template was investigated for lithium ion battery anode applications. The silicon nanotube anode showed high initial discharge capacity during the first cycle of 4600 mAh g^{-1} and good capacity retention (3600 mAh g^{-1} after 20 cycles). The silicon nanotubes preserved their morphology after cycling and the observed performance was attributed to the change in phase from nanocrystalline silicon hydrogenated (nc-Si:H) to amorphous silicon hydrogenated (a-Si:H) during lithiation.

This dissertation demonstrated the plasma synergism with molten metals during vapor-liquid-solid growth of silicon nanowires. A model based on atomic hydrogen interactions with molten metals under plasma excitation has been proposed and validated through systematic experimental studies involving Ga and its alloys with gold and aluminum and theoretical studies involving first principles computations. Finally, the plasma-Ga system has been used to grow successfully silicon nanowires on various technologically useful substrates at temperatures as low as $200 \text{ }^\circ\text{C}$.

TABLE OF CONTENTS

ACKNOWLEDGEMENTS.....	iv
ABSTRACT.....	v
LIST OF FIGURES.....	xiii
LIST OF TABLES.....	xxiv
CHAPTER 1. INTRODUCTION.....	1
1.1 Plasma catalysis for one dimensional materials.....	3
1.2 Plasma catalysis for important chemical conversion reactions.....	5
1.3 Objectives	6
1.4 Organization of this dissertation	7
CHAPTER 2. BACKGROUND.....	9
2.1 Plasma catalysis for 1-D materials: Catalyst assisted growth of nanowires.....	9
2.1.1 Plasma-catalyst synergistic effects.....	10
2.1.2 Plasma non-traditional catalyst metal synergistic effects.....	15
2.1.3 Bulk nucleation versus tip led growth.....	17
2.2 Plasma active gas phase combined with the use of non-traditional metals.....	19
2.2.1 The gallium-hydrogen interaction at high temperatures	19
2.2.2 Nitrogen-Gallium interaction in the presence of plasma.....	21
2.2.3 Plasma enabled dissolution of oxygen and nitrogen for nanowire growth...21	

2.2.4 Plasma effect on surface energy of low melting metals.....	23
2.3 Scalability of plasma systems for producing nanowires.....	24
2.4 Applications of 1-D materials for energy conversion and storage.....	26
2.4.1 Silicon nanowires in solar cells and lithium ion batteries.....	29
2.5 Plasma catalysis for energy and environmental problems.....	30
2.6 Summary.....	34
CHAPTER 3. EXPERIMENTAL METHODS AND CHARACTERIZATION TECHNIQUES.....	36
3.1 Plasma reactor setup and silicon nanowire synthesis experiments.....	36
3.2 Hydrogen absorption studies in low-melting metals with plasma	40
3.3 Synthesis of silicon nanotube thin films.....	41
3.4 Procedure for fabricating Li ion battery coin cells	43
3.5 Structural and electrochemical characterization.....	44
3.5.1 Structural characterization of silicon nanowires and nanotubes.....	44
3.5.2 Electrochemical characterization	45
CHAPTER 4. PLASMA-GALLIUM SYNERGISTIC EFFECT FOR THE GROWTH OF SILICON NANOWIRES AT LOW TEMPERATURE.....	46
4.1 Tip led growth of silicon nanowires using Ga.....	46
4.2 Bulk nucleation versus tip led growth of silicon nanowires at low temperatures.....	51

4.3 Silicon nanowire growth experiments at low temperatures using chloro-silane gas phase.....	52
4.4 Structural characteristics of the synthesized silicon nanowires.....	54
4.5 Growth kinetics of silicon nanowires using Ga clusters at their tips.....	59
4.6 Gibbs–Thomson effect.....	62
4.7 Kinetic models for the growth of silicon nanowires.....	64
4.8 Estimation of activation energy for nanowire growth.....	72
4.9 Diameter control of Si nanowires.....	77
4.10 Growth kinetics of silicon nanowires using reduced Gallia nanoparticles.....	81
4.11 Comparison between growth kinetics obtained with Gallium oxide particle and metallic gallium derived droplets.....	82
4.12 Summary.....	83
 CHAPTER 5. SYNERGISTIC EFFECTS OF GALLIUM ALLOYS FOR THE GROWTH OF SILICON NANOWIRES.....	 86
5.1 Synthesis of Silicon nanowires using Aluminum-Gallium alloy.....	86
5.1.1 Nanowire growth using Aluminum.....	86
5.1.2 The Aluminum-Gallium alloy.....	88
5.1.3 Growth of silicon nanowires using Al-Ga alloys.....	94
5.1.4 Growth kinetic analysis of the silicon nanowires synthesized using Al-Ga alloy	98

5.2 Synthesis of Silicon nanowires using Gold-Gallium alloy.....	100
5.2.1 Gold for nanowires growth.....	100
5.2.2 The Gold-Gallium alloy.....	101
5.2.3 Synthesis of silicon nanowires using Au and the Au-Ga alloy.....	106
5.2.4 Kinetic analysis of the silicon nanowires synthesized using Au-Ga alloy..	111
5.3 Segregation behavior of Ga alloys.....	116
5.4 Summary.....	119
CHAPTER 6. PLASMA-MOLTEN SYNERGISTIC EFFECTS.....	120
6.1 The absorption of hydrogen in Gallium.....	120
6.2 The GaN formation at 800 °C and 70 watts.....	125
6.3 First computational studies.....	127
6.3.1. Computational method.....	128
6.3.2 Model preparation and result discussion.....	132
6.4 The interaction of hydrogen with metals.....	135
6.5 Summary.....	139
CHAPTER 7. THE CAPACITY AND DURABILITY OF SILICON NANOWIRES AND AMORPHOUS SILICON NANOTUBE THIN FILM ANODE FOR LITHIUM ION BATTERY APPLICATIONS.....	140
7.1 Lithium ion battery technology and nanostructured silicon based materials.....	140

7.2 Synthesis and electrochemical characterization of silicon nanowire arrays grown on stainless steel substrates	144
7.3 Synthesis and electrochemical characterization of silicon nanotube thin films.....	146
7.4 Summary.....	162
CHAPTER 8. CONCLUSIONS.....	163
CHAPTER 9. RECOMMENDATIONS FOR FUTURE WORK.....	166
9.1 Plasma catalysis synthesis of ammonia.....	166
9.2 Synthesis of GaN crystals at low temperature and sub atmospheric pressure.....	170
REFERENCES.....	171
CURRICULUM VITAE.....	184

LIST OF FIGURES

Figure 1.1.1 Schematic of the proposed plasma-catalysis concept and its implications with both materials synthesis and chemical catalysis.

Figure 2.1.1 Schematic illustration of silicon nanowire growth using vapor-liquid-solid (VLS) mechanism. The SEM image is taken from reference²⁰.

Figure 2.1.2 Nanoparticle temperature and critical diameter as a function of the substrate temperature for thermal chemical vapor deposition (solid and dashed curves) and plasma enhanced chemical vapor deposition (dotted and dash-dotted curves). This figure is taken from reference⁴⁵.

Figure 2.1.3 SEM images illustrating high density of nucleation and growth of nanowires from micron sized, molten metal clusters of various low-melting point metals^{10,9}.

Figure 2.2.1 A schematic illustrating the concept of rapid plasma oxidation of metals in the presence of alkali salts for producing metal oxide nanowires.

Figure 2.2.2 SEM micrograph of the dumbbell morphology obtained using a three-step sequence involving a ‘no-nitrogen–nitrogen–no-nitrogen’ dosing sequence during growth⁵⁵.

Figure 2.3.1 Schematics illustrating different types of plasma assisted nanowire synthesis approaches⁷⁶.

Figure 2.3.2 Different production techniques for production of nanowires and the reaction time scales involved with them⁷⁶.

Figure 2.5.1 Comparison of basic steps involved in traditional catalysis and plasma catalysis.

Figure 3.1.1 Schematic of the experimental setup used for silicon nanowire synthesis experiments. The custom-designed reactor setup consists of a furnace and a quartz tube covered with external coils for RF plasma generation.

Figure 3.1.2 a) Calibration curves obtained for the substrate temperature (measured using an IR thermometer) as a function of the furnace temperature without plasma b) Calibration curve showing the substrate temperature as a function of the furnace temperature under plasma at a power of 70W.

Figure 3.2.1 Schematic of the experimental setup used for the pressure change studies with hydrogen absorption on molten metals as a function of plasma excitation.

Figure 3.3.1 (a) Schematic illustrating the procedure used for synthesis of silicon nanotubes: Substrate covered with ZnO nanowires; Si deposition onto ZnO nanowires; and Silicon nanotubes formation by removal of ZnO nanowire cores using a mixture of 2%H₂ in Ar. b) Cross-sectional SEM image of the silicon nanotube thin film c) Magnified image of cross-sectional SEM shown in (b).

Figure 4.1.1 a) SEM image of stair-like Si nanowires morphology with diameters > 200 nm grown at 335 °C; b) SEM image of straight Si nanowires with diameters < 200 nm grown at 370 °C; c) High magnification SEM image of a single staircase Si nanowire

morphology grown at 335 °C; d) TEM image of a silicon nanowire showing the gallium neck.

Figure 4.1.2 a), b), c) and d) SEM images of tip-led silicon nanowires grown at 335 °C furnace temperature, used for length measurements.

Figure 4.1.3 a), b), c) and d) SEM images of silicon nanowires grown at 335 °C for 30 min with plasma power of 70 W, 0.1 torr pressure, and 10 sccm of 2% SiH₄/H₂.

Figure 4.3.1 Low temperature experiments. a) SEM images of Si nanowires grown at 180 °C and b) 220 °C using KCl in the reactor chamber and gallium oxide nanoparticles previously reduced with H₂/Ar mixture.

Figure 4.3.2 a) SEM images of gallium droplets covered with a silicon layer observed in sample synthesized at a) 180 °C, 30min and b) 80 °C, 4h. Both samples were obtained in absence of KCl in the reactor chamber.

Figure 4.4.1 TEM images for samples obtained at 335 °C. a) Thin Si nanowire and b) high resolution images and the corresponding [110] zone axis diffraction patterns for a thick nanowire. The Si nanowire growth directions were determined to be (111).

Figure 4.4.2 a) and b) TEM images for Silicon nanowires grown on quartz substrate at 370 °C showing twinning; c) TEM image of a straight thin silicon nanowire grown at 370 °C showing sawtooth faceting; and d) TEM image of a bi-crystal Si nanowire grown at 335 °C, both crystal planes are in the (111) direction.

Figure 4.4.3 Raman peaks from selected Si nanowire samples growth on quartz substrates at different temperatures.

Figure 4.4.4 a) and b) TEM images of bulk nucleated silicon nanowires grown at 220 °C. c) High resolution TEM image. d) Diffraction pattern showing the polycrystallinity of the sample.

Figure 4.4.5 a) and b) SEM images of bulk nucleated silicon nanowires grown at 210 °C c) and d) TEM images of bulk nucleated silicon nanowires at the same temperature.

Figure 4.5.1. Droplet diameter to nanowire diameter ratio (a)-(f) SEM images showing the size of the gallium droplet increasing with respect to the Si nanowire diameter. The Ga droplet size to resulting nanowire diameter ratio varies from a 1:1 ratio for nanowires < 200nm to a 2:1 ratio for bigger nanowires. (g) Schematic representing the droplet diameter to nanowire diameter ratio.

Figure 4.5.2 Growth kinetics studies for silicon nanowires: a) Droplet diameter versus resulting nanowire diameter at different temperatures. b) Growth rate as a function of droplet diameters. c) Growth rate as a function of droplet diameter to nanowire diameter ratio at 400 °C. d) Growth rate as a function of nanowire diameter at various temperatures within 280°C- 470 °C range.

Figure 4.7.1 Schematic illustrating the various possible limiting processes during vapor-liquid-solid growth of silicon nanowires.

Figure 4.7.2 Mole balance for silicon nanowire growth using Gallium droplet at tip.

Figure 4.8.1 Arrhenius plot of growth kinetics as a function of temperature.

Figure 4.8.2 Arrhenius plots ($1/T$ vs $\ln(k)$) at constant nanowire diameter using metallic Ga a) 33nm. b) 38nm. c) 42nm. d) 50nm. e) 61nm. f) 71nm. g) 300nm.

Figure 4.8.3 Schematics illustrating the proposed mechanistic steps for silicon nanowire growth using Ga droplets: a) The Ga droplet acts as a hydrogen sink in the presence of atomic hydrogen by forming Ga-H; b) Dissolution reaction happening on the Ga droplet surface. The Ga-H species formed on the Ga droplet catalyzes the dehydrogenation of the silyl radicals on the surface of the molten Ga; c) Contact area of Ga droplets depending on their size; and d) Precipitation of Si nanowires from Ga droplets leading to one-dimensional growth.

Figure 4.9.1 Histogram showing the size distribution of gallium droplets formed from the reduction of Ga_2O_3 nanoparticles.

Figure 4.9.2 a) SEM image of resulting gallium droplets with reduction of Ga_2O_3 nanoparticles. b) SEM images of synthesized Silicon nanowires using the reduced Ga_2O_3 nanoparticles at a growth temperature of 400 °C.

Figure 4.9.3 SEM image of silicon nanowires synthesized using reduced Ga_2O_3 nanoparticles at growth temperatures of a) 450 °C, b) 380 °C, c) 300 °C and d) 200 °C.

Figure 4.9.4 EDX analysis of a silicon nanowire synthesized at 380° C using Ga_2O_3 reduced nanoparticles.

Figure 4.10.1 Arrhenius plot of growth kinetics as a function of temperatures obtained using Ga_2O_3 at constant diameters a) 24nm, b) 38nm, c) 48nm, d) 70nm and e) 123nm.

Figure 4.11.1 Arrhenius plot of growth kinetics as a function of temperature for nanowires with diameters less than 200nm at different temperatures and using Ga droplets of different sizes: a) 33nm, b) 38nm, c) 42nm, d) 50nm, e) 61nm and f) 71nm.

Figure 5.1.1 Al-Si binary phase diagram

Figure 5.1.2 Al-Ga binary phase diagram.

Figure 5.1.3 Optical photographs of a) Al-Ga alloy and b) Ga films on different substrates.

Figure 5.1.4 SEM image of the Al-Ga alloy droplets on a quartz substrate after a treatment with H₂ plasma at 400 °C and 30min.

Figure 5.1.5 a) SEM image of an Al-Ga film on a quartz substrate, b) Elemental mapping for Al and Ga in the film.

Figure 5.1.6 Spatial EDAX mapping for Al and Ga elements over an Al-Ga alloy droplet.

Figure 5.1.7 SEM images of silicon nanowires synthesized at different temperatures using the Al-Ga alloy: a) 600 °C, b) 550 °C, c) 500 °C and d) 400 °C.

Figure 5.1.8 SEM images of silicon nanowires synthesized using an Al-Ga alloy at a) 300 °C and b) 200 °C.

Figure 5.1.9 EDX analysis of an Al-Ga droplet of a silicon nanowire synthesized at 500 °C.

Figure 5.1.10 Arrhenius plot for growth kinetics as a function of temperature for silicon nanowires with different diameters grown using Al-Ga alloy droplets.

Figure 5.2.1 Au-Si binary phase diagram.

Figure 5.2.2 Au-Ga binary phase diagram.

Figure 5.2.3 SEM image of the Au-Ga alloy droplets formed after exposure to hydrogen plasma at 400° C for 30min.

Figure 5.2.4 Spatial EDAX mapping for Au and Ga elements over an Au-Ga alloy droplet.

Figure 5.2.5 SEM images of different substrates heated at 400 °C a) Au-Ga alloy exposed to plasma, b) Au-Ga without plasma exposure, c) Au exposed to plasma and d) Au without plasma exposure.

Figure 5.2.6 SEM images of samples covered with Au after they were heated without the use of plasma but using SiH₄ at a) 500 °C, b) 700 °C, and c) 700 °C higher magnification image of (b).

Figure 5.2.7 SEM images of silicon nanowires synthesized using the Au-Ga alloy and 70W of plasma at a) 450 °C, b) 380 °C, c) 250 °C and d) 200 °C.

Figure 5.2.8 TEM-EDS line profile analysis of nanowire tip showing the presence of gold.

Figure 5.2.9 Arrhenius plot of growth kinetics as a function of temperature for silicon nanowires of different sizes a) 24nm, b) 30nm, c) 41nm, d) 51nm and e) 115nm for the Au-Ga alloy.

Figure 5.3.1 Schematics illustrating segregation behavior of phases in various Ga alloys.

Figure 6.1.1 Pressure change in the reactor as a function of time when a) the reactor chamber was packed with clean capillaries b) the reactor chamber was packed with capillaries covered with Ga when using hydrogen at 300 °C and 70 W.

Figure 6.1.2 Pressure change as a function of time when using hydrogen and capillaries covered with Ga in the presence of plasma at a) 70 watts, b) 140 watts. Pressure change as a function of time when using nitrogen and capillaries covered with Ga in the presence of plasma at a) 70 watts, b) 140 watts.

Figure 6.1.3 Milimoles of hydrogen absorbed at different temperatures when using a) 70 watts and b) 140 watts.

Figure 6.1.4 Milimoles of nitrogen absorbed at different temperatures when using a) 70 watts and b) 140 watts.

Figure 6.2.1 Pictures showing a) the reactor using nitrogen plasma, b) the quartz substrate covered with a thick Gallium film after plasma exposure and c) quartz tube after plasma exposure.

Figure 6.2.2 a) XRD diffraction pattern for the GaN film formed at 800 °C, 70 watts and 1.2 torr, b) SEM image of the formed GaN film.

Figure 6.3.1 Simulation results for hydrogen activity in Ga using VASP program at 300K and 600K.

Figure 6.3.2 (a) Left side image showing liquid gallium at 0K and right side image showing hydrogenated molten gallium system at 300K (b) Left side image showing

liquid gallium at 0K; right side image showing hydrogenated molten gallium system at 600K.

Figure 6.3.3 (a) and (b) Mean square displacement plots for gallium and hydrogen atoms at 300K. (c) and (d) Mean square displacement plots for gallium and hydrogen atoms at 600K.

Figure 6.4.1 Schematic illustrating recombination of atomic hydrogen on the Ga surface and in the bulk as a means of reduction of the total number of moles.

Figure 7.2.1 SEM images of silicon nanowires on stainless steel for lithium ion batteries a) before cycling and b) after cycling.

Figure 7.2.2 a) Charge-discharge curves of Silicon nanotube thin films at the voltage range of 2.2 V-0.002V with a current of 100 mA/g. b) Discharge capacities versus cycle number of Silicon nanotube thin film at the voltage range of 2.2 V-0.002V with a current of 100 mA/g.

Figure 7.3.1 a) A SEM image of ZnO nanowires used as sacrificial template. b) A SEM image of ZnO nanowires covered with Si film. c) A SEM image of Si nanotubes after ZnO nanowires removal for 2 hours d) A SEM image of silicon nanotubes after removal of ZnO core using a mixture of 2% H₂ in Ar for 5 hours at 600 °C.

Figure 7.3.2 a) and b) SEM images of silicon nanotubes showing silicon nanotubes connected to each other.

Figure 7.3.3 a) Charge-discharge curves of Silicon tube at the voltage range of 2.2-0.2 V with current density of 100 mA/g. b) Capacities vs. cycle number of silicon tube electrode at the voltage range of 2.2-0.2 V with current density of 100 mA/g for the sample of 2 hours removal.

Figure 7.3.4 Raman spectra for zinc oxide nanowires covered with Si without removal step and typical Raman spectra for a sample treated 5 hours with a mixture of H₂/Ar for nanowire removal.

Figure 7.3.5 Raman spectra of nc-Si:H nanotubes films. a) Before cycling b) After cycling.

Figure 7.3.6 a) First charge-discharge curves of silicon tube at 0.024C. b) Discharge capacities versus cycle number of silicon tube at a current of 100 mA/g c) Discharge capacities versus cycle number of silicon tube at different rate of 500mA/g, 1000mA/g, 2000mA/g, 4200mA/g d) Cyclic voltammetry of silicon tube at the scan rate of 1mV/s.

Figure 7.3.7 Coulombic efficiency as a function of cycles for silicon nanotube thin films.

Figure 7.3.8 Zinc oxide nanowires covered with silicon a) Charge discharge curve of zinc oxide nanowires covered with silicon at voltage range of 2.2-0.002 V with current density of 100 mA/g. b) SEM image showing the Zinc oxide nanowires covered with silicon.

Figure 7.3.9 a) and b) TEM images of silicon nanotubes after cycling c) and d) compositional line profile analysis.

Figure 9.1.1 Adsorption of hydrogen and nitrogen in gallium measured by pressure changes in the reactor chamber at a) 400 °C and 140 W, b) when there is no gallium in the reactor chamber.

Figure 9.1.2 Schematic of the proposed set up for ammonia reaction using plasma catalysis.

LIST OF TABLES

Table 2.1.1 List of typical catalytic metals and synthesis temperatures used for VLS growth.

Table 2.1.3 Summary listing non-catalytic metals and the synthesis temperatures used for nanowire growth under plasma activation. No nanowire growth is observed without using plasma activation for gas phase.

Table 2.4.1 Properties and applications of 1-D nanostructures

Table 2.5.1 State of the art of partial oxidation reaction of CH_4 to produce H_2 using plasma.

Table 4.8.1 Proposed surface and bulk reactions happening in the gallium droplet.

Table 5.1.2 Compositions of the liquid and solid phases formed at different temperatures from the 70 wt% Ga and 30 wt% Al alloy.

Table 5.1.10 Activation energy values obtained for silicon nanowire growth using the Al-Ga alloy.

Table 5.2.1 Compositions of the liquid and solid phases formed at different temperatures from the 70 wt% Ga and 30 wt% Au alloy.

Table 5.2.2 Activation energy values obtained for silicon nanowires grown using Au-Ga alloy as a function of nanowire diameters.

Table 5.2.3 Summary of the silicon nanowire growth temperatures and kinetics obtained in this work compared with that from literature.

Table 5.3.1 Surface tension values for Gallium, Aluminum and Gold.

Table 7.3.1. State of the art of silicon nanostructures as anodes in LIBs.

CHAPTER 1

INTRODUCTION

There are several grand challenges in energy conversion and storage technologies that require transformational advances in the discovery of new materials and processes. Specific examples include: 1) Efficient catalytic processes for reactions with tremendous impact on the environment and food production include carbon dioxide reduction and synthesis of ammonia; 2) Catalytic processes for conversion of electricity to chemicals for large scale storage; and 3) Scalable manufacturing of functional nanoscale materials such as nanowire arrays on thin metal foils and/or plastic substrates for cost effective production of energy conversion and storage device technologies.

Typically, the use of catalytic metals had allowed the synthesis of 1-D nanomaterials such as nanowires using a method known as vapor-liquid-solid (VLS) by the dissociative dissolution of precursors at temperatures higher than the respective eutectic temperatures for the catalytic metals. However, the use of high temperatures, typically needed with this method, limits the use of such traditional approaches toward large scale manufacturing. A promising approach for achieving the low temperature synthesis for 1-D nanostructures is the combined use of a low melting point metal and plasma. In this case, the low temperature synthesis can be achieved by the capacity of the low melting point metal to form a eutectic with the precursors at low temperature and the plasma ability to dissociate the gas precursor. The combined effect of the presence of

these two essential elements, a metal and plasma excitation, is termed here as plasma catalysis. However, the beneficial effect of plasma excitation and low-melting metals such as Ga and its alloys has not been understood. If understood properly, this process could be used for growing 1-D materials over large areas at low temperatures on various substrates.

In addition, the plasma catalysis scheme describe here using low-melting metals could be used for addressing other grand challenges with energy-environment and energy-food security nexus. CO₂ is a greenhouse gas that contributes to the climate change. If captured, it could be utilized by reducing it to precursors or chemicals of common use. However, to date, there is no effective and selective catalyst known to perform the CO₂ reduction reaction. On the other hand, the use of ammonia as precursor for fertilizers and building block for the synthesis of pharmaceuticals make this chemical of great interest but its synthesis process needs to be improved. The production of ammonia is accomplished using the Haber-Bosch process which requires high pressures and temperatures making it energy intensive.

In this dissertation, plasma catalysis involving low-melting metals is proposed as the plasma catalysis scheme generically for addressing various materials growth and catalytic processes. See the schematic in Figure 1.1.1. Even though, the use of a metal and plasma combined had been applied to improve catalysis of reactions of great interest such as the hydrogen production, this area still needs a transformational change. Fundamental understanding of the interaction of excited species with the metals used can enable rational design of processes involving plasma-catalysis. Greater understanding of

plasma-metal synergistic effect is needed within the context of silicon nanowire synthesis using low-melting metals. It is hoped that the resulting insight into the mechanistic understanding of plasma-catalyst could provide a basis for the application of such plasma catalysis technique for other applications such as chemical reactions of great importance as indicated in Figure 1.1.1.

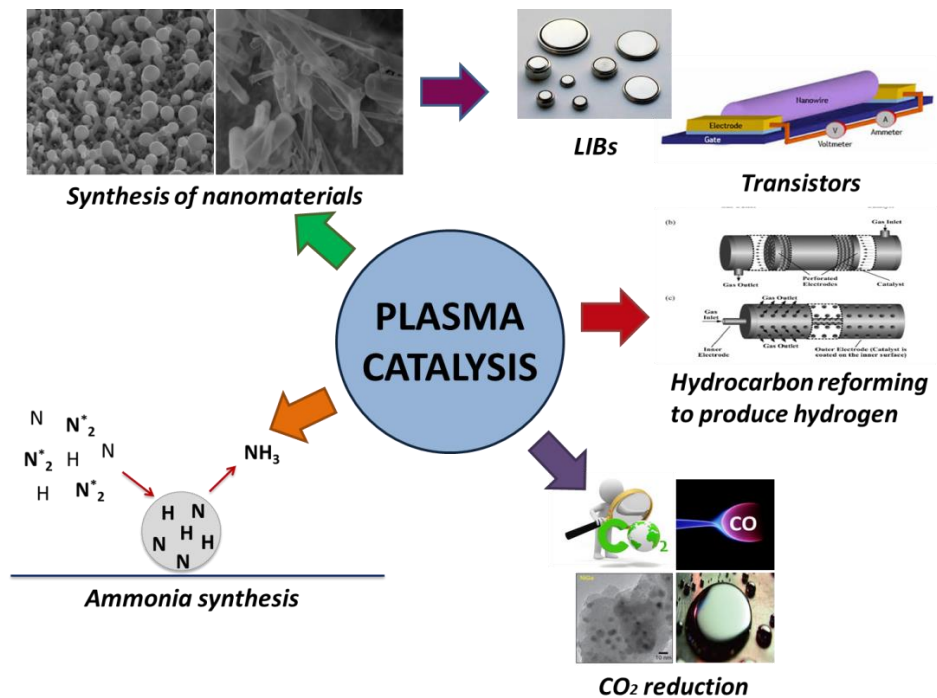


Figure 1.1.1 Schematic of the proposed plasma-catalysis concept and its implications with both materials synthesis and catalyzing chemical reactions.

1.1 Plasma catalysis for one-dimensional materials

The use of catalytic metals such as gold and related materials allowed the synthesis of nanowires through selective dissolution when performed at temperatures much above their eutectic temperatures. The use of plasma over catalytic metal clusters has been shown to reduce synthesis temperatures to near or below the eutectic

temperature. It has been demonstrated that the role of the plasma when using catalytic metals is to increase significantly the growth rate¹, and as mentioned before, the growth of nanowires can be achieved at significant lower temperatures than using similar neutral gas-based processes². Gold is thought as the catalytic metal required for the VLS growth of nanowires to happen^{3, 4, 5, 6}. However, gold is a deep level impurity in silicon and introduces electronic states in the band gap degrading the carrier mobility. Furthermore, it is not possible to achieve the growth of silicon nanowires at temperatures lower than 380 °C even with the use of plasma. As a consequence, it is expected that the use of alternative metals with low eutectic temperatures can allow particularly the synthesis of silicon nanowires at low temperatures. Gallium forms eutectics with silicon at temperatures as low as 29 °C⁷. However, in comparison with highly catalytic metals such as gold, gallium is not catalytic for the selective dissolution kinetics for silicon nanowire growth. Thus, in order to make the silicon nanowire growth possible using gallium, it has been shown that the presence of high density hydrogen radicals can assist the synthesis^{8,9,10}. Another important difference with low melting point metals such as gallium is the considerably low solubility of silicon and related materials. Such low solubility has been attributed to nucleation of multiple nanowires from single Ga droplet. Multiple nanowires have been observed to grow out of a metal droplet in the case of molten metals, such as gallium^{11, 12, 9} and indium¹³. Thus, to achieve the growth of one nanowire with a gallium droplet at its tip –‘tip-led’ growth- at low temperatures it is necessary to avoid the supersaturation of the gallium droplet in the initial stages.

Even though the plasma synergism with catalytic metals has been observed in several hydrocarbon reforming reactions using catalytic metals^{14,15,16} a complete understanding of this effect in low melting point metals has not been addressed yet. Preliminary data on the growth of silicon nanowires using gallium in the presence of plasma suggests that there is some sort of plasma-catalyst synergic effect. Under the presence of plasmas, low melting point metals that are not catalytic under typical conditions, have a synergistic interaction with plasma that allows them to behave as hydrogen sinks, that leads to the formation of hydrogenated metallic species that will mediate the growth reaction at very low temperatures. It is also of great interest to understand whether such synergistic effects could be exploited for other reactions and also in designing catalysts for plasma environments.

1.2 Plasma catalysis for important chemical conversion reactions

Plasma itself has allowed performing reactions of great interest. However, the necessity of a suitable catalyst is still a major need in order to improve the selectivity of these reactions. The use of only plasma for the breakage of the CO₂ molecules has already been reported¹⁷. Plasma reaction, which is based on non-equilibrium state, have shown the possibility to provide a less energy-intensive reduction path¹⁸. However, there is still the need of an appropriate catalyst to perform this reaction at moderate plasma conditions and with improved selectivity. In the case of the ammonia production reaction, when using traditional catalysis, is the dissociative absorption of nitrogen which imposes a major challenge. Nevertheless, in the case of plasma catalysis this situation changes completely. Recently, the use of plasma catalysis has emerged as a promising alternative

for the synthesis of ammonia at milder conditions. The non-equilibrium plasma approach allows the generation of NH radicals when using a N_2/H_2 mixture making possible to obtain ammonia. Besides, it has been observed an enhancement in the ammonia yield when the metal used as catalyst is placed in the plasma region which indicates a synergism between the catalyst and the plasma¹⁹.

1.3 Objectives

The overall objective of this dissertation is to study the synergistic impact of plasma activation with low melting point metals as ‘catalysts’ applied for vapor-liquid-solid growth of 1-D materials. A clear mechanistic understanding for one-dimensional growth of materials using plasma-catalysis involving low-melting metals can lead to the application of the basic concepts gained toward addressing several reactions of great technological and environmental interest. So, the main objective of this dissertation is to introduce the concept of plasma catalysis of low melting point metals for the growth of silicon nanowires.

Specific objectives of the dissertation include the following:

- a) The mechanistic understanding of plasma excitation of gas phase with the molten metals.
- b) The low temperature synthesis limit for silicon nanowires when using plasma catalysis approach along with Ga and Ga alloys.
- c) Demonstrate the use of the synthesized silicon nanowires as an interesting strain relaxation platform for lithium insertion and extraction for LIBs application

d) Development of an alternative conventional silicon nanostructure, such as silicon nanotubes, as anodes for lithium ion batteries at low temperature using plasma.

The specific deliverables of this dissertation are:

- (i) A clear insight of the synergism between plasma and Ga, a low melting point metal.
- (ii) The low-temperature limit for synthesis of silicon nanowires using synergistic effect between plasma-low melting metal catalyst.
- (iii) The development of a silicon nanostructure as anode for LIBs with potential scalability.

The outcomes of this dissertation have the potential to establish the plasma catalysis concept for both synthesis of one-dimensional materials and catalyzing several important reactions. The synthesis of Si nanowires at temperatures below 250 °C will enable scalable manufacturing of 1-D nanostructures on plastic substrates and thin metal foils.

1.4 Organization of this dissertation

This dissertation is divided into nine chapters. Chapter 1 introduces to the growth of silicon nanowires using metals as catalysts, the energy and material challenges that the plasma catalysis technique can potentially address and the need for the understanding and development of the proposed plasma catalysis concept.

Chapter 2 includes a detailed review of the plasma-catalysis for 1-D materials, particularly the VLS growth of nanowires. This review includes the use of plasma for nanowire growth with traditional and nontraditional metals. Also, this chapter discussed

the challenge for growing silicon nanowires at low temperatures and the state of the art approaches for addressing this challenge. Finally, the current status of plasma catalysis schemes for energy and environmental challenges is also reviewed.

Chapter 3 describes the experimental methods used for the synthesis of a) silicon nanowires using the plasma-catalysis approach, b) silicon nanotube thin films using plasma both at low temperature, c) the methodology used for measuring hydrogen absorption under plasma excitation, and d) characterization and testing techniques employed to evaluate the performance of the synthesized samples.

Chapter 4 discusses the results obtained with silicon nanowires using Ga catalyst in the presence of plasma. Chapter 5 describes the results obtained with silicon nanowire growth using Ga alloys with Au and Al.

Chapter 6 explores the gallium-hydrogen interaction in the presence of plasma by hydrogen absorption measurements. Also the nitrogen absorption measurements are presented in order to validate the possible use of Ga for the ammonia synthesis. Chapter 7 describes the capacity and durability of silicon nanowire array and amorphous silicon nanotube thin film anode in lithium ion battery applications. Chapter 8 presents the future work that can be done in order to address the limitations of the research presented in this dissertation. And finally Chapter 9 summarizes the main conclusions of this work.

CHAPTER 2

BACKGROUND

In this chapter, the basic principles involved with vapor-liquid-solid (VLS) approach for one-dimensional materials are discussed. Specifically a detailed review of the state of the art on plasma-catalyst synergistic effect on lowering synthesis temperatures for 1-D materials is presented. In addition to growing 1-D materials, a review of the use of plasmas and plasma catalysis concepts for important chemical reactions is provided.

2.1 Plasma catalysis for 1-D materials: catalyst assisted growth of nanowires

Catalysts are used for growth of one-dimensional materials both at micron and nanoscales using a mechanism known as Vapor-liquid-solid (VLS) originally proposed in 1964²⁰. This mechanism essentially consists of three main steps: (1) the catalytic dissolution of precursor species on the surface of a metal particle, (2) diffusion of the precursor through and/or on the surface of the catalytic particle and (3) nucleation and growth of the 1-D nanostructure. In order to catalyze the selective dissolution, it is common to use various catalytic metals such as Au^{5, 21, 22} and related materials. The synthesis is typically performed much above the eutectic temperatures to enable rapid mixing and diffusion through molten alloy. Other than gold, researchers have shown success with the use of catalytic metals such as Ni²³, Fe²⁴, Cu²⁵, Ag²⁶ and Co²⁷.

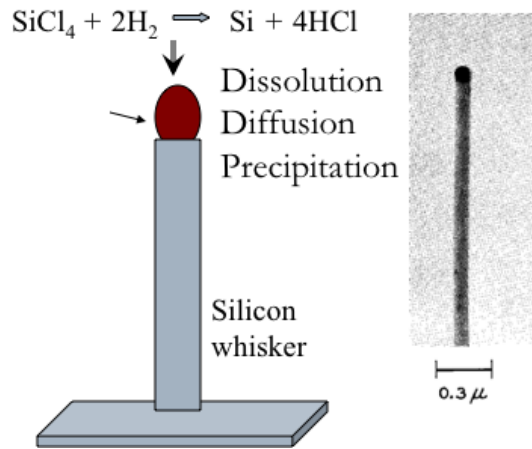


Figure 2.1.1 Schematic illustration of silicon nanowire growth using vapor-liquid-solid (VLS) mechanism. The SEM image is taken from reference²⁰

As shown in Figure 2.1.1, the silicon tetrachloride and hydrogen precursor gases react on gold cluster leading to selective dissolution of silicon into molten gold cluster. The alloying of silicon with gold leads to gold-silicon alloys whose melting point (eutectic temperature) is much less than those of both silicon and gold. The subsequent precipitation from gold-silicon alloy leads to one-dimensional growth of silicon. Typically, the synthesis temperature for crystalline silicon nanowires tends to be much above its eutectic temperatures anywhere from 550 °C – 900 °C using catalytic metals.

2.1.1 Plasma-catalyst synergistic effects

The use of plasma activation of gas phase over traditional catalytic metal clusters has been shown to reduce synthesis temperatures to near the eutectic temperature. This is the case of Au²⁸ where the synthesis temperature has been lowered to 380 °C when using PECVD . Also, the role of plasma along with catalytic metals is shown to significantly increase the growth rate, along with lowering synthesis temperature compared to those using neutral gas-based processes.^{2, 29, 30}

Despite the successful reduction in temperature when using gold clusters as catalysts and plasma, there exists a low temperature limit for the nanowire growth to happen. The main effects of plasma are ionization of gas phase precursors, creating radicals and selective heating of catalyst metal clusters through radical recombination³¹. In addition, the selective dissolution is also enhanced through enhanced adsorption onto catalytic metal surfaces. The low temperature limit is probably set by the diffusion through catalyst controls the nanowire growth kinetics.

Table 2.1.1 List of typical catalytic metals and synthesis temperatures used for VLS growth.

System used	Catalyst metal	Synthesis temperature traditional method	Eutectic temperature	Synthesis temperature plasma method	Plasma system used
Si	Au	550 °C-900 °C ⁵	363 °C	380 °C ²⁸	PECVD
Si	Au	1000 °C ³²	363 °C	380 °C ²⁸	PECVD
GaN	Au	960 °C ³³	~490 °C* ³⁴ *Au-Ga liquid phase when the alloy is rich in Ga	900 °C ³⁵	Dielectric barrier discharge (DBD)
GaN	Au	960 °C ³³	~490 °C* ³⁴ *Au-Ga liquid phase when the alloy is rich in Ga	850 °C ³⁶	PEHFCVD
GaN	Au	960 °C ³³	~490 °C* ³⁴ *Au-Ga liquid phase when the alloy is rich in Ga	900 °C ³⁷	DBD
InGaN	Au	----	----	700-750 °C ³⁸	PACVD
SiO _x N _y	Ni	----	963 °C* ³⁹ *Si-Ni eutectic	300 °C ⁴⁰	RF
GaN	Ni	900 °C ²³	895 °C* *Ni-Ga liquid phase	730 °C ⁴¹	Plasma assisted molecular beam epitaxy
Si	Fe	1000 °C ²⁴	1200 °C ⁴²	-----	Arc Plasma* ⁴³ *Formation of FeSi nanowires (autocatalized)
GaN	Co	800 °C-1050 °C ²⁷	~910 °C* ²⁷ *formation of miscible alloys of Ga-N-catalyst	-----	-----
Si	Ag	490 °C- 500 °C ²⁶	836 °C ²⁶	-----	-----

It is also important to understand various aspects of plasma activation on lowering the temperature required for growth using catalytic metal clusters. Ostrikov et al., pointed out that the temperature of the metallic alloy cluster during growth can be much higher than that of substrate holder due to heating by radical recombination and ion impact dissociation reactions. Such effects will allow for growth at much lower substrate temperature. In addition, Ostrikov and his co-workers gave important insight into the role of plasma activation on the minimum size of nanowire that can be grown compared to thermal chemical vapor deposition (Figure 2.1.2). Under plasma exposure, due to enhanced flux of vapor phase species through plasma sheath and higher dissolution, the supersaturation can be higher at much lower temperatures thus lowering the Gibbs-Thompson effect for lowering the size limit at temperatures lower than 600 °C.⁴⁴

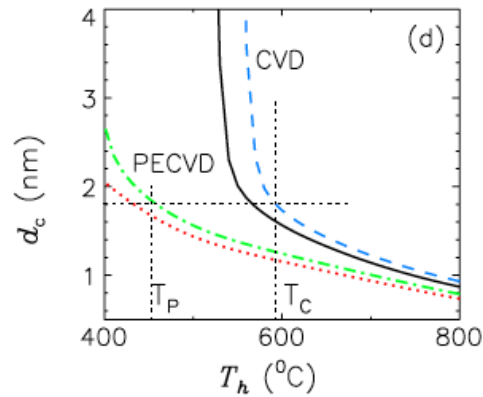


Figure 2.1.2 Nanoparticle temperature and critical diameter as function of the substrate temperature for thermal chemical vapor deposition (solid and dashed curves) and plasma enhanced chemical vapor deposition (dotted and dash-dotted curves). This figure is taken from reference⁴⁵.

See Figure for estimated temperature and critical diameters as function of substrate temperature for thermal CVD and PECVD.

The key attributes of plasma activation for nanowire synthesis include effective dissociation of the precursor gas phase to produce radicals and local heating temperature via radical recombination making the catalyst temperature higher than the average substrate temperature⁴⁶. It has been proposed that energetic surface reactions such as electron-ion recombination and other surface chemical reactions may lead to a considerable particle heating⁴⁷. The combined use of gold and plasma for the growth of silicon nanowires clearly result in the growth of this 1-D nanostructures at lower temperatures and higher growth rates than for the conventional neutral gas process.²⁸

For the growth of GaN nanowires using Au and plasma, one can use nitrogen instead of ammonia as precursor. This is mainly due to the active nitrogen species created by the plasma, which allow the growth to happen³⁷. Even further, the resulting nanowires are high quality single-crystal GaN nanowires. Also, the use of Au and plasma activation has been shown to result in high quality single crystal InGaN nanowires³⁸. Plasma activation of gas phase has been shown to be critical for producing SiO_xN_y compound nanowires. In the absence of plasma, one can only synthesize a-SiO_xH nanowires using any type of catalysts⁴⁰. The radical species involving both hydrogen and nitrogen are essential for synthesis of a-SiO_xN_y⁴⁸ nanowires in which hydrogen radicals keep the catalyst in the reduced form (avoiding oxidized version) and the nitrogen radicals allow for nitrogen incorporation in to the synthesized nanowires.

2.1.2 Plasma non-traditional catalyst metal synergistic effects

In the case of traditional catalyst metals, the use of plasma activation has been mainly to enhance the growth process in terms of growth kinetics, lowering growth temperature and reduce size limit and the use of different precursors. The use of plasma has been shown to be critically essential for growth of one-dimensional materials using non-traditional catalytic metals and systems. Or, in other words, the use of plasma has been shown to make many metals to work for synthesis of 1-D materials. Specifically, the metals such as Ga, In and Sn have been shown to work as catalysts for synthesis of silicon^{10,7}, germanium⁹ and other compound nanowires⁴⁹ through vapor-liquid-solid mechanism with the use of plasma activation. This is significant as many of these metals such as Ga, In and Sn make eutectics with Si and/or Ge at much lower temperatures than catalytic metals such as gold and iron. Specifically, Ga forms a eutectic with Si at $\sim 30^\circ\text{C}$ and it has a low solubility within Si at the eutectic temperature ($\sim 1 \times 10^{-8}$ at %). A peculiarity of these metals is that they are non-catalytic by nature which means that these do not promote the growth of 1-D materials at any temperature and pressure. In general, the growth of nanowires using non-catalytic metals in the presence of plasma has been observed and the following table summarizes various experiments involving non-catalytic metals and plasma methods.

Table 2.1.3 Summary listing non-catalytic metals and the synthesis temperatures used for nanowire growth under plasma activation. No nanowire growth is observed without using plasma activation for gas phase.

Materials System	Catalyst metal	Type of plasma	Metal vapor pressure (bar) @ 650 °C	Synthesis temperature (°C)	Eutectic temperature (°C)	Eutectic solubility (at. %)
Si	In	RF	$\sim 1 \times 10^{-4}$	240 ⁵⁰	156	2×10^{-10}
Si	In	RF		600 ⁵¹		
Si	In	RF		400 ⁵²		
GaN	In	MW		730-760 ⁵³		-----
Si	Sn	RF	$\sim 1 \times 10^{-8}$	300 ⁵⁰	232	1×10^{-7}
Si	Sn	RF		300-400 ⁵⁴		
Si	Sn	RF		380 ⁵⁴		
Ga ₂ O ₃	Ga	MW	$\sim 1 \times 10^{-6}$	450 ⁴⁹	30	-----
Si	Ga	RF		220 ⁵⁵		5×10^{-10}
Si	Ga	RF		500 -600 ⁵⁶		

For the case of GaN nanowires growth with In and plasma, it has been observed that there is an enhancement in the Ga diffusion which results in the suppression of the GaN 2D layer and subsequent cleaner surface⁵³. . Diffusion studies on the growth of GaN nanowires using Au and plasma have shown an interesting interaction between Ga and hydrogen plasma³⁷. It has been concluded that this interaction between hydrogen and gallium is responsible of the observed overall growth of nanowires by the absorption of hydrogen at the Ga surface. However, even though this interaction is not explained in

detail the solely existence of a synergism between Ga and hydrogen is a remarkable observation.

2.1.3 Bulk nucleation versus tip led growth

The low-melting metals such as Gallium also offer extremely low solubilities and low temperatures for eutectics for a number of solutes including silicon. Interestingly enough, such low equilibrium solubilities lead to interesting possibilities, i.e., formation of smaller sized nuclei for growth of multiple nanowires from a micron or sub-micron sized molten metal clusters¹⁰. Multiple nanowires have been observed to grow out of a metal droplet in the case of molten metals, such as gallium^{10,9} and indium⁵¹. This was explained using the estimation of nuclei size using classical nucleation theory using equation below⁷. The Au-Si forms a quasi-miscible system with 18.6 at% Si composition as the eutectic at 640K. The critical nucleus size is estimated to be greater than >200 nm for a supersaturated concentration of C ~33 at % at 1000 K. On the other hand, the Ga-Si system forms quasi-immiscible systems with silicon solubility at 10⁻¹⁰ at % at its eutectic temperature of ~300K). The critical nucleus size is estimated to be about 6 nm for a very small dissolved concentration of ~1 at % at 700 K. Such estimations of smaller nuclei even with modest dissolved concentrations indicate that one can produce high density of nuclei from micron sized molten metal clusters.

$$d_c = \frac{4\Omega V}{RT \ln S}$$
$$\ln S = \ln(C/C_\infty)$$

Figure 2.1.3 below shows several examples on bulk nucleation and growth of nanowires with a number of solutes from micron sized clusters of a number of low-melting-point metals. In the case of silicon and germanium, the experiments were performed using solid-liquid dissolution under plasma exposure. In the case of other experiments, the solutes were supplied through vapor phase but with plasma exposure. The plasma exposure in this case helps with many aspects: (a) maintain clean surface of molten metal cluster for surface energy necessary for promoting vertical growth of nuclei and (2) enhanced selective dissolution of solutes from the vapor phase specifically difficult ones such as nitrogen. The bulk nucleation can be explained as a consequence of rapid dissolution in the initial stages leading to supersaturation levels reaching those of spinodal limit which results in spontaneous nucleation.

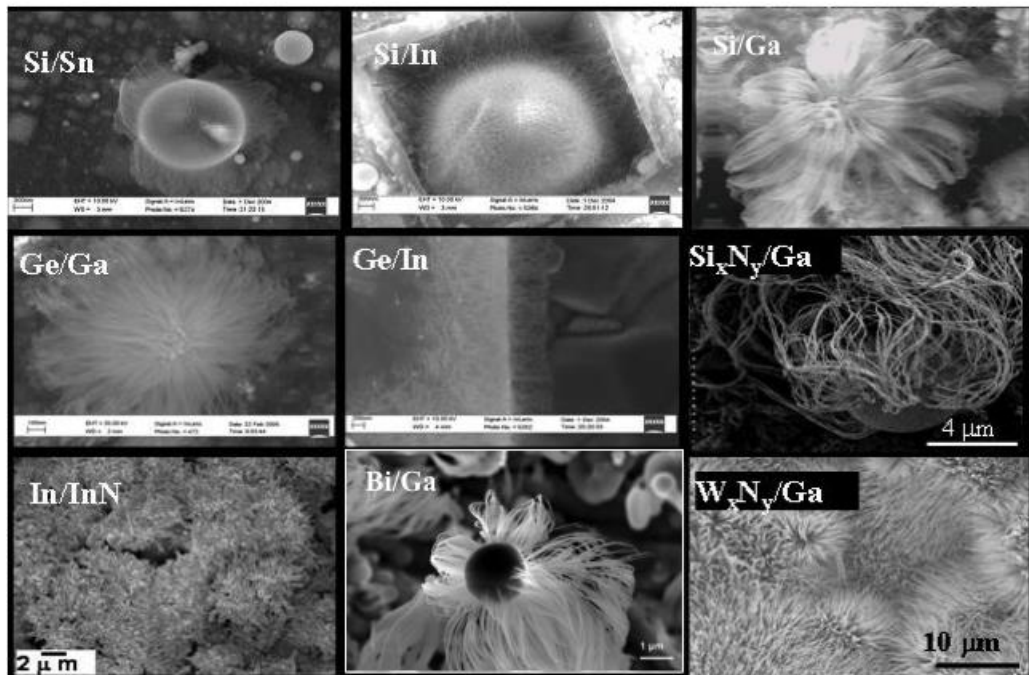


Figure 2.1.3 SEM images illustrating high density of nucleation and growth of nanowires from micron sized, molten metal clusters of various low-melting point metals ^{10,9}.

2. 2 Plasma active gas phase combined with the use of non-traditional metals

In addition to RF, Microwave and ECR plasmas, it is also possible to use hot-filaments to activate the gas phase for synthesis of nanowires using non-catalytic metals. Such is the case of silicon nanowires using Sn⁵⁷, In⁵⁸. In these reports, the metal is first evaporated on the substrate using a H₂ atmosphere, then SiH₄ is introduced into the chamber for the nanowire growth. For this approach, when using catalytic metals it has been observed that the hot filament process can be used as a very efficient source of atomic hydrogen which can be effectively used for the formation of small spherical metal nanoparticles that lead to the nanowire growth. Similar to other studies using plasma activated processes, the importance of hydrogen radicals for the growth of silicon nanowires is remarkable. In the case of silicon nanowires synthesized using Sn and plasma, it has been observed that the etching of tin seeds occurs parallel to the nanowire growth due to an interaction of Sn with the hydrogen active species generated by the plasma. In this case, it is possible to avoid the presence of the metal used for growth of nanowires at the end of synthesis and thereby avoiding an additional step to remove metal toward device integration⁵⁹.

Particularly, the above kind of synthesis with Sn is a clear example of the necessity of an active gas phase in order to conduct the nanowire synthesis when using non-traditional metals. The activated gas phase is similar to that of plasma chemistry.

2.2.1 The gallium-hydrogen interaction at high temperatures

The formation of Ga-H species has been observed as the result of the interaction of supported Ga catalysts with molecular hydrogen at high temperatures⁶⁰. Also, the

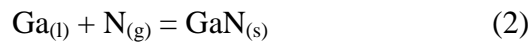
formation of gallium hydrogen species on the Ga₂O₃ surface at elevated temperatures has been reported. A clear understanding of the hydrogen adsorption is of great importance for the design of molecular sensors and alkane dehydrogenation-aromatization catalysts⁶¹. The GaH species on the Ga₂O₃ surface have been experimentally detected by FTIR (Fourier Transform infrared spectroscopy) and its formation had been attributed to the H adatom that binds the unsaturated Ga atoms⁶². The production of GaH species is favored at high temperatures since creation of the oxygen vacancies on the Ga₂O₃ increase with temperature.

The formation of Ga-H surface on GaN (0001) has been also a topic of intensive research in order to gain a better understanding of the GaN surface structure. In this case, it has been found that molecular hydrogen does not react with the GaN (001) surface while atomic hydrogen exposure results in the formation of surface Ga-H⁶³. The changes in the electronic structure of GaN (001) had been determined by electron-energy-loss spectroscopy (EELS), Auger electron spectroscopy (AES), and low-energy electron diffraction (LEED) as indicators of the surface Ga-H presence⁶⁴.

However, it is important to mention that the formation of the surface Ga-H species has been reported at high temperatures indicating that the interaction between Gallium and molecular hydrogen occurs only at high temperatures. The modeling of the hydrogen behavior in Ga stabilized δ -Pu at low temperatures, less than 300° C, has shown that the regions of high Ga concentration showed a dramatic decrease of the hydrogen diffusivity, and H atoms would never enter these regions⁶⁵.

2.2.2 Nitrogen-Gallium interaction in the presence of plasma

The synergistic effect plasma activation can be further understood through nitrogen dissolution into low-melting metals. Molecular nitrogen is usually a non-reactive gas under mild temperature and pressure conditions in neutral gas processes. Typically, one requires about 20 atm pressure and 2000K temperature for dissolving nitrogen into gallium melts using molecular nitrogen according to reaction (1). Using plasma activation of nitrogen, the dissolution into gallium melts is favored at sub-atmospheric pressures and temperatures as low as 850 °C according to reaction (2)^{66, 67}.



Also it has been concluded that the recombination of N to form N₂ is slowly enough to allow the formation of GaN⁶⁸. Such interactions have been exploited to grow GaN nanowires under self-catalyzed conditions using just nitrogen as precursor with the help of plasma.

2.2.3 Plasma enabled dissolution of oxygen and nitrogen for nanowire growth

As discussed above, the hydrogen radicals resulting from plasma can interact and dissolve in to molten metals. Similarly, the plasma excitation of gas phase also enables dissolution of both oxygen and nitrogen radicals into molten metals. In this case, the direct exposure of plasma excited gas phase over molten metals can result in respective oxide and nitride and oxynitride nanowires. The role of plasma excitation here is to enable rapid dissolution of solutes such as oxygen and nitrogen and keeping the surface

of molten metal clean for high surface energy. This concept has been exploited for synthesizing oxide nanowires of Zn, Ga, In, Al and nitrides of Ga, In, etc. In addition to oxidation or nitridation of low-melting metals, it is also possible to use plasmas for producing oxide nanowires from surfaces of high temperature metals^{45,69, 29}. This method consists in expose a thin metal foil to reactive oxygen plasma^{70, 71, 72}. The plasma surface reactions are a determining step for the nanowire growth in this case. The role of plasmas in this synthesis is to generate oxygen atoms in the gas phase through electron impact, also it provides localized surface heating through recombination of the dissociated oxygen atoms and ion bombardment and neutralization. Another method involving plasma oxidation of metals or respective oxides in the presence of alkali salts seems to result in nanowires with exposure time scales on the order of a minute or lower⁷³. The resulting alloys melt at lower temperatures resulting in a similar phenomenon of nucleation and growth of high density nanowires from molten alloys. This technique is similar to that of hydrothermal except that the plasma reduces the time scales from several days to minutes or lower. The actual mechanism of oxidation is expected to utilize oxygen radical in the case of plasma oxidation. See schematic illustration of the plasma oxidation of metals in the presence of alkali salts for nanowire growth.

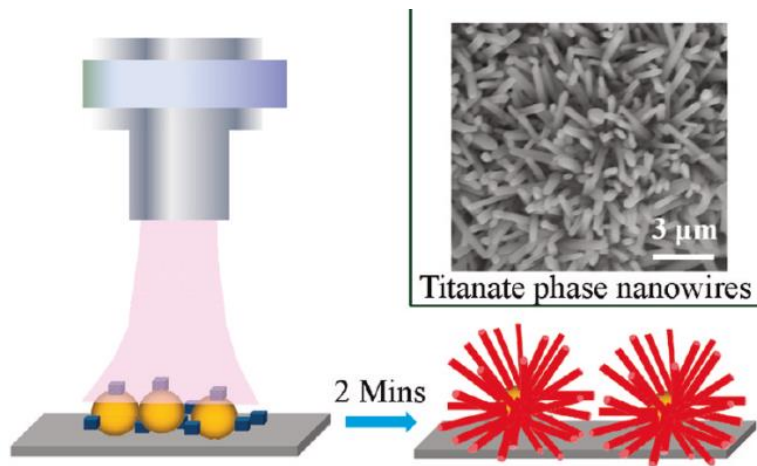


Figure 2.2.1 A schematic illustrating the concept of rapid plasma oxidation of metals in the presence of alkali salts for producing metal oxide nanowires.

2.2.4 Plasma effect on surface energy of low melting metals

The use of plasma activation has been shown to synthesize carbon from hydrocarbon gas phase selectively onto low-melting metals such Ga⁷⁴. The use of plasma activation with small amounts of oxygen and nitrogen has been shown to tune the surface energy and thus the wetting of Ga with growing carbon walls leading to morphological control⁷⁵. . See Figure 2.2.2 for schematic illustrating the carbon microtube morphology depends upon the wetting angle upon addition of oxygen or nitrogen in to gas phase under plasma activation. Under plasma exposure, the dissolution of oxygen or nitrogen into molten Ga cluster reduces the surface energy and this promotes wetting of molten Ga with growing carbon wall. The changes with wetting angle could lead to microtubes with straight and conical morphologies.

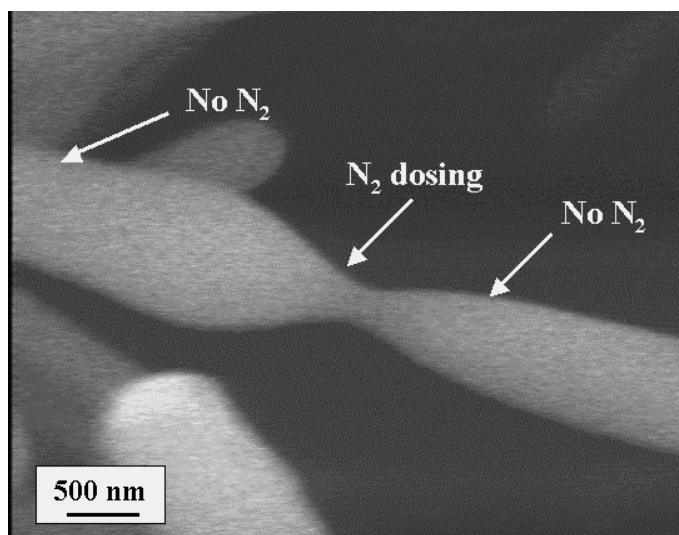


Figure 2.2.2 SEM micrograph of the dumbbell morphology obtained using a three-step sequence involving a ‘no-nitrogen–nitrogen–no-nitrogen’ dosing sequence during growth.⁵⁵

2.3 Scalability of plasma systems for producing nanowires

The plasma exposure systems for synthesis of nanowires can be categorized as the following⁷⁶: 1) PECVD, 2) Plasma-catalyst assisted, 3) Plasma flight-through⁷⁷ and 4) Direct plasma synthesis as depicted in Figure above. The time scales for all of the vapor phase techniques used for synthesis of nanowires are compared in the figure below. As shown, the time scales involving plasma exposure seem to be orders of magnitude better suggesting their use for scalable manufacturing. The bulk production of metal oxide and nanoparticles has been successfully reported by direct oxidation of micron-size metal particles using an atmospheric pressure microwave plasma⁷⁸. Typically, SnO₂, ZnO, TiO₂, and Al₂O₃ nanowires are synthesized by this technique. The production of these

nanostructures depends on the metal particle size, the microwave power and the composition of the gas phase.

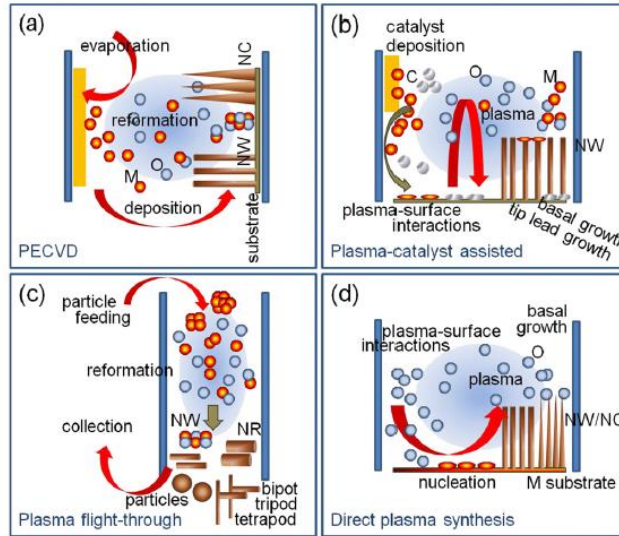


Figure 2.3.1 Schematics illustrating different types of plasma assisted nanowire synthesis approaches.⁷⁶

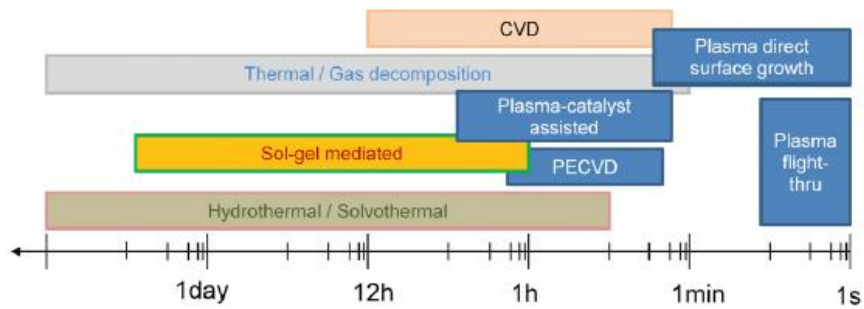


Figure 2.3.2 Different production techniques for production of nanowires and the reaction time scales involved with them.⁷⁶

2.4 Applications of 1-D materials for energy conversion and storage

Semiconductor nanowires and nanotubes have exceptional electronic and optical properties due to their unique structural one-dimensionality and the possibility of quantum confinement effects in two dimensions. Furthermore, the versatile compositions of these 1-D materials lead to a wide range of potential applications. Some of the important properties and applications of semiconductor nanowires are listed and briefly explained in the following paragraphs:

Light absorption and emission in a nanowire is highly polarization dependent⁷⁹. The polarization anisotropy in nanowires is due to the sharp dielectric contrast between the nanowire and its surroundings. Quantum-confined properties in one-dimensional nanostructures make them outstanding candidates for photovoltaic devices, such as photodetectors⁸⁰ due to their excellent electron transport properties. Furthermore, the small size and high surface-to-volume ratio of 1-D nanostructures allow them to have a variety of interesting and useful mechanical properties. They exhibit high toughness and strength for example, characteristics that allow them to be applied as nanoscale actuators, force sensors and calorimeters⁸¹. Another important application because of their very small size and weight is as nanomechanical resonators since they are theoretically capable of heat detection at the quantum limit and mass sensing at the level of individual molecules⁸².

A particular case is represented by the nanowires with flat end facets that have the potential to be exploited as optical resonance cavities to generate coherent light on the

nanoscale. UV lasing at room temperature has been demonstrated for several nanowire systems with epitaxial arrays⁸³ and single nanowires⁸⁴.

Another remarkable property of nanowires is the phonon transport, that is expected to be delayed in thin one-dimensional nanostructures that exhibit <100nm in diameter, as result of an increased boundary scattering and reduced phonon group velocities. Detailed models of phonon heat conduction in semiconductor nanowires have been developed predicting a large decrease of $\approx 90\%$ in the lattice thermal conductivity of these small diameter nanowires⁸⁵. This poor heat transport property results advantageous for thermoelectric materials applications, resulting in the fabrication of nanowires for these particular needs⁸⁶.

Electronic conductivity in semiconductor nanowires and nanotubes is another property that can be significantly enhanced by exposing these nanostructures to photons with energy greater than their bandgaps. The photoconductivity of certain nanowires could be exploited to create fast and reversible UV optical switches⁸⁷.

As it is expected, the magnetic properties of solids are size dependent, thus the magnetic behavior can be enhanced or even induced by reducing the system dimensions; such as the case of nanostructures. The main applications of this interesting property in the case of nanowires include: biological labeling⁸⁸, and high-density data storage⁸⁹.

An important characteristic of semiconductor nanowires that have been exhaustively studies are the quantum transport effects. These requires structures with widths comparable to the Fermi wavelength (tens of nm for semiconductors). The successful development of nanowire quantum devices depends mainly on the nanowire size control

and their device integration. Lieber group pioneered in the area of nanowire electronics with the fabrication of locally gated FETs⁸³, crossed-nanowire p-n junctions and LEDs⁹⁰, bipolar transistors and inverters⁹¹ and various logic-gate structures and memory elements⁹². However, these complex nanowire electronics cannot be produced economically with the available synthesis processes.

Finally, the ionic transport through nanoscale channels have recently gained attention due to the possibility of modulate ion currents during the passage of single DNA molecules⁹³. In this respect, nanotubes provide a unique high-aspect-ratio channel to study the ion transport and fluid flow. Theoretical nanotube studies⁹⁴ suggest that nanotubes with diameters smaller than the Debye length and applied gate bias can expel ions of like charge and produce unipolar solutions of counter ions within the channel.

Thus, the design of nanotube channels to imaging and manipulate single molecules as they pass through them is subject of great interest⁹⁵.

Table 2.4.1 summarizes the properties and applications of 1-D nanostructures described in the previous paragraphs.

Table 2.4.1 Properties and applications of 1-D nanostructures

Property	Application
Mechanical and thermal stability	Nanomechanical resonators
Nanowire lasing	UV lasing at room temperature
Phonon transport	Si and Si/Ge superlattice nanowires
Photoconductivity and chemical sensing	UV optical switches
Magnetic effects	Biological labeling and high density data storage
Electronic transport	Locally gated FETs, crossed wires p-n junctions and LEDs, bipolar transistors and invertors, logic gate structures and memory elements.
Ionic transport	Imaging and manipulation of single molecules

2.4.1 Silicon nanowires in solar cells and lithium ion batteries

Two applications of specific great interest for 1-D nanostructured based materials are solar cells and lithium ion batteries. In the case of solar cells, the direct electrical pathways provided by the nanowires, specifically silicon nanowires, ensure the rapid collection of carriers generated throughout the device, and a full sun efficiency reported to be 3.5% by Yang group⁹⁶, this is limited primarily by the surface area of the nanowire array.. The use of nanowires for solar cell applications have shown to have low transmission and photocurrent measurements and an increase in the path length of incident solar radiation by a factor of 73. This extraordinary light-trapping path length enhancement is superior to any other light-trapping methods. However for the scalability of the solar power energy using 1-D nanomaterials it is still required the reduction of its cost by the use of inexpensive substrates. The use of silicon nanowires for lithium ion batteries has been motivated by the high theoretical capacity of silicon that is 10 times higher than the existing carbon anodes. In addition to the advantage of a nanostructured morphology offers: facile strain relaxation, enhance power rate, efficient 1-D electron transport and good contact with current collector⁹⁷. However, there are still several challenges to overcome such as the formation of a stable electrode-electrolyte interface and the synthesis of these nanostructures on thin metal foils or flexible substrates.

The applicability of the above 1-D materials in to solar cells and LIBs depends greatly in making scalable manufacturing techniques that can work at low temperatures necessary for inexpensive and flexible substrates. Thus the low temperature synthesis of 1-D nanomaterials is a critical challenge to address.

Forthcoming challenges: The main challenge with 1-D based materials for storage and energy conversion and storage is with scalable manufacturing. For example, synthesis of nanowire arrays on very thin metal foils or on plastic substrates cannot be achieved using existing traditional techniques. In this dissertation, the use of plasma for the synthesis of silicon nanowires and silicon nanotubes at low temperatures is investigated in an effort to offer a possible cheaper and scalable alternative for the synthesis of these 1-D nanostructures on thin metal foils and plastic substrates.

2.5 Plasma catalysis for energy and environmental problems

Since early 1990s the application of plasma technologies in catalysis have been attracting an increase attention particularly, the use of plasma for the hydrocarbon reforming to generate H_2 . This mainly because H_2 is one of the most promising alternative energy sources since it is a carbon free energy carrier. Hydrogen as an energy source can be carbon neutral if produced from biomass and carbon free if it is produced from solar water splitting. Most importantly, hydrogen is compatible with fuel cell, a clean and highly efficient power generation device. The plasmas contain energetic electrons and a variety of chemically active species which can greatly promote the chemistry for reforming, however the H_2 selectivity has proven to be lower than the one achieved with traditional catalytic process for reforming⁹⁸ and its one of the present challenges of this technique to be industrial applicable. Recently, the plasma catalysis technique is emerging as a novel alternative that combines the high products selectivity from the thermal catalysis and the fast startup from the plasma technique. Till date, the main applications of plasma catalysis are the hydrocarbon reforming for hydrogen

production and the gaseous pollutant removal^{99, 100}. For hydrocarbon reforming, there is experimental evidence that there is a synergism between the catalyst and the plasma that results in high hydrogen yields at lower temperatures than the ones used with traditional catalysis¹⁴. One reaction that has been extensively studied using plasma chemistry for its simplicity is the partial oxidation of CH₄ to produce H₂. Based on the analysis, it has been confirmed that the plasma discharge could substantially influence the properties of the catalyst and its performance. However, up to date, the mechanism about how the plasma affects the catalyst is not yet clear. The most important results are summarized in Table 2.5.1 where the symbols ↑, ↓ and – stand for increase, decrease and no-change. In addition to the enhancement of hydrocarbon conversion and H₂ selectivity, it was observed that the presence of plasma effectively suppresses the coke deposition by about 15-55% compared when there is no plasma.

Table 2.5.1 State of the art of partial oxidation reaction of CH₄ to produce H₂ using plasma.

Catalyst (metal loading in wt %)	Plasma type	Method of plasma treatment	CH ₄ conversion	H ₂ selectivity	Coke formation	Ref
10% Ni/ α -Al ₂ O ₃	RF	Ar plasma, 1.5h (160W, 20 sccm)	↑	↑	↓	¹⁰¹
Ni-Fe/ γ - Al ₂ O ₃ Ni: 0.07%; Fe: 0.03%	DC	Ar plasma, 1h	↑	↑	↓	¹⁰² , ¹⁰³
0.5% Pt/ γ -Al ₂ O ₃	Glow	Ar plasma 10min	↑	—	↓	¹⁰⁴
5% Ni/ γ - Al ₂ O ₃ 10% Ni/ γ - Al ₂ O ₃	Corona	Ar plasma 4min (40kV, 20sccm)	↑	↑	↓	¹⁰⁵
10% Ni/ α -Al ₂ O ₃ 10% Ni/ γ - Al ₂ O ₃ 1% Pt/ α -Al ₂ O ₃ 1% Pt/ γ - Al ₂ O ₃	Di- electric barrier (DBD)	He plasma, 3min (60W, 45ml/min)	↑ ↑ ↑ ↑	— — — —	↓ ↓ ↓ —	¹⁰⁶

However, all these approaches have been done using typical catalytic metals and none is done using Low-melting metals that are known to be non-catalytic. In addition to hydrogen production, CO₂ reduction is another important reaction for energy-environment nexus¹⁰⁷. Our proposed system is a low-temperature plasma that is not in thermal equilibrium state which means that the electron temperature is around 1-10ev and is much higher than the gas temperature. From the plasma chemistry perspective the rotational and vibrational species are considered useless since they have short life times and low threshold energy, i.e. < 2eV thus, it is the electron impact dissociation and

ionization that is responsible for the molecule decomposition as it has been seen for hydrocarbons. Applying the same concept for the CO₂ reduction it is important to consider the elementary dissociation of the vibrationally excited CO₂ molecule which happens as follows:



This dissociation process results in the formation of an oxygen atom in the electronically ground state and requires the exact energy of an OC=O bond to be spent (530kJ/mol).

Contrasting the traditional catalysis versus the plasma catalysis approach, there is a clear reduction in the activation energy for this latter since the plasma chemistry offers the presence of excited species, radicals and positive/negative ions.

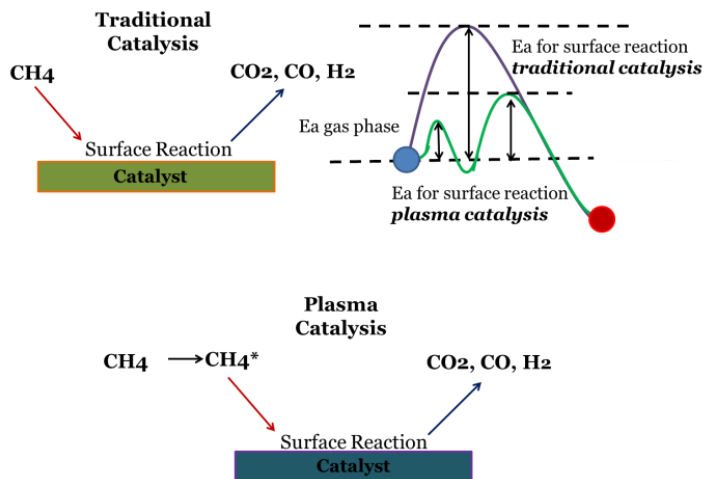


Figure 2.5.1 Comparison of basic steps involved in traditional catalysis and plasma catalysis.

Therefore the active species generated by the plasma change the gas-phase reactants state whereas the other two can affect the physical and chemical properties of the catalyst; however this last-mentioned phenomenon has not been addressed yet. The

CH₄ steam reforming reaction for H₂ generation which, as already mentioned it has been exhaustively studied^{108, 109, 110, 111, 112}. For this reaction, the enhancement of the dissociative adsorption of CH₄ on the catalyst is the rate limiting step, thus once this step is enhanced the overall reaction rate can be greatly increased. For the case of CH₄ dissociative adsorption enhancement several catalysts have been investigated in the presence of plasma such as: Ni¹¹², Pt¹¹³, Ru¹¹¹ and W^{108a}. All of them mainly conclude that methane molecules in vibrational state show much higher catalytic activity than those in ground state. In plasma chemistry reaction, the species in vibrational state are not that useful. However, when there is a catalyst in the plasma reactor, these species could assist thermal catalysis. Hence, there will be an energy efficiency enhancement. As a consequence one can expect that the working temperature of the catalyst might be reduced. Although there is no available data explaining how the combined effect of plasma and catalysts happen, the already mentioned evidence for this phenomena suggest that it is worth further investigation to get a clear insight into the interaction between plasma and catalysis.

2.6 Summary

As it can be seen, plasma catalysis is emerging as a new field leading to new alternative routes to solve grand material and energy challenges. Plasma catalysis not only offers a way for the synthesis of nanomaterials at low temperatures for energy storage and electronic applications. Plasma catalysis also has the potential to allow the synthesis of chemicals of great economic importance such as ammonia at mild conditions, resulting in a low production cost method.

Plasma catalysis has shown to have the capability to make possible the CO₂ reduction as well as the hydrocarbon reforming for H₂ production two reactions that keep being an environmental and energy challenge. These two reactions as described in this chapter present a huge energetic barrier, thus the use of plasma since it is based in a non-equilibrium state offers the possibility of a less energetic path. In addition to lower the energy requirements the use of plasma have shown to keep a clean catalyst surface ready to react as presented in the literature reviewed for this chapter.

In summary, the use of plasma is emerging as a new approach for the catalysis field both for growing 1-D materials and improving kinetics of chemical reactions. However there are many important fundamental concepts that need further understanding regarding the type of catalyst materials to be used in synergistic fashion with plasmas.

CHAPTER 3

EXPERIMENTAL METHODS AND CHARACTERIZATION TECHNIQUES

In this chapter, the experimental procedures used to perform plasma-catalysis experiments and also plasma based approach for producing silicon nanotubes thin films are discussed. The techniques for characterizing resulting materials are briefly explained. In addition, the fabrication of the Li ion batteries coin cells is described as well.

3.1 Plasma reactor setup and silicon nanowire synthesis experiments

The Si nanowire synthesis experiments were carried out in a custom-made, plasma-enhanced chemical vapor deposition reactor as shown in schematic in Figure 3.1.1. The setup consists of a tubular furnace and a quartz tube equipped with uniquely designed coils connected to RF power supply. The reactor is connected to a supply of silane, hydrogen and argon gases. Silicon, quartz and GaN substrates were used as substrates. In a typical experiment, the substrate was coated with a thin gallium film and then placed inside the furnace and heated to the chosen reaction temperature under vacuum at base pressure. In some experiments, the substrates were coated with Ga₂O₃ nanoparticles and then subjected them to hydrogen plasma for in-situ reduction to Ga droplets. The silicon nanowire synthesis experiments were performed using 2% SiH₄ in H₂ at 0.1 torr pressure, 70 W RF plasma power and at different temperatures ranging

from 100 °C to 500 °C. Typical duration of the experiments were anywhere from 15-30 minutes. Upon exposure to plasma, the molten gallium film formed sub-micron to millimeter-sized droplets on the substrates. In some experiments, KCl was placed ahead of the furnace in plasma to produce in-situ chlorosilanes and chlorine species in the gas phase at temperatures from 130 °C to 250 °C.

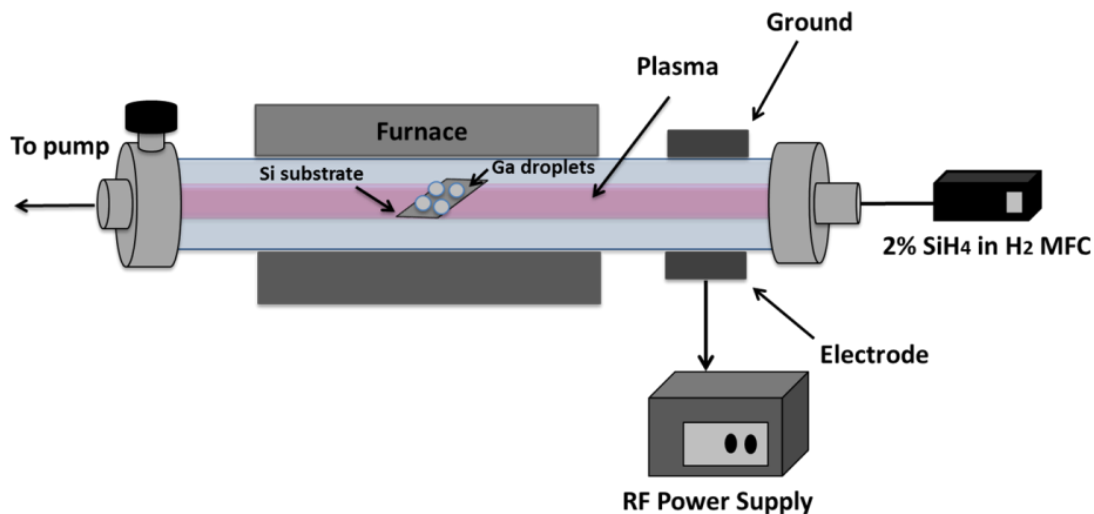


Figure 3.1.1 Schematic of the experimental setup used for silicon nanowire synthesis experiments. The custom-designed reactor setup consists of a furnace and a quartz tube covered with external coils for RF plasma generation.

The temperature of the substrates placed in quartz tube inside furnace can differ from the set furnace temperature due to improper thermal contact and non-equilibration of temperature with insufficient radiation at low temperatures. So, in each experiment, a substrate with an irreversible temperature record strip (Omega thermostrip DC irreversible temperature indicators) was also placed inside the quartz tube in order to measure the actual substrate temperature. Also, temperatures were measured using an IR

sensor (FLUKE 62 MAX, -30°C to 500 °C). The calibration data for substrate temperature with respect to furnace temperature is given in Figure 3.1.2. Under plasma exposure, the actual substrate temperature measured using both IR sensor and strip showed slightly higher values than that without plasma but still much lower than furnace temperature. The actual substrate temperatures measured using either IR sensor or using strips are reported as the growth temperatures in this study. The following graphs in Figures 3.1.2 (a) and (b) show the strips temperature versus the oven temperature and the IR thermometer temperature without plasma and with plasma power of 70W. The data in Figure 3.1.2 shows that there is a difference of ~ 60°C- 80°C between the furnace and the actual substrate temperature when the plasma is on at 70W. All the experiments for the synthesis of silicon nanowires were performed at 70 W, 12sccm of 2%SiH₄/H₂ and 0.1 torr. The only variable was the temperature, which was ranged from 100 °C to 500 °C.

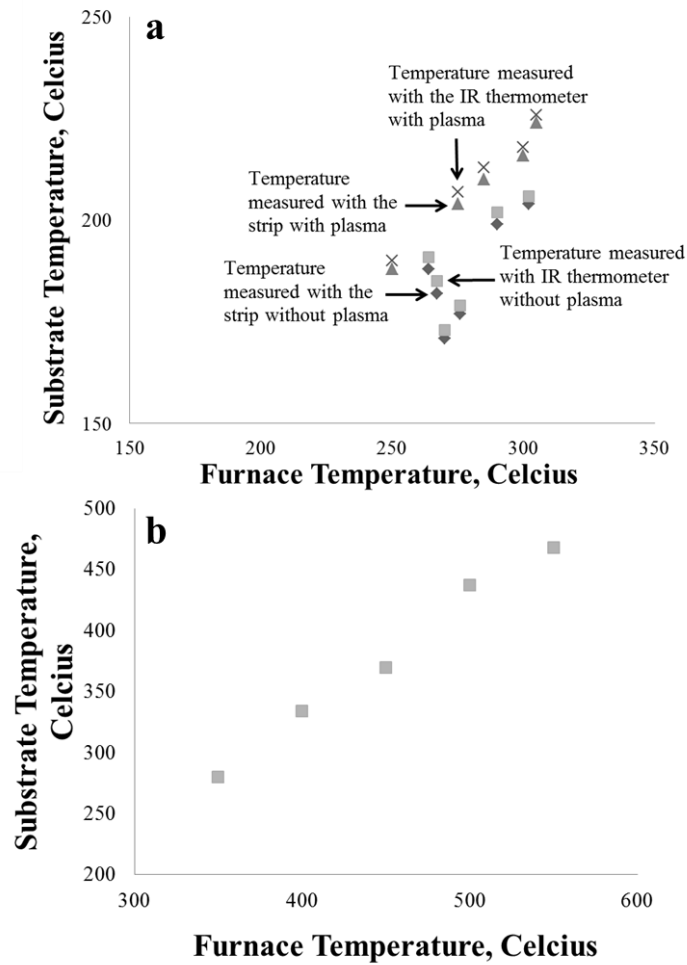


Figure 3.1.2 a) Calibration curves for the substrate temperature (measured using an IR thermometer) as a function of the furnace temperature without plasma b) Calibration curve showing the substrate temperature as a function of the furnace temperature under plasma at a power of 70W.

3.2 Hydrogen absorption studies in low-melting metals with plasma

The experimental setup was modified in order to transform the RF plasma reactor into a batch reactor where was possible to measure the change in pressure inside the chamber (Figure 3.2.1). The reactor chamber was packed with inert supports: quartz capillary tubes open both ends. The capillaries' outer walls were coated with metal Ga, the typical amount of Ga used was about 4 grams. It was used 1000 capillaries with an outer diameter of 0.54 mm and 100 mm in length. The surface area of all the capillaries used to pack the reactor is $\approx 0.17\text{m}^2$. The chamber was then filled with different gases such as hydrogen and nitrogen and the capillaries were exposed to plasma at constant temperature. The effect of plasma on gallium was investigated using plasma reactor in which quartz tube is packed with capillaries. The interaction of plasma excited gases with Ga is studied by observing pressure changes at various temperatures and two different powers: 70 W and 140 W.

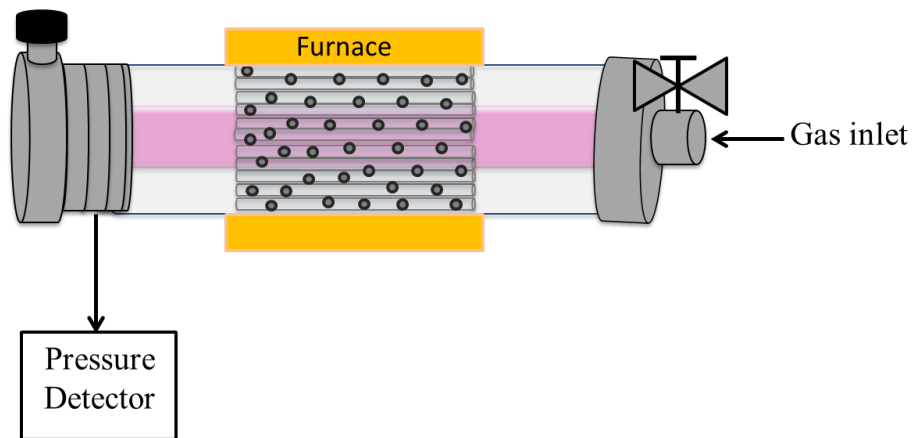


Figure 3.2.1 Schematic of the experimental setup used for the pressure change studies with hydrogen absorption on molten metals as a function of plasma excitation.

3.3 Synthesis of silicon nanotube thin films

Silicon nanotube thin films were prepared by silicon deposition on ZnO nanowire thin films templates followed by removal of ZnO nanowires. The silicon deposition was performed using the same RF PECVD reactor setup described in Section 3.1. The deposition experiments were performed at temperatures around 400°C or lower which is considerably lower than the temperature of 490°C employed in other reports¹¹⁴. The details of the synthesis process for Si nanotube thin films involved three main steps: 1) ZnO nanowire films were prepared on stainless steel substrates by dropcasting ZnO nanowire powder dispersion in acetone. ZnO nanowire powders were produced in another reactor described elsewhere⁷⁷. The ZnO nanowires with an average diameter of 50nm were used as the sacrificial layer. 2) The covered substrates were placed inside our custom-made reactor. Si deposition on ZnO nanowire thin films was done using a mixture of 2%SiH₄/H₂ at 400° C, 70W for about 30 minutes. 3) Finally, the selective removal of the ZnO nanowires was done using a mixture of 10%H₂/Ar and using just thermal oven at 600°C in-situ for over five (5) hours. Note, both duration and the required temperature can be drastically reduced using plasma activation and pressure in this step. For example, our previous studies have shown that atmospheric plasma based processes can reduce time scales from days to minutes⁷⁸. However, for studies conducted here, this is achieved using thermal process. This process step allowed the formation of silicon nanotubes opened from both sides. Figure 3.3.1(a) illustrates the overall 3-step procedure followed for the synthesis of the silicon nanotubes. Figure 3.3.1(b) shows the cross-sectional scanning electron microscope image of the resulting silicon nanotube film with an approximate thickness of 20 microns. Figure 3.3.1(c) shows magnified image of the Figure 3.3.1(d) indicating tightly packed silicon nanotubes into a thick film.

The process of making nanotubes using sacrificial templates results in a better size control of the resulting materials compared to alternatives such as supercritical hydrothermal synthesis¹¹⁵. Furthermore, the tube wall thickness can be controlled with adjusting the deposition time. We reported silicon nanotube thin film electrodes with 0.6 mg loading that exhibited an initial discharge capacity of 4766 mAh g⁻¹ and retained about 3400 mAh g⁻¹ after 20 cycles at 100 mA g⁻¹ rate. The silicon nanotube thin film samples with thicknesses ranging from 10-28 microns were prepared using silicon deposition on bulk produced zinc oxide nanowire films and subsequent removal of zinc oxide cores. The developed silicon nanostructures exhibit tubular geometry with both open ends. The nanotubes with thin walls are shown to accommodate large volume changes with lithiation and exhibit stable capacity retention. The synthesized silicon nanotubes are connected to each other forming a web-like network.

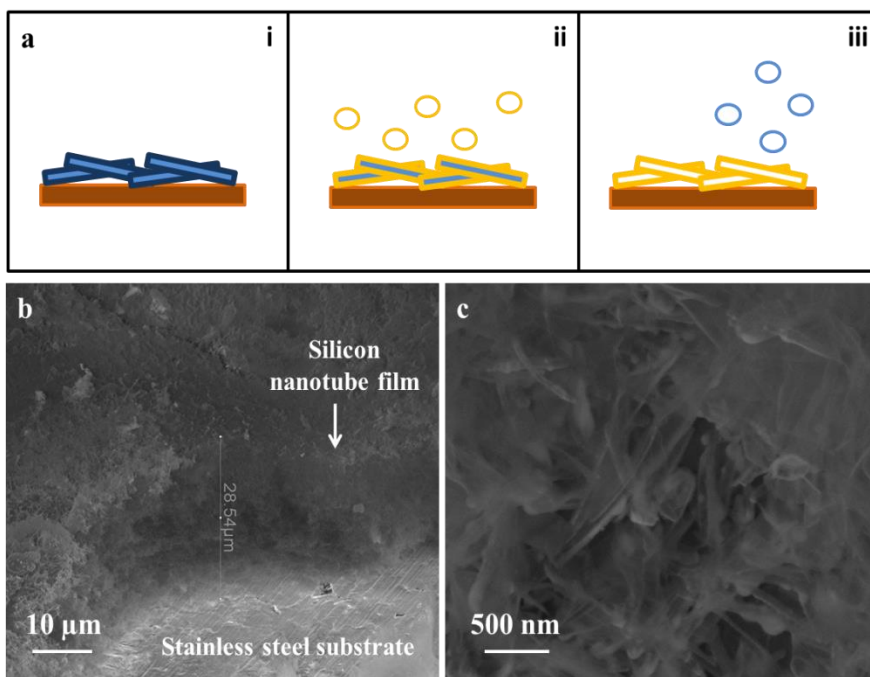


Figure 3.3.1 (a) Schematic illustrating the procedure used for synthesis of silicon nanotubes: Substrate covered with ZnO nanowires; Si deposition onto ZnO nanowires; and Silicon nanotubes formation by removal of ZnO nanowire cores using a mixture of 2% H_2 in Ar. b) Cross-sectional SEM image of the silicon nanotube thin film c) Magnified image of cross-sectional SEM shown in (b).

3.4 Procedure for fabricating Li ion battery coin cells

Electrode preparation: The test cell consists of a working anode electrode with Si nanotube thin films and a counter electrode made using lithium metal. No binders are used. The mass loading of active working electrode was 1.0~1.5 $mg\ cm^{-2}$.

Cell Assembly: The electrochemical measurements are performed using CR2032 coin-type cells assembled in a dry argon-filled glove box. The test cell consists of a working

anode electrode with Si nanotube thin films and a counter electrode made using lithium metal. The electrodes are separated by two pieces of glass fiber filter (ADVANTEC GB-100R, Toyo Rishi CO., Japan). The electrolyte solution used is 1 M LiPF₆-ethylene carbonate (EC): dimethyl carbonate (DMC) (1: 2 by volume). No binders are used. The mass loading of active working electrode was 1.0~1.5 mg cm⁻².

3.5 Structural and electrochemical characterization

3.5.1 Structural characterization of silicon nanowires and nanotubes

Scanning electron microscopy (SEM) was used to obtain morphological information of the synthesized samples. Using this technique we were able to measure the lengths, nanowire diameter and droplet diameter of the synthesized nanowires. This information was essential for the experimental approximation of the activation energy of the silicon nanowire growth. The transmission electron microscopy (TEM) was employed to obtain information about the crystal planes of the samples and the diffraction patterns that allowed us to determine the growth direction of our synthesized silicon nanowires. X-ray diffraction (XRD) experimental technique was used in this work to obtain crystallographic information of our materials in order to determine the composition of the sample. Specifically this technique was employed to detect the presence of GaN in a Ga sample exposed to nitrogen plasma. Raman spectroscopy provided us information about molecular vibrations for sample identification. In our case we were able to identify different silicon hydrogenated phases in silicon nanotubes thin films samples.

3.5.2 Electrochemical characterization

The charge–discharge measurements are carried out using a battery tester (16 channel Arbin Instruments, USA). The charge –discharge tests were made using different current densities: 100, 500, 1000, 2000, and 4200 mA g⁻¹.

We also performed a cyclic voltammetry study of the silicon nanotube thin films. Following we will briefly describe this technique and how we performed for this particular testing.

Cyclic voltammetry (CV)

Cyclic voltammetric characterization studies were also performed for studying the lithiation and de-lithiation behavior of silicon nanotube thin films. Cyclic voltammetry (CV) is one of the most commonly used electroanalytical techniques for silicon nanowires as well as silicon nanotubes anodes. It is an excellent tool, but is not usually a good technique for quantitative analysis. Its main advantage in electro analysis is its ability to characterize an electrochemical system.

In a CV experiment, the potentiostat applies a potential ramp to the working electrode to gradually change the potential and then reverses the scan, returning to the initial potential.

The cyclic voltammetry study was carried out using three cell electrodes with 1M LiPF₆-EC:DMC (1:2) electrolyte, where silicon nanotube electrode was used as a working electrode and Li metal was used as both counter and reference electrode. The cyclic voltammetry measurement was carried out at the voltage range of 2.2 – 0.002 V with scan speed of 1 mV s⁻¹ using eDAQ e-corder potentiostat.

CHAPTER 4

PLASMA-GALLIUM SYNERGISTIC EFFECT FOR THE GROWTH OF SILICON NANOWIRES AT LOW TEMPERATURE

In this Chapter, fundamental studies to understand the synergistic effect on the use of Gallium under plasma excitation for the growth of silicon nanowires at low temperatures are presented. Studies were performed to determine the conditions that promote tip-led growth of silicon nanowires when using low-melting metals specifically Gallium. Growth kinetics studies were performed to estimate activation barrier involved and a mechanism is proposed to explain the synergic effect between plasma and molten Ga for selective dissolution of silicon from the vapor phase. Finally, a synthesis approach is presented for controlling diameter for silicon nanowires.

4.1 Tip led growth of silicon nanowires using Ga

The silicon nanowires synthesized in this section were prepared as follows: A thin layer of molten metallic Gallium was placed on different clean substrates such as silicon and quartz. The substrates then were exposed to silane plasma ($2\% \text{SiH}_4/\text{H}_2$) at 0.1 torr pressure, 70 W RF plasma power and at different temperatures ranging from 100°C to 500°C . Typical duration of the experiments was 30 minutes.

Figure 4.1.1 shows typical SEM images for the resulting silicon nanowire arrays grown using Ga droplets on silicon and non-silicon substrates at 335 °C. In almost all cases, the nanowires grew vertical away from the substrate with Ga at tips indicating tip-led growth. The resulting nanowires exhibited different morphologies depending up on Ga droplet size. The wide distribution of observed nanowire diameters is due to the use of Ga films for creating Ga clusters. As discussed later, the use of gallium oxide nanoparticles for producing Ga clusters allowed for more uniform size distribution of silicon nanowire diameters. In the case of larger Ga droplets with diameters larger than 200 nm, the resulting Silicon nanowires exhibited a stair-like morphology. At smaller diameters with sizes below 200 nm, the nanowires grew straighter with less kinking. The Ga droplet size is larger than the resulting nanowire diameter for larger sizes (> 100 nm) whereas for smaller sizes, the droplet diameter size is similar to that of the resulting nanowire diameter. As expected, the molten Ga exhibited non-wetting behavior with all substrates when exposed to atomic hydrogen using plasma activation at elevated temperatures beyond 100 °C. The extent of non-wetting is expected to be higher with larger diameter due to large cohesive strength of Ga depending upon temperature. Thus, at very high temperature, Ga would exhibit complete non-wetting behavior irrespective of the size¹¹⁶. The experimental observations of the resulting diameters of the nanowires being smaller than those of the Ga droplets can be explained by the differences in the interfacial contact area between Ga droplet and the substrate depending upon size. At smaller sizes (less than 100 nm), the wire diameter is almost the same as that of the droplet indicating higher interfacial contact area between Ga droplets and substrate. Figure 4.1.1 (d) shows clearly the presence of a Ga neck on the Si nanowires, a common feature in our nanowires.

Additional images can be seen in Figure 4.1.2 and Figure 4.1.3. This observation is particularly intriguing given the fact that extremely small solubility of Ga in solid silicon. In addition, the presence of neck always coincided with silicon film deposition around the Ga droplet. Thus, the neck formation is hypothesized to occur as below. During reactor shut down, silicon film forms on molten Ga forming a shell. Due to volume expansion at low temperatures, the molten Ga is hypothesized to expand and diffuse into the solid Si forming a neck region. Similar diffusion, due to capillary pressure forcing the melted metal into the nanowire neck at elevated temperatures, has been observed for gold inside a germanium nanowire covered with a carbon shell¹¹⁷.

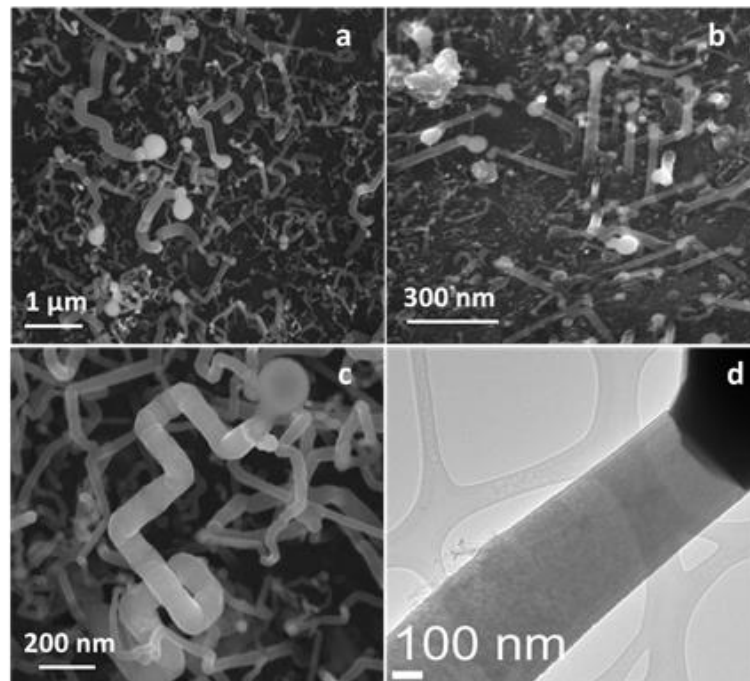


Figure 4.1.1 a) SEM image of stair-like Si nanowires morphology with diameters > 200 nm grown at 335 °C; b) SEM image of straight Si nanowires with diameters < 200 nm grown at 370 °C; c) High magnification SEM image of a single staircase Si nanowire

morphology grown at 335 °C; d) TEM image of a silicon nanowire showing the gallium neck.

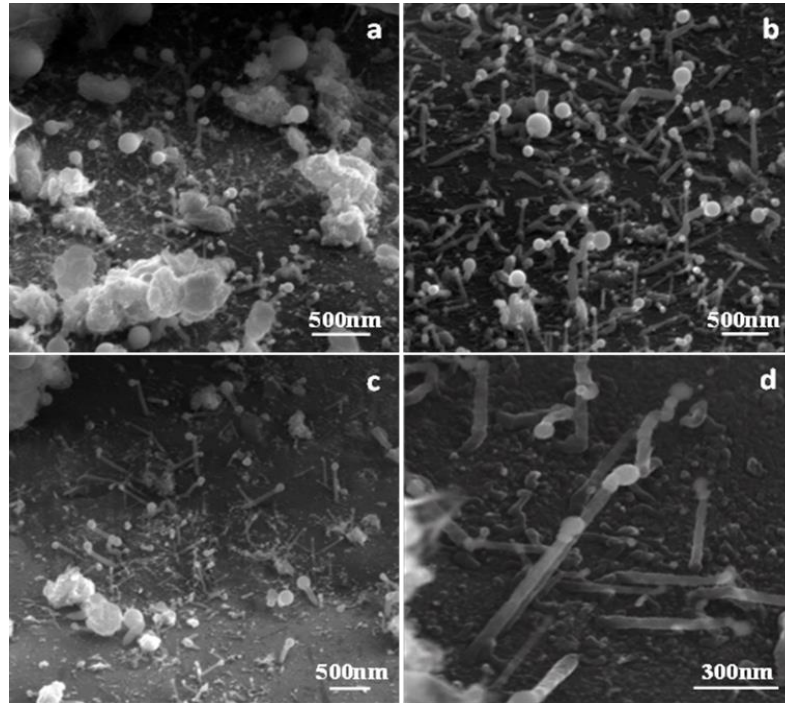


Figure 4.1.2 a), b), c) and d) SEM images of tip-led silicon nanowires grown at 335 °C furnace temperature, used for length measurements.

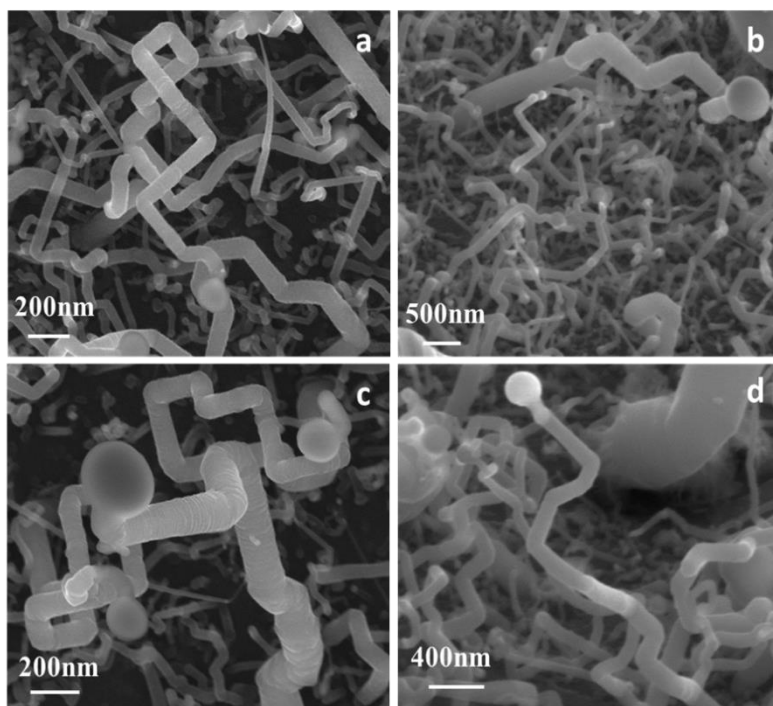


Figure 4.1.3 a), b), c) and d) SEM images of silicon nanowires grown at 335 °C for 30 min with plasma power of 70 W, 0.1 torr pressure, and 10 sccm of 2% SiH₄/H₂.

Several sets of experiments were performed to understand the low temperature limit for silicon nanowire growth using vapor phase precursors over molten Ga. The experiments with 2% SiH₄ in H₂ suggest the low-temperature limit for tip-led growth to be 250 °C. Experiments conducted between 210 °C and 250 °C resulted in bulk nucleation and growth of nanowires with diameters on the order of 10 nm or lower in size from micron-sized Ga droplets. Below 210 °C, there seems to be a ubiquitous Si film deposition everywhere including Ga droplet surfaces. At low temperatures, the use of only silane in hydrogen triggers ubiquitous silicon deposition lowering the selectivity for tip-led growth at low temperatures. As discussed later, the use of Si-H-Cl system allowed

enhancing the selectivity for silicon dissolution in to Ga droplets and lowering the temperature limit for nanowire growth.

4.2 Bulk nucleation versus tip led growth of silicon nanowires at low temperatures

At temperatures lower than 250 °C, we observed the precipitation of silicon nanowires in bulk fashion. Bulk nucleation of silicon nanowires at temperatures between 210 °C-250 °C can be explained as follows: because of an evenly deposition of a solid silicon layer formed on the surface of molten Ga droplets in the initial stages, the deposited silicon dissolves in to Ga droplets similar to that observed for Ga droplets on silicon substrates in which silicon dissolves through the solid-liquid interface. This in turn results in a rapid dissolution through solid-liquid interface and enables the silicon concentration in Ga droplet to reach the spinoidal decomposition limit. At spinoidal decomposition limit, the dissolved silicon and Ga undergo spinoidal decomposition leading to bulk nucleation⁹ resulting in high density of sub-5 nm sized Si nanowires from low-melting metals. Earlier observations reported for Sn and In⁵⁰ with vapor phase supply of precursor at low temperatures ~ 240° C are consistent.

The tip-led growth observed in experiments at temperatures above 250 °C can be understood as the result of slow dissolution of silicon directly from the vapor phase precursors. Such slow dissolution in the initial stages allows the concentration of Si to stay closer to equilibrium solubility of Si-Ga system and the precipitation occurs in the interface of the solid-liquid (substrate-Ga droplet) leading to the growth of one nanowire with one tip at its end. This is again consistent with the observations in which the

resulting nanowire diameters being similar to contact area between droplet and the substrate.

4.3 Silicon nanowire growth experiments at low temperatures using chloro-silane gas phase

In order to increase the selectivity of silicon nanowire growth at lower temperatures, experiments were performed using KCl powder within the chamber to provide for chlorosilanes in the gas phase. The hydrogen radicals can react with potassium chloride and create chlorine and chloro-silanes in the gas phase. Similarly, experiments were also conducted by introducing hydrochloric acid soaked silicon powder. The results were similar in both cases indicating that there is no role for potassium or potassium chloride in the process except for producing chloro-silanes in the gas phase.

As shown in Figure 4.3.1, the SEM images indicate that the use of KCl lead to the improvement on the selectivity of silicon dissolution into Ga droplets, as no silicon deposition was observed on substrates at temperatures as low as 130 °C (Figure 4.3.2). In the experiments involving the use of chlorine in the gas phase, bulk nucleation and growth from large droplets at all temperatures tested were avoided. And it was observed the resulted tip-led growth of nanowires at temperatures as low as 180 °C. See SEM images in Figures 3a and 3b. In addition, there was no Si film formation on the substrates. Selective nanowire growth using Ga clusters at temperatures as low as 180 °C is encouraging and strongly suggest that suppression of the ubiquitous Si film deposition plays a key role in facilitating the tip-led growth of nanowires even at low temperatures.

However, it should be noted that the temperature of the Ga cluster could be higher than the measured substrate temperature due to heating caused by atomic hydrogen recombination. Bulk nucleation observations suggest that solid silicon deposited on Ga droplets in the initial stages dissolves in to Ga droplets through solid-liquid interface, and results in high supersaturation leading to a spontaneous nucleation in the initial stages with high nanowire density from Ga droplets.

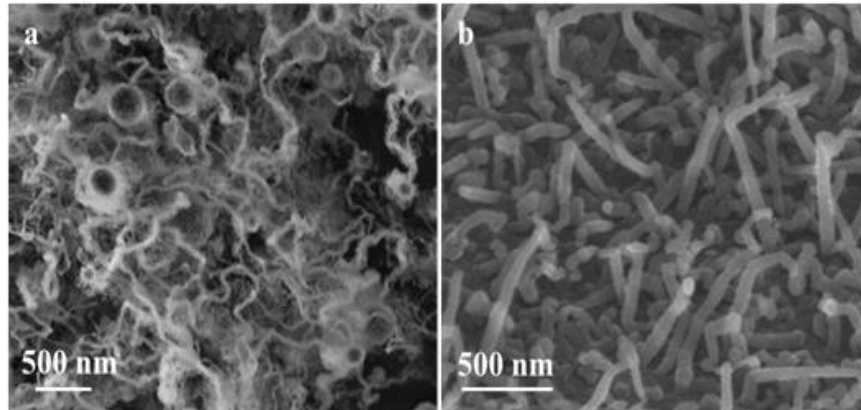


Figure 4.3.1 Low temperature experiments. a) SEM images of Si nanowires grown at 180 °C and b) 220 °C using KCl in the reactor chamber and gallium oxide nanoparticles previously reduced with H₂/Ar mixture.

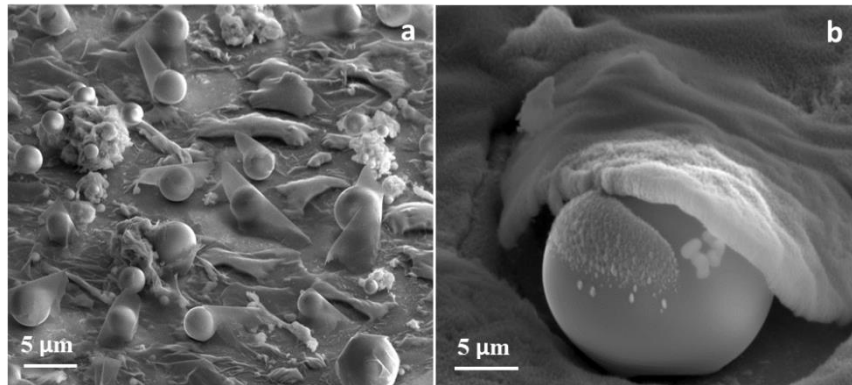


Figure 4.3.2 a) SEM images of gallium droplets covered with a silicon layer observed in sample synthesized at a) 180 °C, 30min and b) 80 °C, 4h. Both samples were obtained in absence of KCl in the reactor chamber.

4.4 Structural characteristics of the synthesized silicon nanowires

As mentioned earlier, in the case of large diameter (> 200 nm), the wires shown in Figure 2 seem to kink vertically during their growth. This is, most likely, due to the nature of the interface between the droplet and the silicon wire, which is not necessarily flat and can involve faceting^{6, 30}. In such a case, droplets larger than the wire diameter can shift on to different facets leading to kinking of wire during growth. TEM characterization of kinked wire suggested that the growth direction does not change with kinking. Such kinking behavior is not seen with smaller diameter nanowires. Figure 4.4.1 shows the TEM images for the sample obtained at 335 °C. Figures 4a and 4b show the high resolution images and the corresponding [110] zone axis diffraction patterns for a typical thicker and thinner nanowire for this sample. Using diffraction patterns, the growth directions for both thicker and thinner wires were determined to be same in the $\langle 111 \rangle$ direction. Some of the thicker wires showed the presence of planar defects such as stacking faults. Interestingly, thinner nanowires exhibit single crystallinity with no apparent stacking faults. In almost all experiments, the preferential growth direction for wires grown with Ga at their tips under our experimental conditions seems to be $\langle 111 \rangle$.

Also, the resulting Si NWs exhibited uniform size over several microns length scale while when using similar metals such as In and Sn, the Si NWs tend to be tapered due to high vapor pressure of In and Sn at growth temperatures.

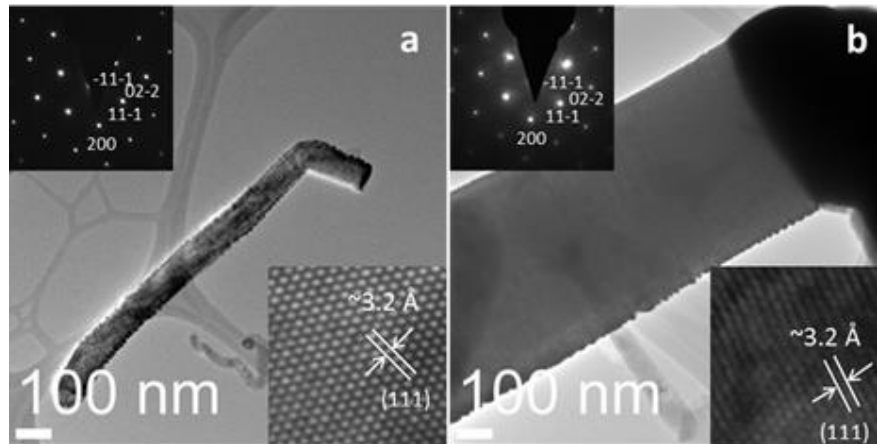


Figure 4.4.1 TEM images for sample obtained at 335 °C. a) Thin Si nanowire and b) thick Si nanowire high resolution images and the corresponding [110] zone axis diffraction patterns. The Si nanowire growth directions were determined to be (111).

Figure 4.4.2 shows the TEM analysis for different types of defects found in the synthesized nanowires. For example, some of the thin silicon nanowires grown at 370 °C have twinning planes along their length in the (111) direction as seen in Figures 4.4.2 (a) and 4.4.2 (b). Such morphology has been shown to result with changing precursor pressure and growth temperature for Au cluster¹¹⁸. In the present case with Ga droplets, due to low dissolution kinetics, it is possible that the silicon concentration in Ga droplets is undergoing some sort of fluctuation resulting in such periodic occurrence of twinned regions. In a sample grown at 280 °C, both thin and thick nanowires exhibited saw tooth faceting (Figure 4.4.2 (c)). This kind of defect has been observed previously for the Au-Si system and it has been explained as the result of the interplay of geometry and surface energies of the nanowire and the liquid droplet⁶. In some cases we observed also bi-crystal nanowires (Figure 4.4.2 (d)). Raman analysis showed also the characteristic Silicon peak for samples grown on quartz (figure 4.4.3). In some cases we observed also

bi-crystal nanowires (Figure 4.4.2 (d)). Raman analysis showed also the characteristic Silicon peak for samples grown on quartz (Figure 4.4.3). The shifting of the Raman peak values (520cm^{-1} , 518 cm^{-1} and 516 cm^{-1}) observed for different samples has been already reported and attributed to the local nanowire heating effect, being a common observation in samples having a wide range of nanowire diameter⁹

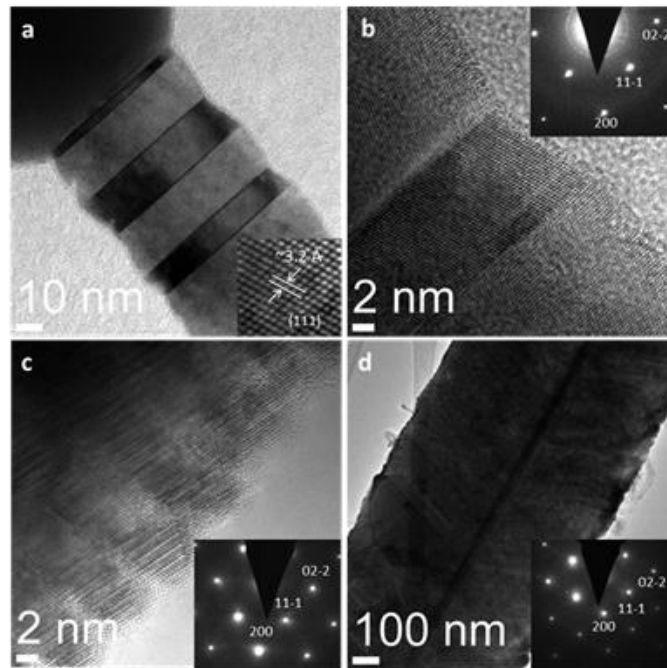


Figure 4.4.2 a) and b) TEM images of Silicon nanowires grown on quartz substrate at 370 °C showing twinning planes in the (111) direction all along their length c) TEM image of a straight thin silicon nanowire grown at 370 °C showing sawtooth faceting d) TEM image of a bi-crystal Si nanowire grown at 335 °C, both crystal planes are in the (111) direction.

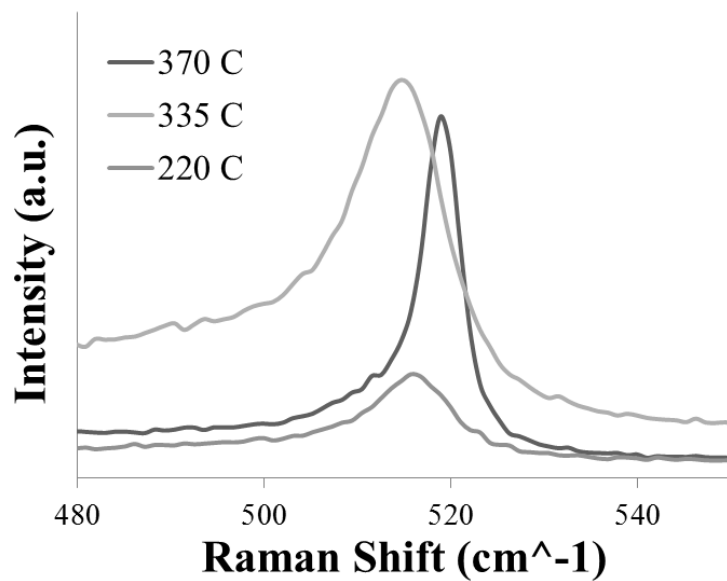


Figure 4.4.3 Raman peaks from selected Si nanowire samples growth on quartz substrates at different temperatures.

Another interesting morphology was observed for some of the Si nanowires grown from large droplets with bulk nucleation at low temperatures (as low as 210 °C). They showed “rope like” morphology but exhibited crystallinity as shown in Figures 4.4.4 and 4.4.5. The polycrystalline nature of these bulk nucleated silicon nanowires is attributed to the low temperature synthesis.

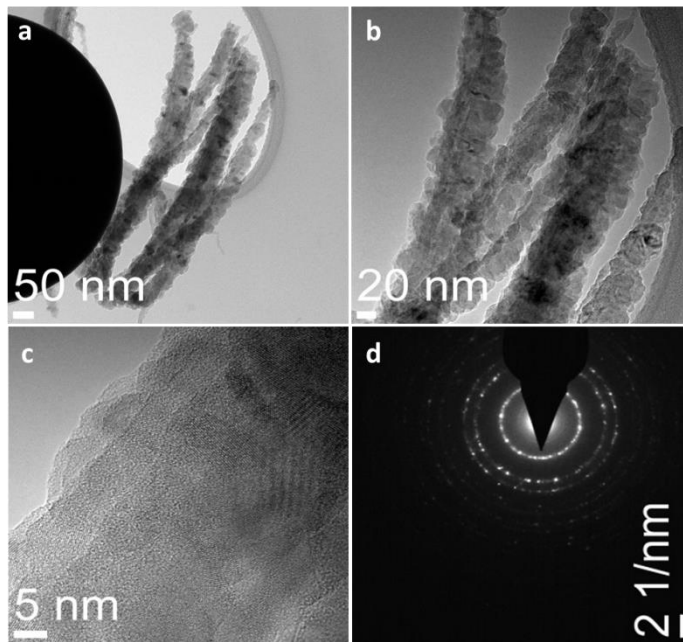


Figure 4.4.4 a) and b) TEM images of bulk nucleated silicon nanowires grown at 220 °C. c) High resolution TEM image. d) Diffraction pattern showing the polycrystallinity of the sample.

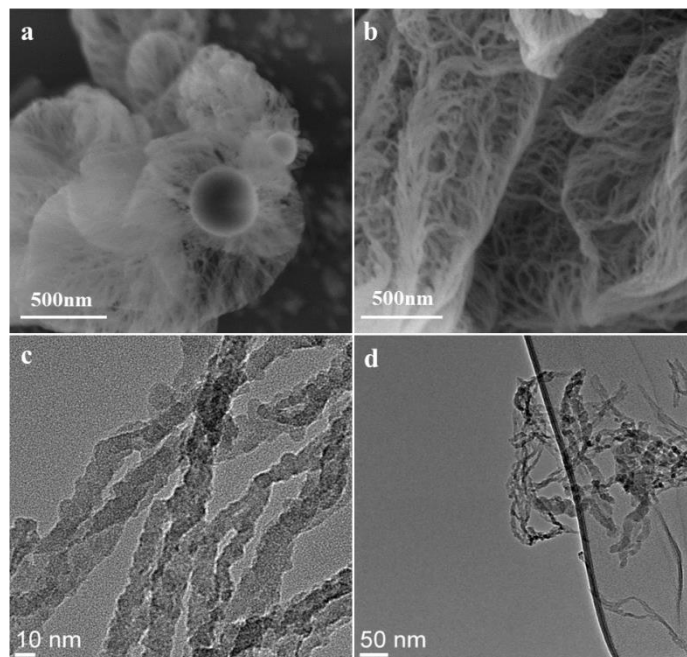


Figure 4.4.5 a) and b) SEM images of bulk nucleated silicon nanowires grown at 210 °C c) and d) TEM images of bulk nucleated silicon nanowires at the same temperature.

4.5 Growth kinetics of silicon nanowires using Ga clusters at their tips

Typically, in vapor-liquid-solid method, the Gibbs-Thompson effect ensures that the growth rate is higher for smaller diameter nanowires¹¹⁹. Similarly, the surface diffusion effects lead to faster growth rates for the smaller diameter nanowires. Therefore, the observation of higher growth rate for nanowires with larger diameters deserves careful further analysis. In all our experiments with different Ga droplet sizes, the size of Ga droplet showed a continued linear increase in size until it reached a ratio of 2:1, or higher i.e., that the Ga droplet diameter was two times or more than the size of the nanowire diameter (Figure 4.5.1). The statistical analysis suggested that the ratio of Ga droplet size to resulting nanowire diameter was approximately 1:1 until about 200 nm where it reached a constant 2:1 ratio for all sizes larger than 200 nm. It was clearly observed that the small Ga droplets had a higher tendency to wet the substrate compared to the big Ga droplets⁶⁰. Thus, the non-wetting behavior at the initial stages of the growth was responsible for the 2:1 ratio of the droplet and the resulting Si nanowire in case of bigger droplets. Interestingly, for a big Ga droplet that had a larger exposed surface area for dissolution; the Si nanowires precipitating grew faster, however this observation is being analyzed further. In addition, it is well known that small molten gallium droplets tend to agglomerate due to its high surface tension. Thus, such behavior results in the formation of micron size gallium droplets. Consequently, there are gallium droplets of different sizes.

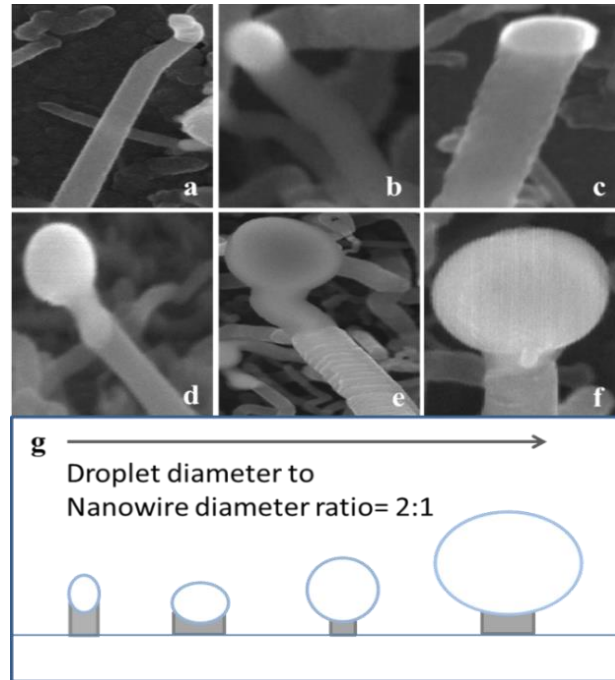


Figure 4.5.1. Droplet diameter to nanowire diameter ratio (a)-(f) SEM images (g) schematic. The size of the gallium droplet showed a continued linear increase with respect to the Si nanowire diameter. The Ga droplet size to resulting nanowire diameter ratio varies from a 1:1 ratio for nanowires < 200nm to a 2:1 ratio for bigger nanowires.

The lengths and diameters of nanowires and droplet diameters of several samples were determined and analyzed to understand the growth kinetics. The results are summarized in Figure 4.5.2. More specifically, Figure 4.5.2a shows the droplet diameter to nanowire diameter. As we can observe from this plot for small nanowire diameters the droplet diameter to nanowire diameter ratio is 1:1 and keeps increasing until 2:1 or more for micron or higher size nanowires. In terms of growth kinetics, the average growth rate is determined by using the lengths of resulting nanowires. It is important to remark that big nanowires tend to be kinked making it difficult to measure the lengths. So, the growth rate is difficult to measure for nanowires with diameters greater than micron. Figure 4.5.2b shows the droplet diameter vs growth rate and it is possible to observe that for big

droplets i.e., $\approx 1\mu\text{m}$ when the droplet diameter to nanowire diameter is 2:1 the growth rate becomes constant as marked by the horizontal blue line. As explained before, the constant growth rate for micron sized or bigger nanowires is an artifact of experimental measurement. Figure 4.5.2c shows the ratio droplet diameter/ nanowire diameter vs growth rate in this plot it is possible to observe that the growth rate becomes constant at a ratio of 1.8, denoted again by the blue horizontal line. Finally, figure 4.5.2d shows the growth kinetics of the nanowires as a function of synthesis temperatures in the 280 °C to 470 °C range for nanowires less than 100nm in diameter where the growth rate is linearly proportional to the nanowire diameter for the presented range of nanowire synthesis temperatures.

The growth kinetics data suggests that the growth rate increases as the nanowire diameter. Also, the kinetics increase with temperature indicating some temperature activated process. The data further suggests that larger diameter nanowire grows faster than that of smaller sized nanowire. Such observation needs to be explained further. In order to understand the data, various models available for vapor-liquid-solid growth of nanowires are detailed in the next section.

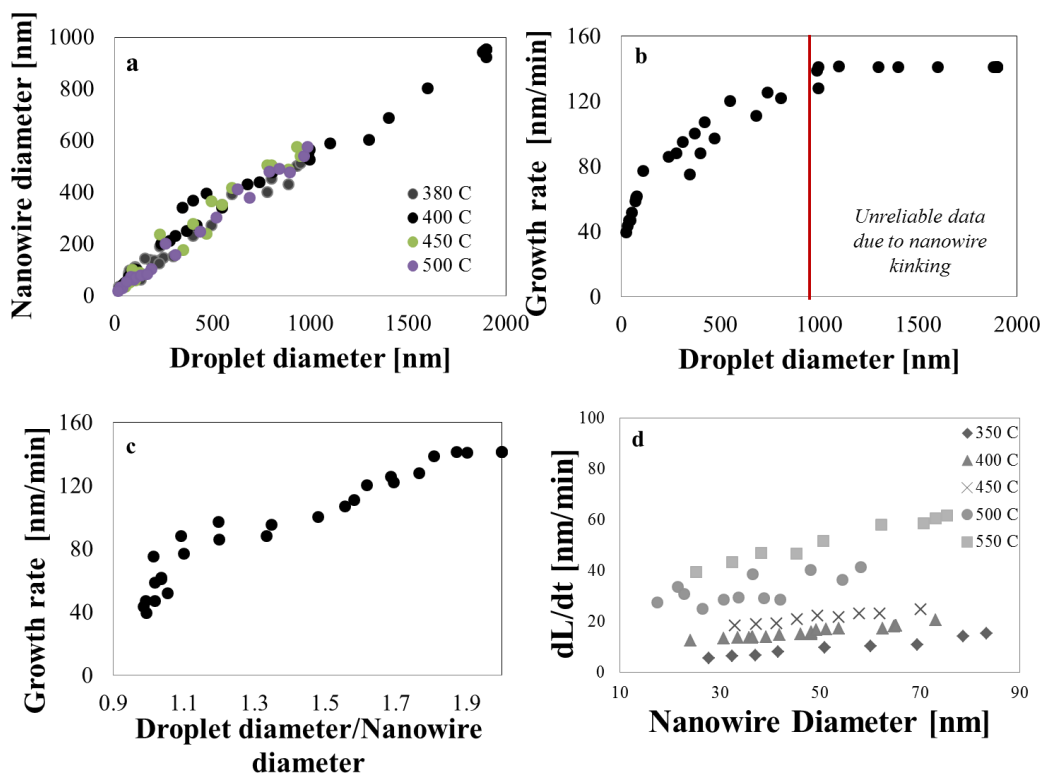


Figure 4.5.2 Growth kinetic studies for silicon nanowires: a) Droplet diameter versus resulting nanowire diameter at different temperatures. b) Growth rate as a function of droplet diameters. c) Growth rate as a function of droplet diameter/nanowire diameter ratio at 400 °C. d) Growth rate as a function of nanowire diameter at various temperatures within 280°C-470 °C range.

4.6 Gibbs–Thomson effect

The Gibbs-Thomson effect is of great importance since it has consequences on the growth rate of nanowires, thus the necessity to understand it. The chemical potential, $\mu = \mu_{\infty} + 2\Omega\sigma/R$ can be written as a function of radius (R) of the droplet. Similar relationship exists for spherical droplet at the tip of growing nanowire. The above Gibbs-

Thompson effect suggests that the equilibrium vapor pressure near droplet at the tip of smaller diameter is more than that at larger diameter nanowire or at planar surface.

The Gibbs-Thompson effect essentially represents the idea that thermodynamic parameters of nanoparticles such as pressure and chemical potential are essentially size-dependent. One of the most important manifestations of the size-dependent effects is a tremendous increase of the equilibrium pressure inside a nanoparticle and the corresponding elevation of its chemical potential. Both effects are driven by the surface curvature. Whenever the system consists of two or more phases, for example, liquid droplets surrounded by vapor, all thermodynamic potentials are modified by the surface energy term.

In summary, the Gibbs Thomson effect is often used to explain the nanowire growth rate based on the fact that a decreasing particle size leads to an increase of the pressure inside the metal particle due to an increase of the surface curvature. Therefore, smaller droplets will desorb more atoms than larger ones, which will suppress the nanowire growth from droplets smaller than a certain critical radius and at the same time it explains the fact that a higher vapor pressure could result in higher flux to the droplet leading to faster growth kinetics for smaller diameter nanowires.

4.7 Kinetic models for the growth of silicon nanowires

In this section, we will revise the different kinetic models that are available in the literature for the growth of silicon nanowires. Here in we present 4 main cases, each of them having a different limiting step³⁰.

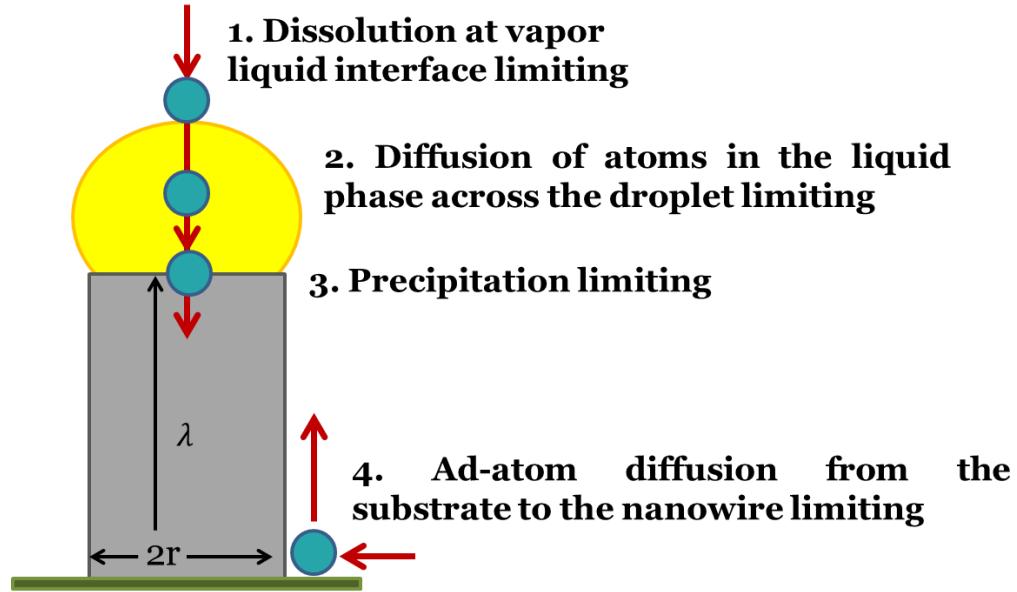


Figure 4.7.1 Schematic illustrating the possible limiting processes in the VLS growth of silicon nanowires.

Case 1: Dissolution at the vapor-liquid interface as rate limiting step: in the case of growth controlled by processes at the vapor-liquid interface, the supersaturation in the gas phase is much larger than that in the liquid droplet. A general balance that represent the events happening in the metal droplet:

$$\frac{2}{3}\pi R^3 \frac{dC}{dt} = \pi R^2 x_{vl} J - 2\pi R^2 \frac{r_1 C}{\tau_1} - \pi R^2 \frac{V_{NW}}{\Omega_m}$$

# molecules in the volume of the metal droplet	# molecules absorbed	# desorption events	# molecules lost for crystallization
--	-------------------------	------------------------	--

Where in this equation:

$J = \text{adatom flux,}$

$V_{NW} = \text{nanowire growth rate,}$

$x_{vl} =$

coefficient of condensation of molecules from vapor on to the liquid droplet,

$\tau_i = \text{average lifetime of molecules on the liquid surface}$

$\Omega_m = \text{specific volume of the molecule.}$

The result is that at steady state, the growth kinetics of nanowire is diameter-independent determined only by adsorption and desorption processes. As it is clear from the equation above the two R^2 of the terms of absorption and desorption are cancelled and the dependence on the radius/diameters disappears.

In order to understand better this equation and accounting for the difference in supersaturation on the vapor and liquid phases, Meyyapan et al³⁰ presented it in a simplified way in terms of the nanowire growth rate as:

$$V_{NW} = V_0(\Phi - \mu)$$

Where

Φ is the measure of supersaturation in the gas phase determined by the balance of adsorption and desorption processes

μ is the super saturation in the liquid phase

V_{NW} nanowire growth rate

V_0 is a coefficient dependent on the equilibrium concentration, molar volumes of the growth species in the solid and liquid phases and the average life time of the molecules on the droplet surface controlled by desorption processes

In this case of nanowire growth controlled by processes at the vapor-liquid interface, the supersaturation in the gas phase is much larger than that in the liquid droplet. Considering this, the solution of the equation presented becomes trivial and the result is a diameter independent growth rate determined only by adsorption and desorption processes.

Case 2: Diffusion of atoms in the liquid phase across the droplet as the rate limiting step.

This case can be modeled by the Fick's equation for mass diffusion:

$$J_A = -\rho D_{AB} (dw_A/dx_i)$$

Where: $J_b = \text{Molecular Flux}$, $D_b = \text{diffusivity}$, $w_A = \text{concentration}$ and $x_i = \text{length}$

This model means slower growth for thicker wires, which have a thicker catalyst beads. As it can be observed from the expression above a bigger x_i value will lead to a reduction in the molecular flux that is limiting in this case the nanowire growth rate. Then a bigger bead will lead to shorter nanowires. However, this only applies under the assumption that the concentration at the tip is some value irrespective of the diameter and the concentration at the growth front is small leading to a lower gradient with increased diameter.

Case 3: Precipitation kinetics as the limiting step

In this case the precipitation kinetics is directly proportional to the concentration (supersaturation) that exists in the droplet.

According to the Gibbs/Thomson effect, the decrease of supersaturation can be expressed as: $\Delta\mu = \Delta\mu_0 - 4\Omega\alpha$.

Where $\Delta\mu$ is the effective difference between the chemical potential in our case of the Si in the vapor phase and in the nanowire, $\Delta\mu_0$ is the same difference when the nanowire diameter becomes infinite, α is the specific free energy of the nanowire surface and Ω is the atomic volume of Si. The growth rate typically represented by V is given by $V \sim \left(\frac{\Delta\mu}{kT}\right)^n$.

From these two equations it is possible to obtain:

$$\sqrt[n]{V} = \frac{\Delta\mu_0}{kT} \sqrt[n]{b} - \frac{4\Omega\alpha}{kT} \sqrt[n]{b} \frac{1}{d}$$

Where:

b is the kinetic coefficient independent of supersaturation.

$V^{1/n} = \text{growth rate}$,

$d = \text{nanowire diameter}$,

$\Omega = \text{molar volume of species within the cluster}$,

$\Delta\mu_0 = \text{change in chemical potentials of species in the gas phase to that in the solid phase}$,

$\kappa = \text{Boltzmann constant}$, $\alpha = \text{liquid-vapor interface tensions}$.

This equation presents a general relationship between the nanowire diameter and the growth rate.

This latest equation is the well-known Givargizov model¹²⁰ and relates the growth rate (V) to the supersaturation (driving force for crystallization).

It can be observed that as diameter increases, the growth rate increases predicting faster growth rate for thicker whiskers than thinner ones. However, it is important to mention that the model used for develop this equation is flawed. This is because this equation predicts a diameter limit below in which one cannot observe VLS growth. It has been shown in many materials systems, nanowires could be grown using VLS mode with diameters in the sub 5nm sized nanowires up to 2nm for Si¹²¹. Thus the model and the assumptions of supersaturation are not appropriate for VLS growth.

Case 4: Adatom diffusion from the substrate to the nanowire as the limited step Seifert et al¹²² proposed a simple expression for the nanowire growth including R_{top} , the material which directly hits the particle at the top of the whisker and (ii) R_{side} , the material which diffuses towards the particle after it has arrived at the (ideally) non-growing side-facets:

$$R_L = mR_{top} + nR_{side}$$

Where:

$$m = \frac{2\pi r^2}{\pi r^2}, n = \frac{2\pi r \lambda}{\pi r^2}, R_{top} \approx R_{side} \approx R$$

R stands for the arrival rate of reactant species per surface site.

$$\text{Then: } R_L = 2 \left(R + \frac{\lambda}{r} \right)$$

The linear growth rate should increase with the reactant pressure p and, due to the term λ/r , thinner nanowires should grow faster than thicker ones.

As it can be observed, any of the models described in this section can correlate with our experimental observations of the droplet diameter to the nanowire diameter ratio

1:1 for thinner nanowires and the droplet diameter to the nanowire diameter ratio of 2:1 or more for thicker nanowires. Furthermore, they failed explaining the observation that thicker nanowires grow faster due to higher surface available for the dehydrogenation reaction to occur comparing to thinner nanowires that grow slower due to a smaller surface area available for the dehydrogenation reaction to occur. Despite the Givargizov model predict that thicker nanowires grow fast this model it has the inaccuracy of taking the chemical potentials in the gas phase equal to those in the solid phase which makes this method unreliable. These observations led us to propose a model that can explain our experimental observations and it is described in the following section.

Our proposed model: Dissolution kinetics limiting as the rate limiting step

First of all, all of the above models are developed for constant ratio between droplet diameter and nanowire diameter. In our case, the droplet diameter to the nanowire diameter ratio is 1:1 for thinner nanowires and the ratio increases to 2:1 or more for thicker nanowires. Secondly, even for constant diameter ration, majority of models predict faster growth kinetics for smaller diameter nanowires. As discussed before, the Givargizov model that predicts faster growth for thicker nanowires uses inaccurate assumption about supersaturation within droplets being diameter dependent and makes inaccurate predictions of diameter limits for growth. The experimental observations here on silicon nanowire growth using Ga droplets will need to be explained further with a new model. The details of our proposed model are described below.

In order to get a mathematical expression that correlates with our experimental observations we made a mole balance on the gallium droplet at steady state condition and with accumulation term equal to zero. The equation for the overall mole balance:

$$\begin{aligned} & \left[\text{molar flow rate of species} \right]_{In} - \left[\text{molar flow rate of species} \right]_{Out} + \left[\text{molar rate of} \right. \\ & \qquad \qquad \qquad \left. \text{generation of species} \right] \\ & = \left[\text{molar rate of} \right. \\ & \qquad \qquad \qquad \left. \text{accumulation of species} \right] \end{aligned}$$

Then:

$$\left[\text{molar flow rate of species} \right]_{In} - \left[\text{molar flow rate of species} \right]_{Out} = 0$$

$$W_{Ar}(4\pi r_d^2) - \bar{\rho}_{Si}(\pi r_{nw}^2) \cdot r_{Si} = 0$$

Where:

W_{Ar} = flux at constant temperature, pressure and SiH₄ partial pressure ($mol/nm^2 \cdot min$)

It is important to mention here that the flux under dissolution kinetics limitation should be:

$$W_{Ar} = kC_{gas}^n$$

Where k is the rate constant, C_{gas} is the concentration of the gas phase and n represents the reaction order that depends of the dissolution mechanism.

r_d = Ga droplet radius, (nm)

$\bar{\rho}_{Si}$ = is the molar density of silicon, (mol/nm^3)

r_{nw} = Si nanowire radius, (nm)

r_{Si} = growth rate (nm/min)

In this simplified mole balance $4\pi r_d^2$ is the surface area of the Gallium droplet and has units of nm^2 , πr_{nw}^2 is the cross section of the silicon nanowire and has units of nm^2 , and finally we made $r_{Si} = dL/dt$ then r_{Si} have units of nm/min.

Then by working with the equation we can get that the growth rate of our silicon nanowires is:

$$r_{Si} \sim \frac{r_{droplet}^2}{r_{nw}^2} \sim \frac{d_{droplet}^2}{d_{nw}^2}$$

Flux of Species

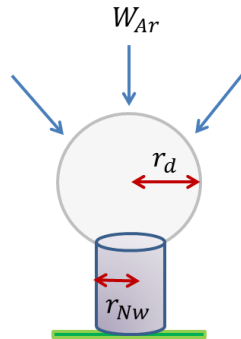


Figure 4.7.2 Mole balance for silicon nanowire growth using Gallium droplet at tip.

From our experimental observations small nanowires have a droplet diameter to nanowire diameter ratio of 1:1 then the growth rate in this case is equal to a constant. This theoretical model based on the mole balance in the Gallium droplet correlates with our experimental observation, as it can be observed from data plotted in Figure 4.5.2.

From our experimental observations, in the whole range of silicon nanowires synthesized (Figure 4.5.2a), it was found that the following mathematical correlation is valid:

$$G_{NW} \sim \frac{A_{droplet} d_{droplet}^2}{A_{nw} d_{nw}^2} \sim f(d_{nw})$$

where, G_{NW} silicon nanowire growth rate, A_{nw} is the cross section area of the Si nanowire; A_d is the surface area of the Ga droplet, d_{nw} , $d_{droplet}$ are diameters of nanowire and Ga droplet, respectively. The agreement with experimental data and observations

suggest that the silicon nanowire growth here is limited by dissolution kinetics at vapor-molten Ga interface.

4.8 Estimation of activation energy for nanowire growth

The activation energy was calculated using the Arrhenius equation and different nanowire diameters, including bigger than 200nm. The average value of the activation energy for all these nanowires was calculated to be 31.9 kJ/mol (Figure 4.6.3).

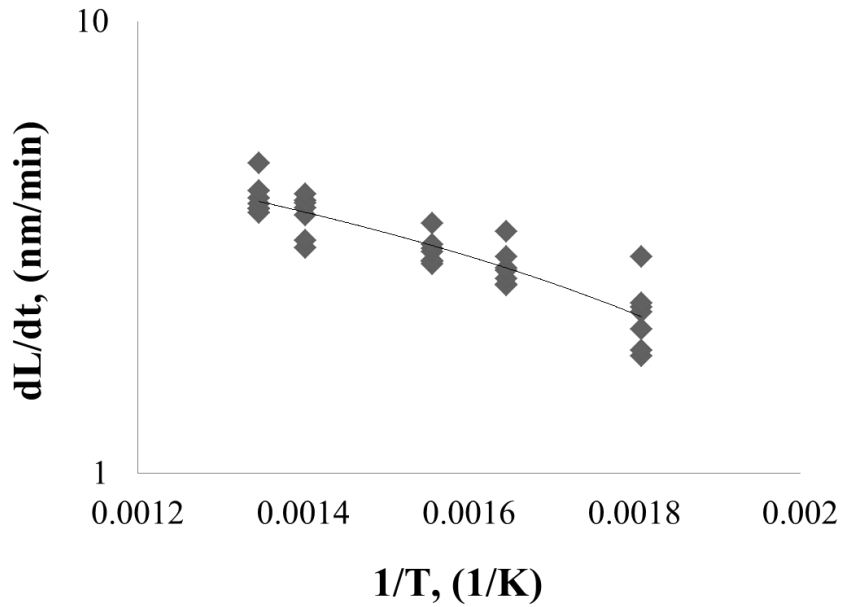


Figure 4.8.1 Arrhenius plot of growth kinetics as a function of temperature.

The activation energy was calculated at constant diameters for nanowires with ≤ 300 nm. As seen in Figure 4.8.1, the activation energy values are estimated to be between 20-40kJ/mol.

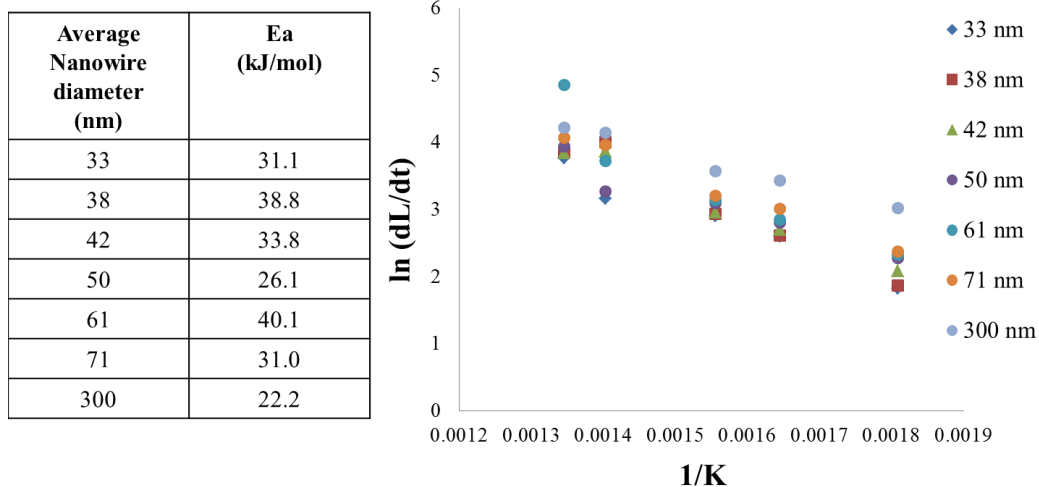


Figure 4.8.2 Arrhenius equation $1/T$ vs $\ln(k)$ plots at constant nanowire diameter using metallic Ga a) 33nm. b) 38nm. c) 42nm. d) 50nm. e) 61nm. f) 71nm. g) 300nm.

In the case of dissolution kinetics limited growth, the volumetric growth rate is proportional to the dissolution rate which itself is proportional to the surface area of Ga droplet. The linear growth rate is then proportional to the ratio of dissolution rate to cross-sectional area of the wire as shown in the equation below. Typically, the ratio of tip surface area and the nanowire cross-sectional area is constant and thus the linear growth rate becomes independent of nanowire diameter under dissolution kinetics limited regime. However, here, for our experiments, the ratio of the droplet and the nanowire diameters increase with nanowire diameter until about 200 nm and then stays constant.

Therefore, it is possible to determine the activation energy for the overall reactions involved in silicon dissolution using growth kinetics data obtained at different temperatures. The apparent activation energy is obtained using the slope of the Arrhenius plot by the best-fit line through the data shown in Figure 4.8.1 The activation barrier height is estimated to be about ~ 31.9 kJ/mol. The data is analyzed for all nanowire

diameters and the activation barriers ranged from 20-40 kJ/mol. In order to explain the silicon dissolution process on the Ga droplet surface, the following two reactions are proposed. In both reactions, silyl radicals from the gas phase adsorb on to Ga surface and undergo dehydrogenation by reacting with surface or bulk hydrogen within Ga (Ga-H). The formation of surface gallium hydride species in gallium catalysts has been reported before⁶⁰. The Ga-H bond energy has been calculated to be ~ 24 kJ/mol, estimated by FTIR spectra^{60, 123}

Table 4.8.1 Proposed surface and bulk reactions happening in the gallium droplet.

Reaction	Approximated Ea (kJ/mol)
$\text{SiH}_3 + \text{Ga-H} \rightarrow \text{Si} + \text{Ga} + 2\text{H}_2$ (4.5.1)	304
$\text{SiH}_2 + \text{Ga-H} \rightarrow \text{Si} + \text{Ga} + 3/2\text{H}_2$ (4.5.2)	138
$\text{SiH} + \text{Ga-H} \rightarrow \text{Si} + \text{Ga} + \text{H}_2$ (4.5.3)	28
<i>Reactions on the surface</i>	
$\text{Ga} + \text{H} \rightarrow \text{Ga-H} + \text{H}_2$ (4.5.4)	24
$\text{Ga-H} + \text{H} \rightarrow \text{Ga} + \text{H}_2$ (4.5.5)	412
<i>Reactions on the surface and bulk</i>	
$\text{Ga-H} + \text{Ga-H} \rightarrow 2\text{Ga} + \text{H}_2$ (4.5.6)	388

As seen from Table 4.8.1, for all possible reactions that could take place, the reaction number (4.5.4) is more likely to be limiting the reaction for the silicon nanowire growth based on the estimated activation energy for the overall growth kinetics. This is supported by the theoretical value of 24 kJ/mol for the activation energy which reasonably agrees to the calculated experimental value of 31.9 kJ/mol.

The activation barrier estimated for Equation 4.5.4 using the bond energies suggests that the experimentally obtained value can be explained by the energy required

to break the Ga-H bonds. Based on the net energy required for bond breakage and formation arguments in Equation 4.5.2, it is possible to conclude that the reaction shown as Equation 4.5.4 is more likely to have activation energy similar to that observed in our experiments.

As the experimental data suggests, the plasma activation of gas phase is necessary to grow silicon nanowires using Ga. This implies that the atomic hydrogen reacts with molten Ga and forms Ga-H species both on the surface and in the bulk. In recent literature, there has been some interest in storing hydrogen using Gallium through formation of Ga-H¹²⁴.

The Gallium hydrides will release hydrogen at moderate temperatures around 200 °C or higher. However, in our experiments involving high concentrations of atomic hydrogen, there will be a dynamic exchange of hydrogen from vapor phase in to molten Gallium and release of dissolved hydrogen to vapor phase through formation of molecular hydrogen. Such dynamic exchange with between molten gallium and atomic hydrogen allows for high concentration of gallium hydrides within molten gallium clusters.

Note that dehydrogenation of silyl radicals on molten gold occurs without the presence of atomic hydrogen. Thus, the selective dissolution of silicon into molten Ga in the presence of atomic hydrogen suggests a synergistic effect which requires having high concentration of atomic hydrogen for catalysis. Based on the above mechanism, it is hypothesized that the molten gallium acts as hydrogen sink that leads to the formation of the Ga-H species which catalyze the dehydrogenation of silyl radicals on molten Ga

surface (Figure 4.8.3). Such enhanced reactivity could be explained for the observed selectivity and the resulting silicon nanowire growth using molten Ga droplets in the presence of plasma gas phase activation.

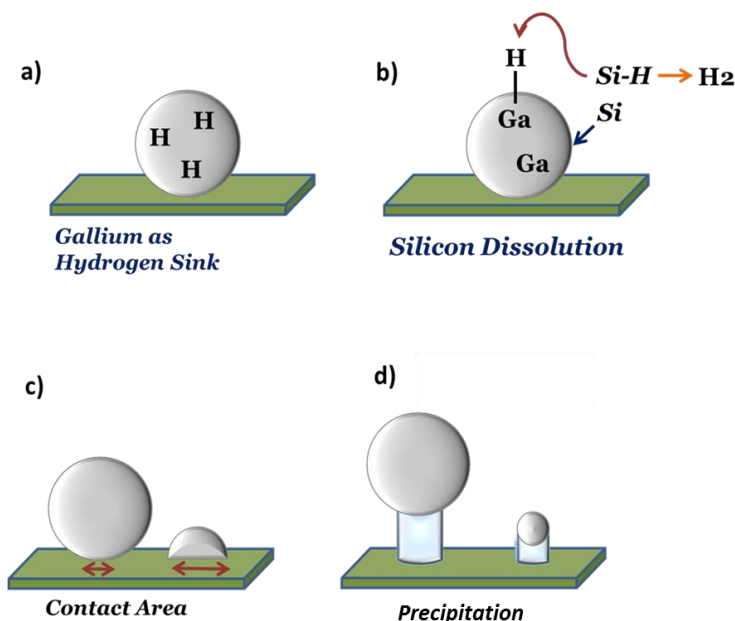


Figure 4.8.3 Schematics illustrating the proposed growth mechanistic steps involved with silicon nanowire growth using Ga droplets: a) The Ga droplet acts as a hydrogen sink. Gallium droplets in the presence of hydrogen tend to capture hydrogen forming Ga-H. b) Dissolution reaction happening on the Ga droplet surface. The Ga-H species formed on the Ga droplet catalyzes the dehydrogenation of the silyl radicals on the surface of the molten Ga. c) Contact area of Ga droplets depending on their size. d) Precipitation of Si nanowires from different droplet size.

It is theoretically possible for growing Si nanowires using Ga droplets at its eutectic temperature of 30 °C or higher. However, the kinetics will be extremely slow. Thus, if the dissolution kinetics could be improved by increasing the atomic hydrogen concentration (plasma conditions), silyl radical concentration, optimized chlorosilane

composition and pressure then it should be possible to reduce the growth temperature to near 100 °C. Growth of crystalline silicon nanowires at sub-200 °C temperatures could open up avenues for their fabrication over thin metal foils for lithium ion battery and plastic substrates for flexible electronics.

4.9 Diameter control of Si nanowires

The use of Gallium films obtained by evaporation and/or spreading leads to Ga droplets with a large size distribution. Therefore, it is important to develop a method to obtain Ga droplets with uniform distribution and also obtain droplets with controlled diameters. Here, the use and reduction of Ga₂O₃ nanoparticles is proposed as an indirect and alternative approach to obtain control on diameter and its size distribution of silicon nanowire arrays.

The synthesis of Silicon nanowires using Gallium (III) oxide 99.9995% (Sigma-Aldrich) <100nm nanometer particle size was carried out as follows: the gallium oxide particles were dispersed on acetone and sonicated for around 30min. The homogeneous solution then was dropped onto different substrates including quartz, silicon and stainless steel. Then the substrates were placed in the reactor and the nanoparticles were reduced at 800 °C for 1 hour using 15sccm of a mixture of 10%H₂/Ar. In order to confirm that the reduction of the Ga₂O₃ was successful we perform EDAX analysis on the reduced droplets. In this way we confirmed that the droplets composition was rich in Ga with non-detectable oxygen content.

Figure 4.9.1(a). shows the distribution of gallium droplets size reduced from Ga₂O₃. The average droplet size was 30nm. The dispersion of the synthesized nanowires is wide, with an average nanowire diameter 68nm. All the synthesized nanowires were

less than 200nm in diameter. The reason for the resulting nanowire diameter being bigger than the starting reduced droplet diameter can be attributed to the agglomeration of the gallium droplets during the initial heating stage for the nanowire growth as in the case when using metallic gallium. This explains the resulting bigger nanowire diameter than the starting reduced Ga₂O₃ nanoparticles diameter.

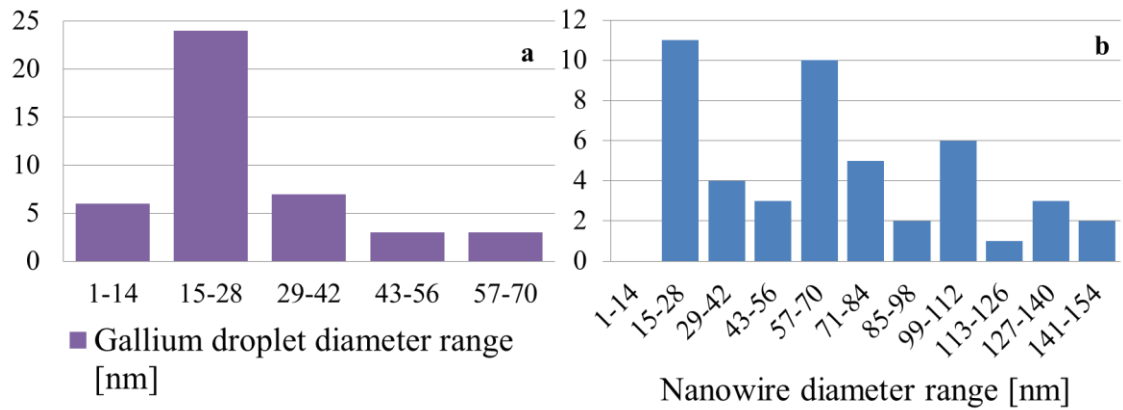


Figure 4.9.1 Histogram showing the size distribution of the gallium droplets formed from the reduction of Ga₂O₃ nanoparticles.

After the reduction, the reactor was cooled down and the desired temperature for the nanowire growth was set. The synthesis of silicon nanowires was performed under typical conditions. Figure 4.9.2 shows the SEM images of the Gallium III oxide nanoparticles reduced and the resulting nanowires obtained. These nanowires were grown at 400 °C. The samples using this method showed high homogeneity of the silicon nanowire diameter size.

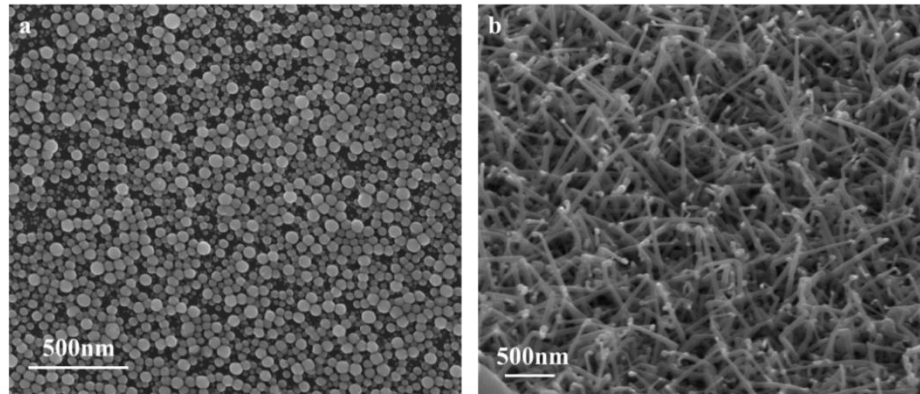


Figure 4.9.2 a) SEM image of gallium droplets reduced from Ga_2O_3 nanoparticles. b) SEM images of synthesized Silicon nanowires using reduced Ga_2O_3 nanoparticles at 400°C .

Silicon nanowire growth experiments were performed at different temperatures using reduced Gallia nanoparticles and the data is used to estimate the activation energy for growth kinetics.

Figure 4.9.3 shows the SEM images for different samples synthesized at different temperatures using reduced Gallia nanoparticles. As it can be observed there is an increased nanowire diameter homogeneity comparing with the samples shown in the previous chapter that were prepared using metallic gallium thin layer on top of the substrates.

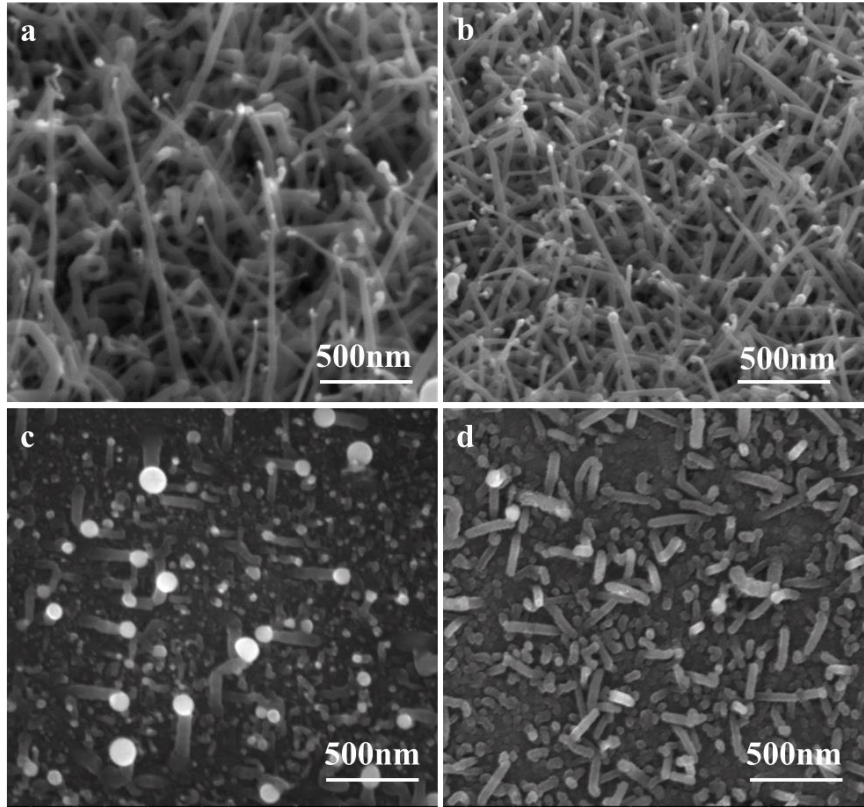


Figure 4.9.3 SEM image of silicon nanowires synthesized using Ga_2O_3 reduced nanoparticles at a) 450 °C, b) 380 °C, c) 300 °C and d) 200 °C.

Another important characteristic of the resulting nanowires is that they show almost no kinks as expected due to their small sized droplets at their tips. Besides the narrow size distribution for diameters and lengths for resulting nanowires, the nanowire diameter to droplet diameter ratio in most of the cases is approximately around 1:1. It is important here to note that these observations agree well with the previous results obtained when using metallic gallium droplets with sizes smaller than 100 nm.

The composition of the synthesized nanowires was performed using EDX analysis on the sample obtained at a growth temperature of 380 °C. Figure 4.6.4 shows that the tip of these nanowires is rich in Gallium but shows the presence of small amounts of oxygen. However, the nanowire appears to be silicon with no oxygen content. This is an important observation as it suggests that it is possible to grow Si nanowires even with partially reduced gallium oxide particles. The use of such particles could avoid coalescence into large droplets during their use.

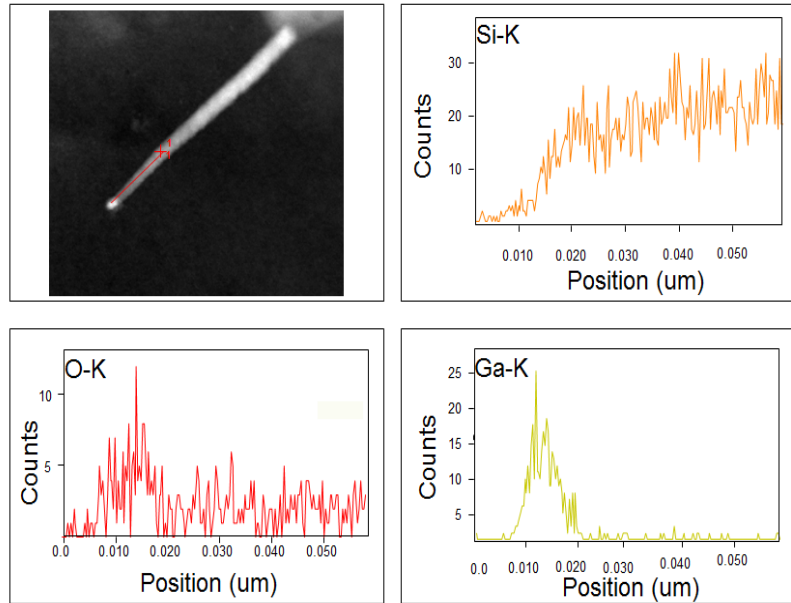


Figure 4.9.4 EDX analysis of a silicon nanowire synthesized at 380° C using Ga₂O₃ reduced nanoparticles.

4.10 Growth kinetics of silicon nanowires using reduced Gallia nanoparticles

The activation energy for the growth of silicon nanowires is extracted from growth kinetics data as a function of temperatures at a constant diameter. The growth rate or dL/dt is determined using the measured lengths and the reaction duration (usually 30min).

Figure 4.10.1 shows the Arrhenius plots for different temperatures at various diameters. The average calculated activation energy value is 35.4 kJ/mol which is still within the range estimated for the growth kinetics when using metallic gallium. However, this value is slightly higher than the previously reported that obtained using pure metallic gallium of 31.9 kJ/mol.

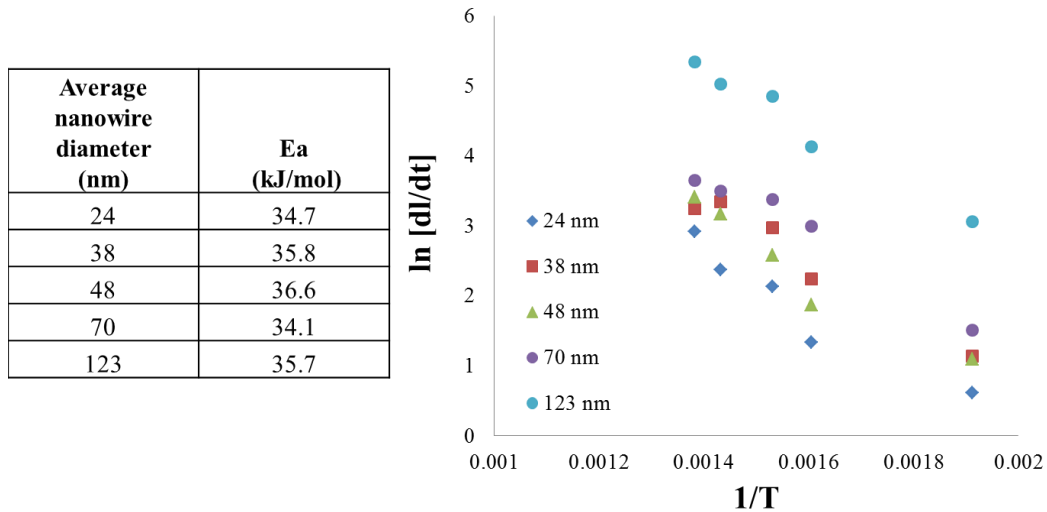


Figure 4.10.1 Arrhenius plot of growth kinetics as a function of temperatures obtained using Ga_2O_3 at constant diameters a) 24nm, b) 38nm, c) 48nm, d) 70nm and e) 123nm.

4.11 Comparison between growth kinetics obtained with Gallium oxide particle and metallic gallium derived droplets

In this subsection we show the recalculation of the activation energy for data shown in section 4.5 but for small nanowire diameters i.e. <200nm. The reason to recalculate the activation energy is that the samples prepared using Gallium oxide reduced nanoparticles did not lead to the growth of nanowires with diameter bigger than

200nm so no reasonable or direct comparison can be done with the activation energy for nanowires with diameter > 200nm. Also, it is well known that the very small nanowires exhibit the most interesting electrical, chemical and mechanical properties that can be exploited in several applications of great interest.

Figure 4.11.1 shows figure 4.8.1 replotted for nanowires with diameters less than 200nm. The previous value obtained when using nanowires bigger than 200nm is 31.9 kJ/mol, whereas the recalculated value when using only small nanowire diameters is 33.5 kJ/mol.

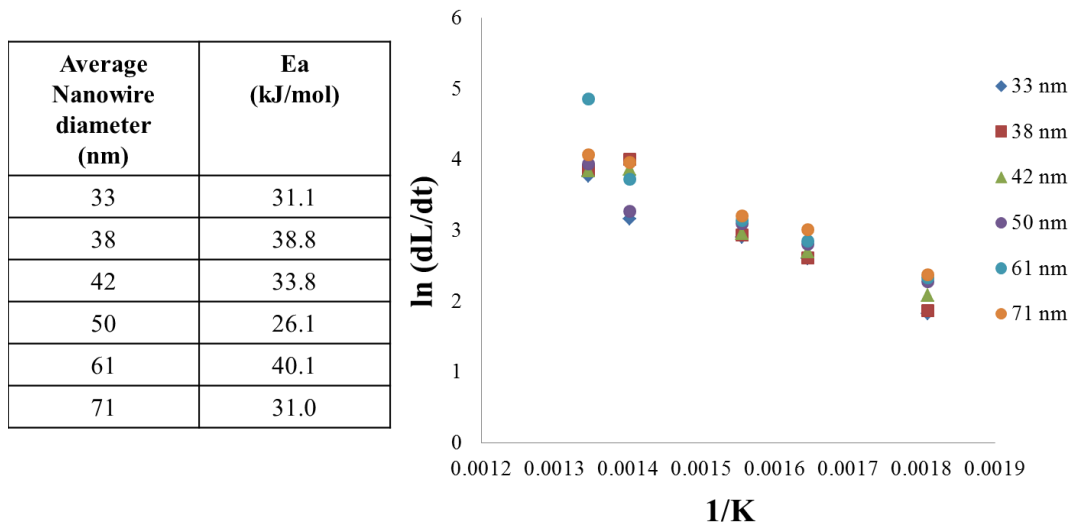


Figure 4.11.1 Arrhenius plot of growth kinetics as a function of temperature for nanowires with diameter <200nm at different temperatures and using Ga droplets of different sizes: a) 33nm, b) 38nm, c) 42nm, d) 50nm, e) 61nm and f) 71nm.

4.12 Summary

The silicon nanowire growth using Ga droplets is studied extensively using plasma excitation. The experiments suggest that there is no silicon nanowire growth observed in

the absence of plasma even at high temperatures. The presence of gentle plasmas is found to be essential for silicon nanowire growth when using Gallium. One particular characteristic of our nanowires synthesized using metallic Ga is that the nanowires less than 200nm in diameter exhibit a droplet diameter to nanowire diameter ratio around 1:1, whereas the nanowires with more than 200nm in diameter exhibit a droplet diameter to nanowire diameter ratio 2:1 or more.

Using reduced Gallia nanoparticles as Ga source, it was possible to observe highly homogeneous samples of silicon nanowires. The diameters and length of the nanowires synthesized showed to be narrowly dispersed. The average calculated activation energy value when using reduced Gallia is 35.4 kJ/mol. This is a slightly higher value than the 33.5 kJ/mol recalculated for small nanowire diameters when using metallic gallium. However, there is no significant difference found in the activation energy values when using different Ga sources.

Metallic Gallium		Ga ₂ O ₃ reduced	
Average Nanowire diameter (nm)	Ea (kJ/mol)	Average nanowire diameter (nm)	Ea (kJ/mol)
33	31.1	24	34.7
38	38.8	38	35.8
42	33.8	48	36.6
50	26.1	70	34.1
61	40.1	123	35.7
71	31.0		
	33.5		35.4

The synthesis of silicon nanowires using Gallia reduced nanoparticles can be used for growth of silicon nanowires uniformly on large areas of stainless steel and other thin metal foil substrates. The lowest temperature for the tip led growth of silicon nanowires using this approach is found to be $\sim 200^\circ \text{C}$.

CHAPTER 5

SYNERGISTIC EFFECTS OF GALLIUM ALLOYS FOR THE GROWTH OF SILICON NANOWIRES

In this chapter, the synthesis of silicon nanowires is investigated using Ga alloys with aluminum and gold. Gold represents as a catalytic metal which does not need plasma excitation for VLS growth of silicon nanowires. Aluminum is one of the low-melting point Group III metal which is not known for catalytic ability but has been shown to work with silicon nanowire synthesis using VLS growth at high temperatures without the use of plasma excitation. These alloys are investigated with their synergistic effect with plasma excitation toward VLS growth of silicon nanowires for two main reasons: (i) enable growth at temperatures as low as 100C with enhanced kinetics at low temperatures; and (ii) gain further insight into selective dissolution in molten metals with and without plasma excitation.

5.1 Synthesis of Silicon nanowires using Aluminum-Gallium alloy

5.1.1 Nanowire growth using Aluminum

Aluminum is a metal that belongs to the same group as gallium and is the third most abundant element in earth after oxygen and silicon. Aluminum has been itself an excellent choice for the growth of silicon nanowires. From a technological point of view, aluminum is a standard metal in silicon process line for device integration. Even further

as the formation of silicon nanowires using gallium has been observed to be hydride mediated, we can expect that the same mechanism could be extended for aluminum for one main reason: previous reports have shown the interaction between hydrogen and aluminum at high temperatures. This interaction leads to the formation of hydrides at relative high temperatures $\sim 1100\text{ }^{\circ}\text{C}$ ¹²⁵. As the interaction with hydrogen has been observed in the absence of plasma, it is expected that such interaction occur at lower temperature when plasma is used. In addition, the presence of gallium in Ga-Al alloys can enable the synthesis of silicon nanowires at much lower temperatures than those reported for when using aluminum alone. The lowest temperature reported to date when using only Al is $430\text{ }^{\circ}\text{C}$ ¹²⁶. Recently an effort to lower this temperature has been reported, making possible the synthesis of aluminum-catalyzed silicon nanowires after hydrogen radical treatment at $350\text{ }^{\circ}\text{C}$ ⁸. These results further support our hypothesis of hydride mediated synthesis. Even further, our work concludes that plasma and/or the presence of hydrogen radicals is essential when the metal-catalyzed silicon nanowires are synthesized at temperatures lower than metal–Si eutectic temperature.

Aluminum itself is a good candidate for the synthesis of silicon nanowires despite the fact that aluminum tends to oxidize easily making this synthesis challenging. Aluminum oxide is promptly formed when the metal is exposed to air, leading to a thin oxide layer covering the metal. As it can be observed in Figure 5.1.1 the eutectic point, the lowest temperature at which the Al-Si mixture will melt, is $577\text{ }^{\circ}\text{C}$. Thus, it can be expected to grow silicon nanowires around this temperature, or in the case of plasma at

even lower temperature than the eutectic as in the case of hydrogen radical-assisted method.

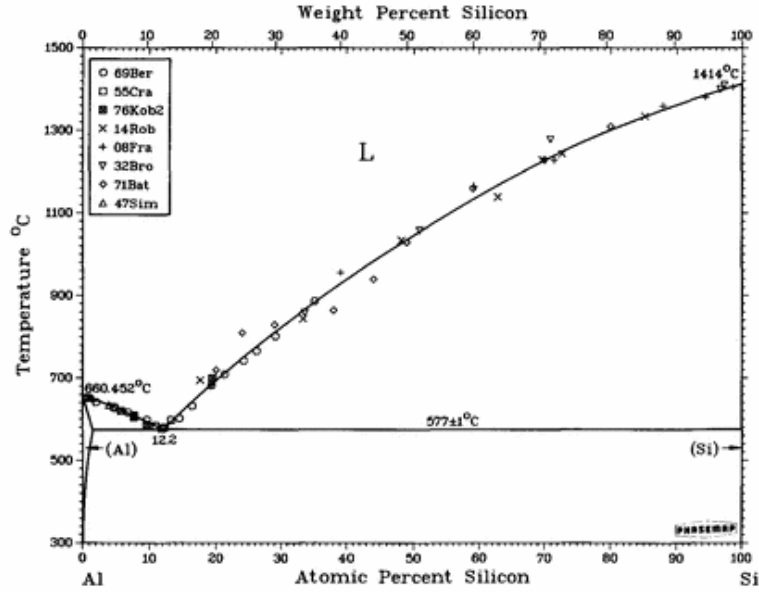


Figure 5.1.1 Al-Si binary phase diagram¹²⁷.

5.1.2 The Aluminum-Gallium alloy

As shown in Al-Ga binary phase diagram, the melting point of the AlGa alloys can be lowered with increasing Ga concentration. The melting point of Ga rich AlGa alloys increases with Al content from 29.3 °C. Nevertheless, one can have molten AlGa alloys at temperatures at 100 °C or lower (Figure 5.1.2.). All the different temperatures used for the growth of silicon nanowires are noted by the letters A, B, C, D, E and F and the detailed analysis of their composition is discussed below.

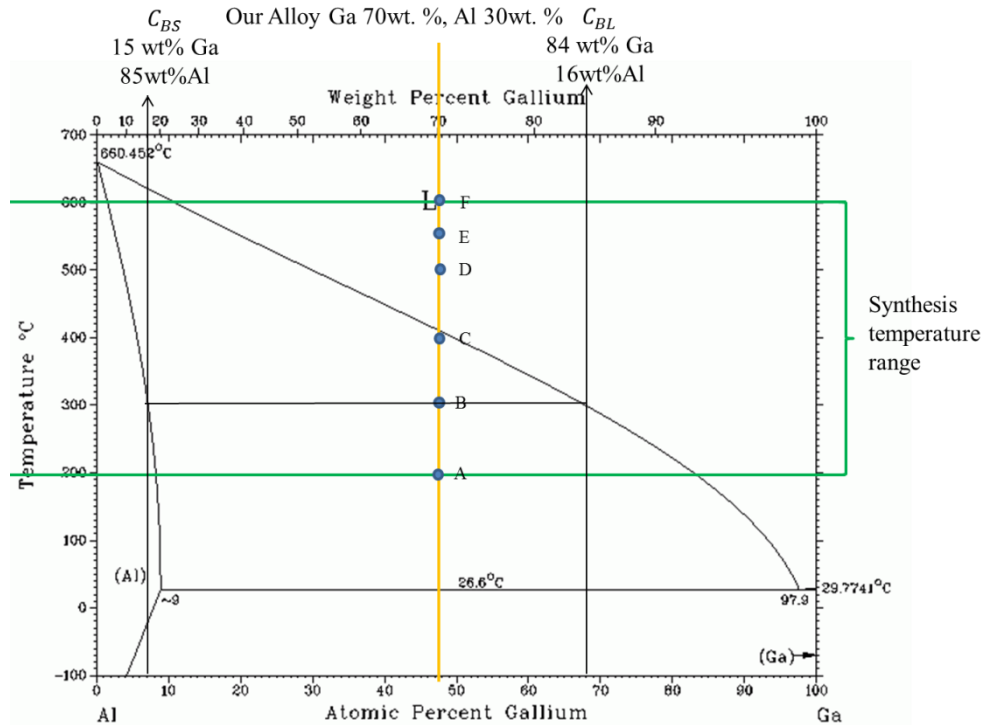


Figure 5.1.2 Al-Ga phase diagram¹²⁸

From Figure 5.1.2 it is possible to observe that 70 wt% Ga, 30 wt% Al Ga-Al mixture can be molten for points C, D, E and F (or temperatures above 400C). Below 400 C, the alloy will segregate into two phases, i.e., one is solid and another is liquid. Using tie-line between solidus and liquidus lines for Al-Ga alloys, the following segregation will happen. Using lever rule, one can estimate the relative percentages of liquid and solid alloys present at different temperatures below 400C for 70:30 wt% Ga-Al alloy. The estimated fractions and compositions of segregated phases are summarized below in Table 5.1.2.

Table 5.1.2 Compositions of the liquid and solid phases formed at different temperatures from the 70 wt% Ga and 30 wt% Al alloy.

Alloy	Temperature [°C]	Composition of the solid phase wt. %	Composition of the liquid phase wt. %	Weight percent of the alloy as liquid phase	Weight percent of the alloy as solid phase
A	200	16 wt. % Ga 84 wt. % Al	93 wt. % Ga 7 wt. % Al	52%	48%
B	300	15 wt. % Ga 85 wt. % Al	84 wt. % Ga 16 wt. % Al	66%	34%
C	400	11 wt. % Ga 89 wt. % Al	72 wt. % Ga 28 wt. % Al	95%	5%
D	500			100	
E	550			100	
F	600			100	

As it can be observed from the Table 5.1.2 all the alloys at different temperatures are liquid phase rich. Since Aluminum is able to interact with hydrogen at high temperatures forming hydrides in the absence of plasma it is possible to expect that the Al-Ga alloy can lead to the growth of silicon nanowires in the absence of plasma.

However, several attempts to grow silicon nanowires using the Al-Ga alloy failed even at temperatures as high as 600° C in the absence of plasma excitation.

The Aluminum-Gallium alloy was prepared by mixing ~ 1056.9mg of an Aluminum slug (99.99% purity Alfa Aesar) and 2388 mg of Gallium (99.99% purity, Sigma Aldrich). The alloy composition is about ~ 30.7 wt% of Al and 69.3 wt% of Ga. It is important to mention that this alloy has a powdery texture while making it difficult to spread the alloy on to the substrate in ambient, thus the films prepared with this alloy are remarkably thicker in comparison with the Ga films. (Figure 5.1.3).

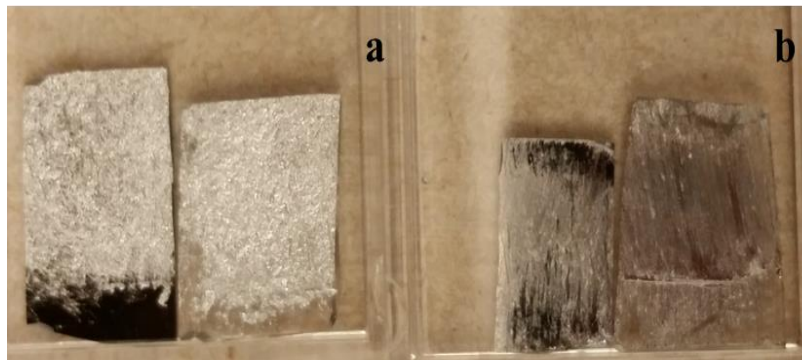


Figure 5.1.3 Optical photographs of a) Al-Ga alloy and b) Ga films on different substrates.

The Al-Ga alloy was exposed to hydrogen plasma in order to form droplets using a 2% H_2 /Ar mixture at 70W and the typical growth temperature for silicon nanowires (400 °C) for 30min. The resulting Al-Ga droplets on a quartz substrate can be observed in Figure 5.1.4. It is worth to remark that the droplets formed with this alloy are not completely spherical and the substrate is not all covered with droplets as in the case of the

Au-Ga alloy showed later or Ga itself. Thus this alloy shows a higher degree of wetting behavior comparing to that of Au-Ga and Ga.

The formation of pure Al alloys droplets is not a trivial task in itself. Pure Al and its alloys are known to be highly sensitive to oxidation and the presence of negligible amounts of oxygen is enough to instantaneously form a monolayer of Aluminum oxide at room temperature¹²⁹.

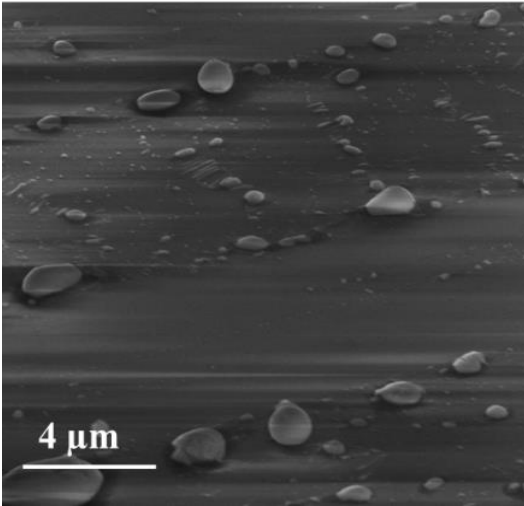


Figure 5.1.4 SEM image of the Al-Ga alloy droplets on a quartz substrate after a treatment with H₂ plasma at 400 °C and 30min.

The EDAX analysis was performed on both films and individual droplets. Figure 5.1.5 shows the SEM image of an Al-Ga alloy film and the dispersion of both metals in the film. The film as well as the droplet showed a 30 wt. % of Al as expected from the starting materials. Figure 5.1.5 shows the Al-Ga film and the distribution of both compounds. Being Ga represented in green color and Al in purple color, it is clear that

the Ga content in this film is much higher than the Al content. The data also show uniform dispersion of Al rich regions throughout the film.

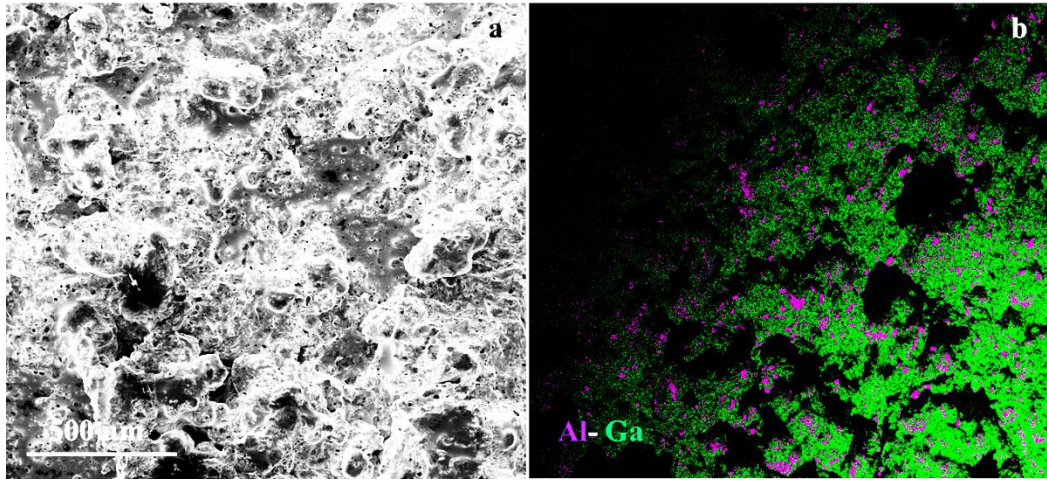


Figure 5.1.5 a) SEM image of an Al-Ga film on a quartz substrate, b) Elemental mapping for Al and Ga in the film.

The elemental mapping in Figure 5.1.6 shows the distribution of Al and Ga within the droplet. The data confirms the weight percent calculated from the Al and Ga weights used to prepare the alloy (30 wt. % and 70 wt. % respectively). Surprisingly, the Ga seems to be on the surface of the droplet, whereas the core of the droplet seems to be rich in Al. Thus, the distribution of the metals within the droplet is clearly marked. However, it is not clear whether such segregation of metals from the alloy could be different during synthesis at different temperatures.

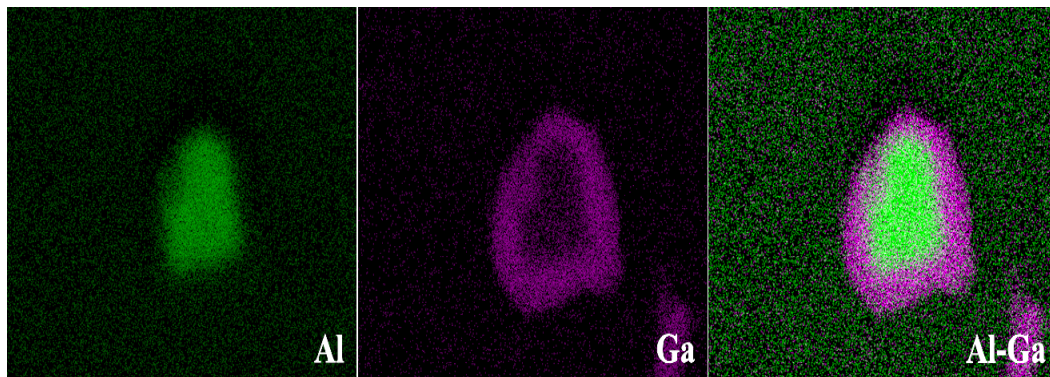


Figure 5.1.6 Spatial EDAX mapping for Al and Ga elements over an Al-Ga alloy droplet.

5.1.3 Growth of silicon nanowires using Al-Ga alloys

The growth of Silicon nanowires by UHV-CVD using silane as precursor and Aluminum has already been successfully reported at temperatures between 430 °C-490 °C with a tapered morphology. As expected, the growth of Silicon nanowires in the tip led fashion happened at lower temperatures in the presence of both plasma and Al-Ga alloy. In our experiments, the lowest temperature at which Silicon nanowires resulted due to tip led growth is 300 °C. Below 300 °C, the experiments resulted in the bulk nucleation of silicon nanowires and this could be due to the presence of bigger Al-Ga droplets. An important observation is that in the absence of plasma there is no growth of silicon nanowires using this alloy, even at relative high temperatures ~600 °C as shown in Figure 5.1.4. However, the surprising aspect is that the growth of silicon nanowires using the Al-Ga alloy were not observed even at relative high temperatures without plasma even though expected from prior work with pure Aluminum. The presence of small amounts of

oxygen through back diffusion could have hampered the growth of silicon nanowires without the presence of plasma at high temperatures.

The use of plasma in our experiments enabled the presence of hydrogen radicals that seem essential for the nanowire growth at low temperatures. The presence of hydrogen radicals ensures the Ga-H intermediate formation and possibly the Al-H interaction similar to that discussed in hydrogen interaction with pure aluminum metals in a previous report¹³⁰. The nanowires grown at 400 °C using the Al-Ga alloy in the presence of plasma showed a droplet diameter size bigger than the nanowire diameter, in some cases reaching the 2:1 ratio or more similar to that observed using pure Ga droplets as discussed in Chapter 4. As the synthesis temperature was increased the nanowire morphology became tapered. See Figure 5.1.7. The temperature where the nanowires seem to be clearly tapered is 550 °C. This is the common temperature for the synthesis of silicon nanowires using only Aluminum. As it has been previously observed the tapering of the nanowires can be strongly reduce by reducing the growing temperature¹²⁶. The tapered morphology implies that it is difficult to grow longer nanowires as the catalyst cluster at tips can disappear gradually during growth. So, it is important to avoid and control the tapering with growth. Our experiments show that the use of Ga rich Al alloys at temperatures lower than 500 °C, one can avoid tapering of silicon nanowires.

As already mentioned we observed that the synthesized nanowires began to show tapering at 550° C with this alloy, thus the highest temperature to obtain non-tapered nanowires with this alloy was found to be 500° C.

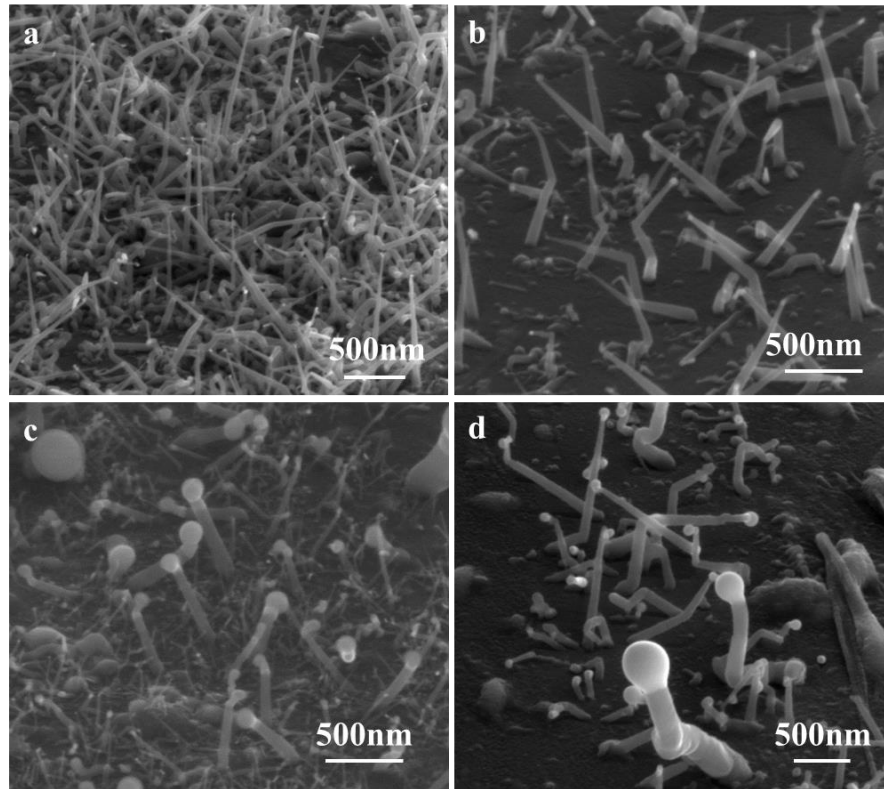


Figure 5.1.7 SEM images of silicon nanowires synthesized at different temperatures using the Al-Ga alloy: a) 600 °C, b) 550 °C, c) 500 °C and d) 400 °C.

The SEM images of silicon nanowires synthesized using Ga-Al alloys at temperatures from 200 °C to 300 °C are shown in Figure 5.1.8. The data in Figure 5.1.8 (a) shows tip led growth of silicon nanowires at 300 °C. In addition to silicon nanowire growing with Ga-Al alloy droplet at its tip, the presence of a silicon blanket on the substrate characteristic is also clearly seen. Figure 5.1.8 (b) shows the sample grown at 200 °C and it shows that bulk nucleation of silicon nanowires from big droplet. Even

though, it is possible to observe small droplets in this sample, they have several nanowires coming out of them as in the already reported ‘rope-like’ bulk precipitation of silicon nanowires as discussed in Chapter 4.

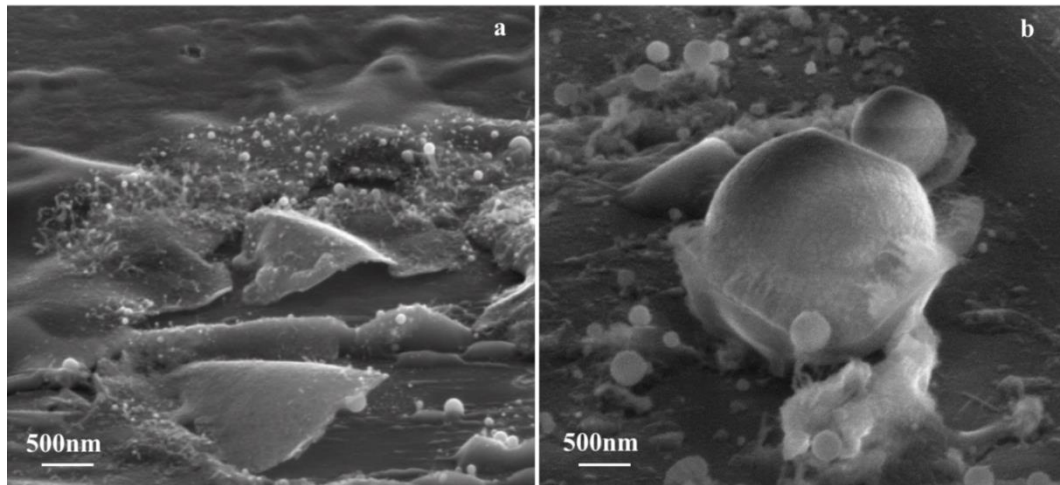


Figure 5.1.8 SEM images of silicon nanowires synthesized using an Al-Ga alloy at a) 300 °C and b) 200 °C.

The EDX analysis of the droplet on the tip of silicon nanowire grown at 500 °C is shown in Figure 5.1.9. The data shows smaller Al peak compared to that for Gallium indicating Ga rich Ga-Al alloy being present.

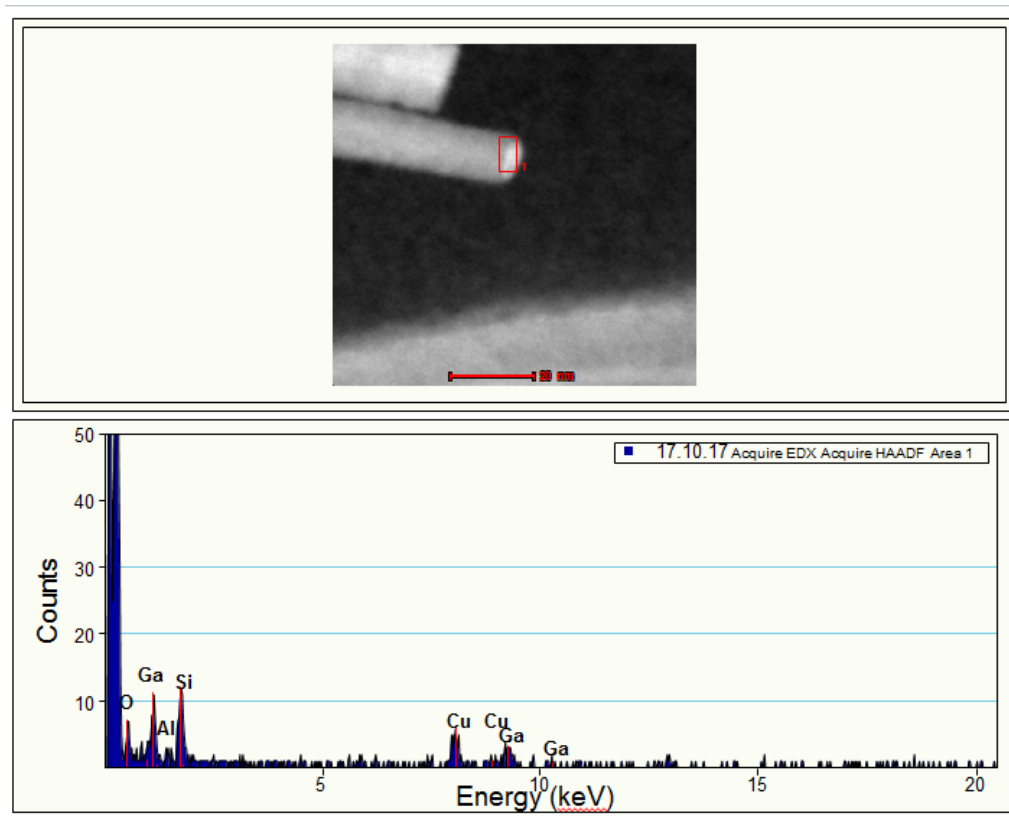


Figure 5.1.9 EDX analysis of an Al-Ga droplet of a silicon nanowire synthesized at 500 °C.

5.1.4 Growth kinetic analysis of the silicon nanowires synthesized using Al-Ga alloy

The kinetics for silicon nanowire growth as a function of nanowire diameter and temperature is shown in Figure 5.1.10. The resulting activation energies for various diameters are estimated and tabulated in Table 5.1.10

Table 5.1.10 Activation energy values obtained silicon nanowires grown using the Al-Ga alloy.

Average Nanowire diameter (nm)	Ea (kJ/mol)
32	49.1
54	48.3
63	48.8
84	47.3
100	49.6

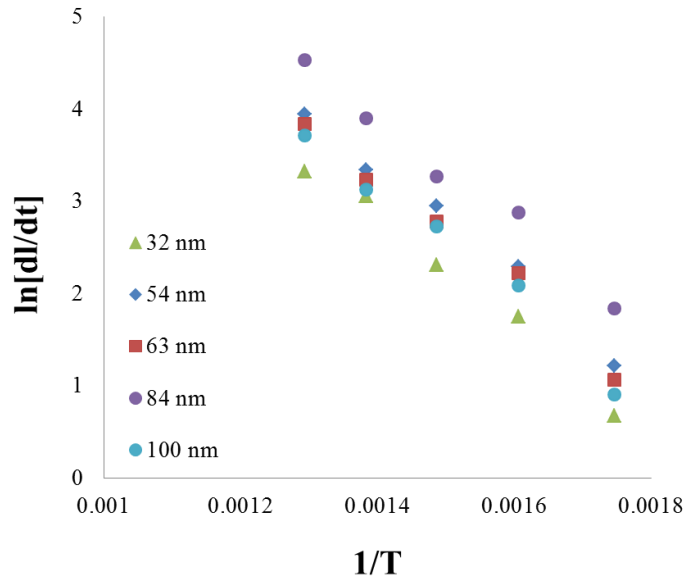


Figure 5.1.10 Arrhenius plot for growth kinetics as a function of temperature for silicon nanowires with different diameters for the Al-Ga alloy.

As indicated in the Table 5.1.10 the average calculated activation energy values for the Al-Ga alloy is 48.6 kJ/mol. This activation energy value is bigger than the calculated value when using either reduced Gallia (35.4 kJ/mol) particle or Gallium metal (33.5 kJ/mol). The low activation barrier for Ga metal explains the higher growth rate observed when using only Gallium and also validates Gallium as a better catalyst for this

reaction compared to the Al-Ga alloy. The higher activation energy values suggest that the addition of Aluminum does not favor the silicon nanowire growth reaction. The observations of sluggish kinetics are not expected and need further exploration. Since both Ga and Al have been used separately as catalyst for the synthesis of silicon nanowires it is possible to treat this pair as cocatalysts having in mind that by definition a catalyst is a substance that modifies the rate of reaction. In the case of Ga and Al alloy, this pair does not act in the optimum cooperative way as a good duo of catalysts should do.

However, this alloy allowed to have a molten metal at relative low temperatures leading to the observed synthesis of silicon nanowires at the lowest temperature of 300 °C, the lowest reported from our knowledge when using pure Al. Thus, even though the activation energy value was higher than the one for pure Ga, the use of this alloy allowed the synthesis of silicon nanowires at low temperature.

5.2 Synthesis of Silicon nanowires using Gold-Gallium alloy

5.2.1 Gold for nanowires growth

The growth of silicon nanowires has been typically performed using Gold as catalyst. Gold offers several advantages such as high chemical stability, forms a eutectic with silicon at 363 °C and its nanoparticles are stable and easily available. The above reasons make gold as an outstanding candidate for silicon nanowire growth. However, gold is incompatible with silicon based electronics since it creates deep level defects in Si. Also, the gold is difficult to be removed from samples making it as a major challenge.

Figure 5.2.1 shows the Au-Si phase diagram showing the eutectic Au-Si. The synthesis of silicon nanowires using gold has been shown to be possible at temperatures near the eutectic²⁸ (380° C), slightly above its eutectic temperature when using plasma. Without the use of plasma, typical temperatures are much above 550C when using gold as catalyst¹³¹.

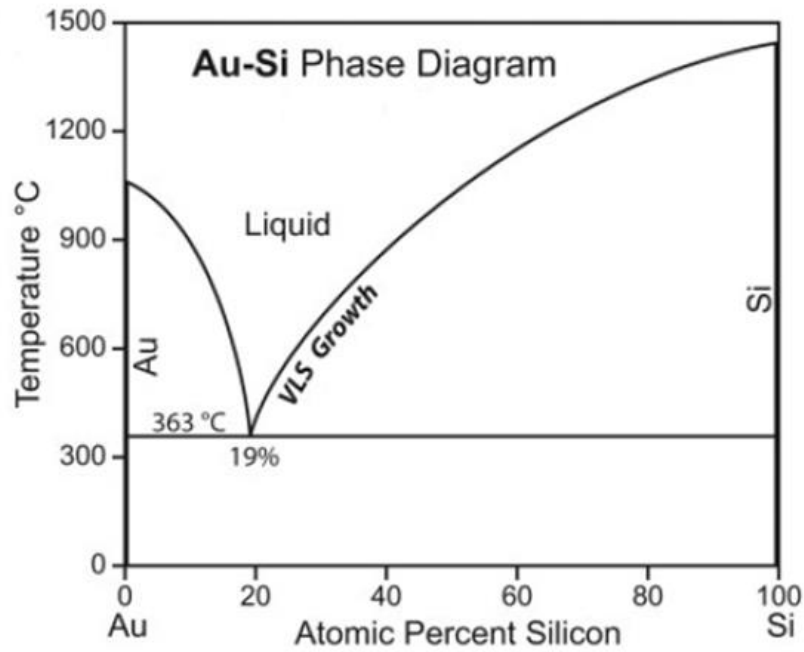


Figure 5.2.1 Au-Si phase diagram.¹³¹

5.2.2 The Gold-Gallium alloy

The Gold-Gallium alloy has been previously used for the growth of nanostructures in order to allow low temperature synthesis and achieve better growth rates¹³². This is because from the catalytic point, gold is a better candidate for the synthesis of semiconductor nanostructures and gallium will allow a lower eutectic temperature leading to an overall low temperature synthesis. From the Au-Ga binary

phase diagram in Figure 5.2.2, Au rich alloys do not melt at temperatures lower than 500 °C but the Ga rich alloys can be molten at temperatures lower than 100 °C. The different temperatures used here for the growth of silicon nanowires are defined by the points A, B, C and D which composition will be later described in detail using the phase diagram.

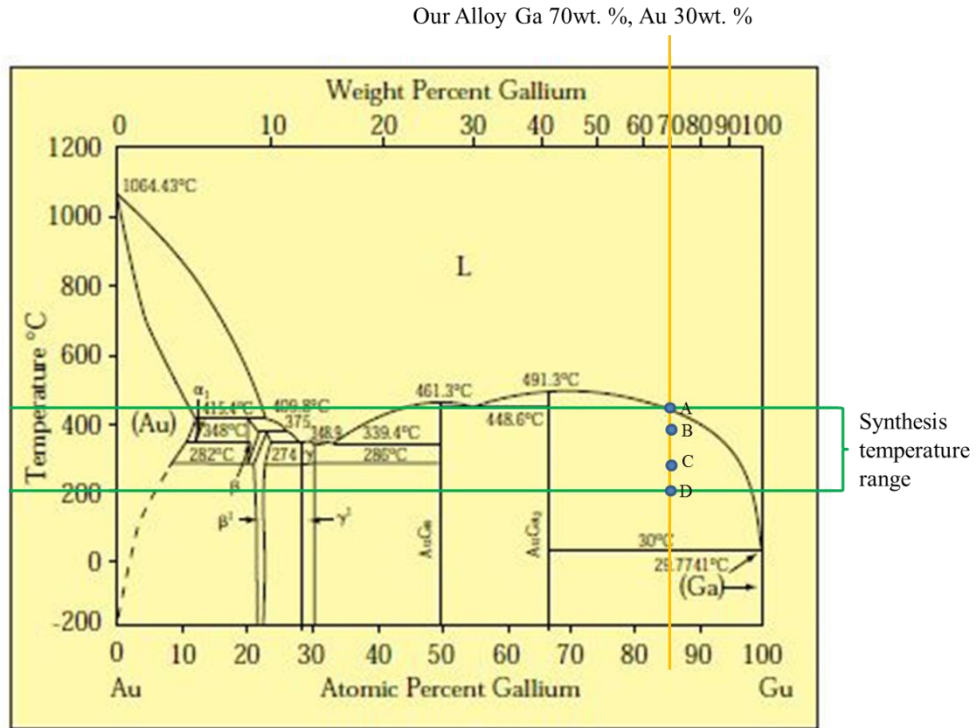


Figure 5.2.2 Au-Ga binary phase diagram.

The Au-Ga alloy was prepared as follows: a thin layer of metallic Ga was spread on a substrate followed by a sputtered thin layer of Au for 5 minutes. In order to form droplets from this alloy we expose it to a 2% H_2 /Ar mixture at 400° C, 70W for 30min. The Au-Ga droplets alloy can be observed in Figure 5.2.1. The compositional analysis was performed for the 30%Au-70%Ga by wt. is analyzed at various temperatures. The data obtained is

summarized in Table 5.2.1. As indicated, the data shows that the original alloy will be molten until 450 °C. Below 450 °C, the alloy will segregate into two phases, a solid phase and a liquid phase. As indicated below, at temperatures as low as 200 °C, majority of the alloy will be in molten phase with Ga rich composition. The solid part of the alloy seems to be equal in composition.

Table 5.2.1 Compositions of the liquid and solid phases formed at different temperatures from the 70 wt% Ga and 30 wt% Au alloy.

Alloy	Temperature [°C]	Composition of the solid phase wt. %	Composition of the liquid phase wt. %	Weight percent of the alloy as liquid phase	Weight percent of the alloy as solid phase
A	450			100	
B	380	41 wt. % Ga 59 wt. % Au	80 wt. % Ga 20 wt. % Au	78%	22%
C	250	41 wt. % Ga 59 wt. % Au	63 wt. % Ga 37 wt. % Au	63%	37%
D	200	41 wt. % Ga 59 wt. % Au	60 wt. % Ga 40 wt. % Au	60%	40%

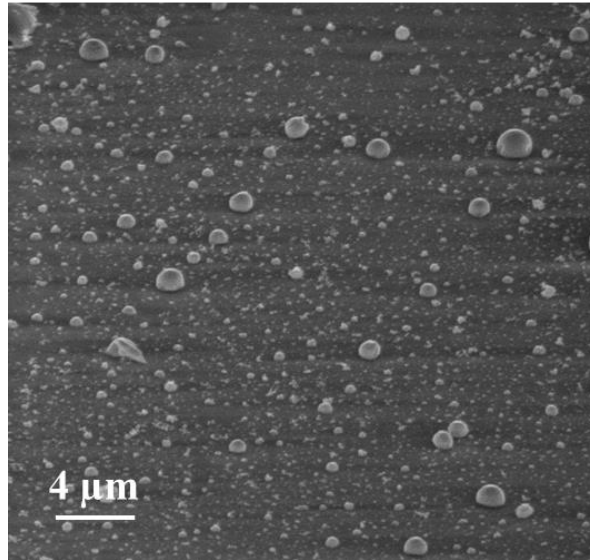


Figure 5.2.3 SEM image of the Au-Ga alloy droplets formed after exposure to hydrogen plasma at 400° C for 30min.

EDX analysis of the Au-Ga alloy droplets was performed. See Figure 5.2.4, The EDX mapping shows the distribution of Au and Ga within the droplet. Surprisingly, the Ga rich alloy seems to be covering the surface of the droplet, whereas the core of the droplet seems to be rich in Au. This observation is similar to the case of the Al-Ga alloy droplets. However, it was possible to observe that the formation of droplets with this alloy (Au-Ga) is quite more challenging than the formation of pure Ga droplets. The distribution of the metals in the droplet change with the temperature.

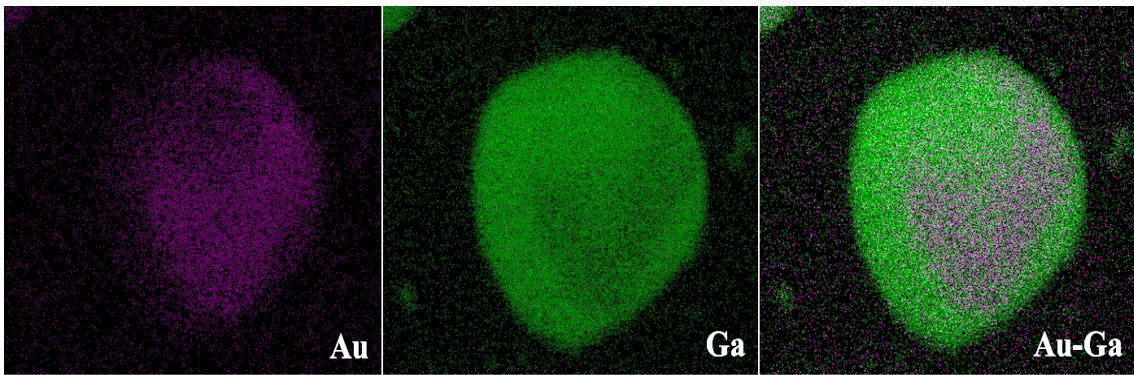


Figure 5.2.4 Spatial EDAX mapping for Au and Ga elements over an Au-Ga alloy droplet.

5.2.3 Synthesis of silicon nanowires using Au and the Au-Ga alloy

Several experiments were performed to confirm the catalytic effect of pure Au by using gold covered substrates with and without plasma exposure and compared them with those using Au-Ga alloy at the same conditions. See SEM images in Figure 5.2.5. These sets of experiments were performed at 400 °C, a relatively low temperature for the growth of silicon nanowires using gold. The images in Figure 5.2.5 (a) and (b) correspond to the substrates covered with the alloy, Au-Ga. As it can be observed in Figure 5.2.5 (a), the use of Au-Ga alloy with plasma at 400 °C resulted in silicon nanowire growth. At the same time, when the same alloy is only heated without plasma exposure, a thin layer of silicon covered both the substrate and the alloy droplets. Thus, there was no selective dissolution of silicon into the droplets without plasma excitation.

Figures 5.2.5 (c) and (d) show the SEM images of substrates covered with only Au. Interestingly, no nanowire growth could be observed even in the presence of plasma. The experiment shows the necessity of a temperature higher than 400 °C when

synthesizing silicon nanowires using Au and SiH₄ system. However, the presence of plasma when using Au helps to the formation of small gold droplets as observed in Figure 5.2.5 (c), whereas there is no Au droplet formation in the absence of plasma. In this case, the Au film formation is clearly observed. Thus, the necessity of plasma for small droplet formation is evident.

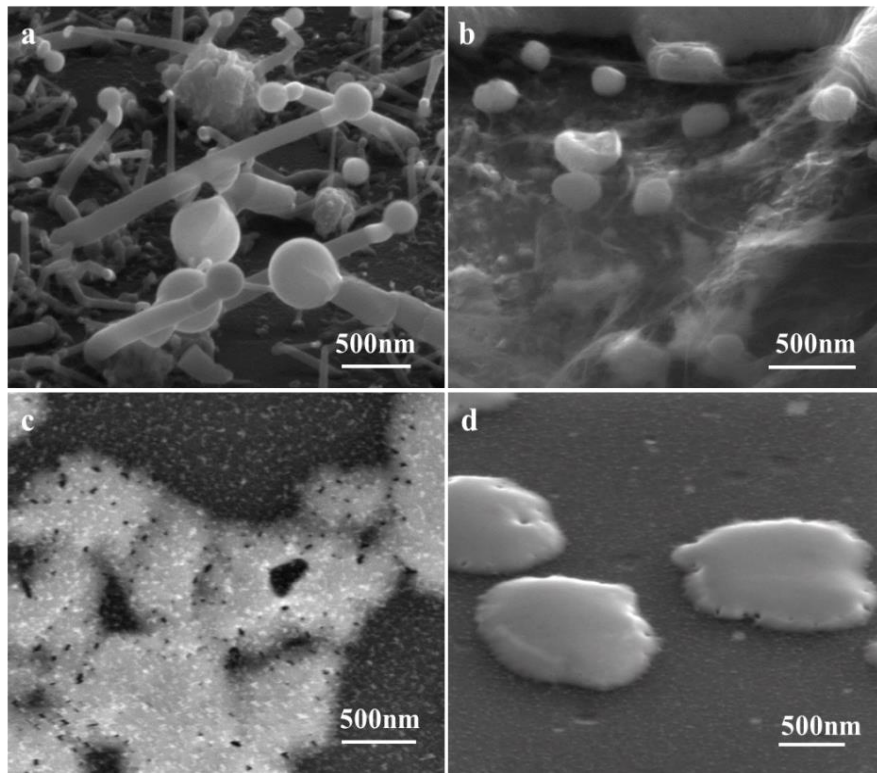


Figure 5.2.5 SEM images of different substrates heated at 400 °C a) Au-Ga alloy exposed to plasma, b) Au-Ga without plasma exposure, c) Au exposed to plasma and d) Au without plasma exposure.

The silicon nanowire growth using only Au without any plasma excitation was observed until reaching high temperatures, around 700 °C as it can be observed in Figure 5.2.6. The synthesized silicon nanowires using only Au and no exposure to plasma

showed to be kinked and tapered. The sample also showed a high density of silicon nanowires. It is important to observe that in the absence of plasma at relative low temperatures ($\sim 450^\circ\text{C}$) Au alone formed films and no droplet formation was observed on the substrates.

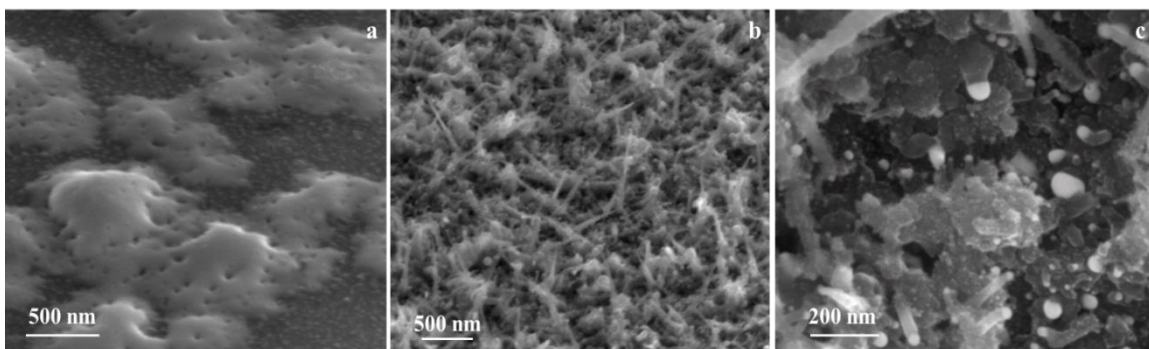


Figure 5.2.6 SEM images of samples covered with Au and heated without the use of plasma but using SiH_4 at a) 500°C , b) 700°C and c) 700°C higher magnification image of (b).

We can conclude that the growth of silicon nanowires using Au can be possible either at the eutectic or higher temperatures in the presence of plasma. These observations lead to hypothesize that the metal hydrides either occur at high temperature or in the presence of plasma. These hydrides are important intermediates for the catalytic dissolution of silicon species into Gold. This idea can be supported by the reports of transition metal hydrides which are well-established complexes that are key intermediates in several homogenous and heterogeneous Au catalyzed reactions¹³³. Particularly, Gold hydrides have been postulated as intermediates in numerous homogeneously catalyzed hydrogenations^{134, 135} and hydrosilylations¹³⁶. Despite the widely use of Gold as catalyst,

the importance of its hydrides have attracted much attention just recently¹³⁷ due to its importance in the catalytic process. In our case, the presence of Au hydrides intermediate species could be happening as in the case of Al, at high temperatures or either produced by the synergism between the molten metal and plasma.

Several experiments were performed at different temperatures using Au-Ga alloys to understand the low temperature limit. Figure 5.2.7 shows the silicon nanowires synthesized using the Au-Ga alloy at different temperatures: 450 °C, 380 °C, 250 °C and 200 °C. As it can be observed the nanowires exhibit very small diameter, less than 100nm and the droplet to nanowire diameter is typically around 1:1. The lowest temperature for growing silicon nanowires using this alloy was found to be 200 °C. The SEM images in Figure 5.2.7 show translucent contrast for silicon nanowires indicating that they may be tubes. These observations need to be explored to see if the core-shell segregation of molten and solid phases in the droplet at synthesis temperatures could result in tubular growth.

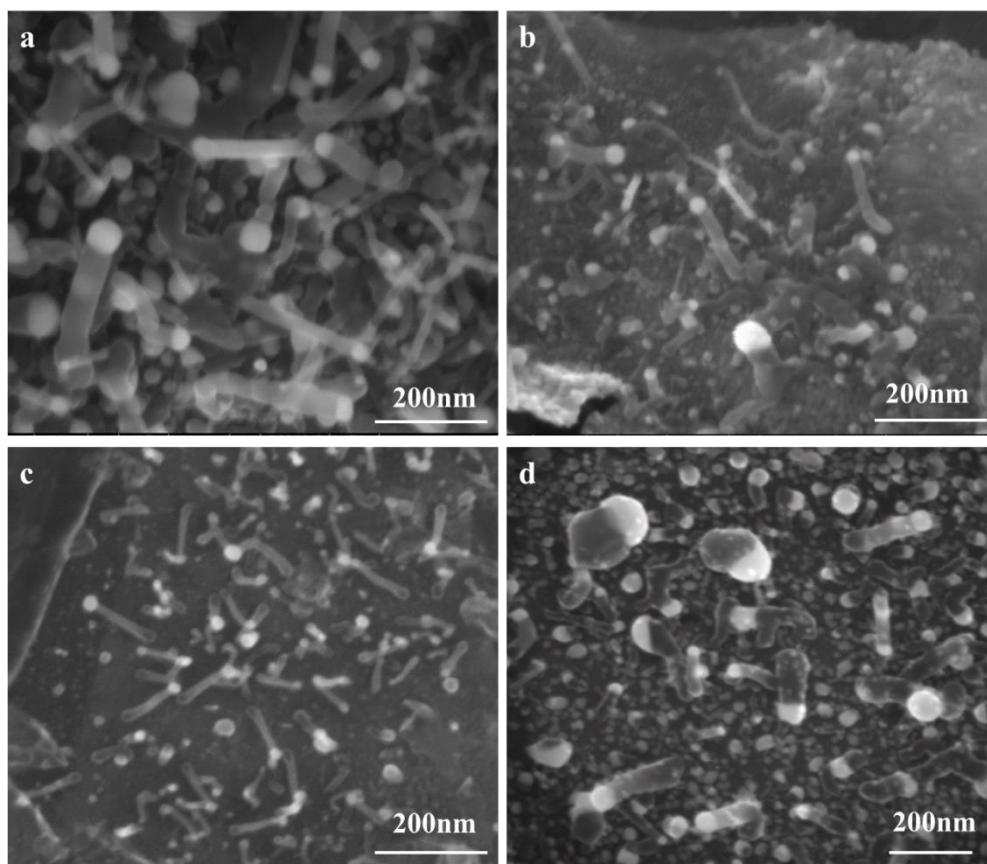


Figure 5.2.7 SEM images of silicon nanowires synthesized using the Au-Ga alloy and 70W of plasma at a) 450 °C, b) 380 °C, c) 250 °C and d) 200 °C.

In order to confirm the presence of Au in the synthesized nanowires we perform compositional profile analysis as shown in Figure 5.2.8. As it can be observed from this analysis, the presence of Au is confirmed in the alloy droplet.

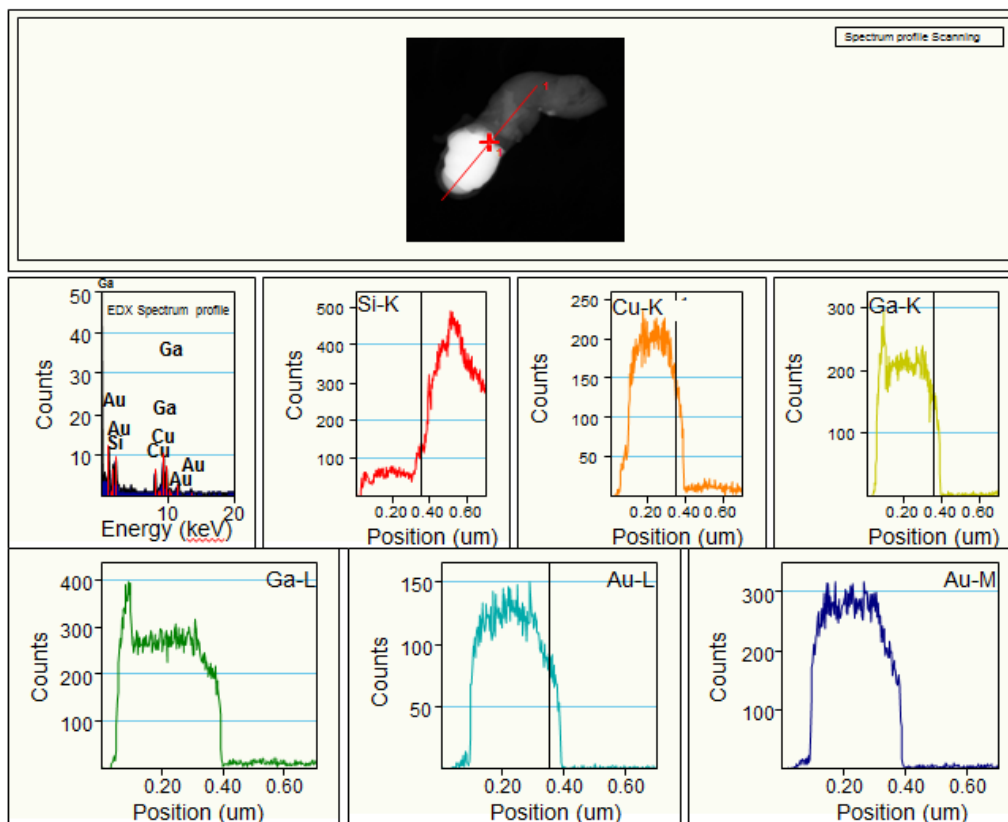


Figure 5.2.8 TEM-EDS line profile analysis of nanowire tip showing the presence of gold.

5.2.4 Kinetic analysis of the silicon nanowires synthesized using Au-Ga alloy

Figure 5.2.9 shows the kinetics data for nanowires grown using Au-Ga alloys.

Table shows the estimated activation energy values for various diameters.

Table 5.2.2 Activation energy values obtained for silicon nanowires grown using Au-Ga alloy as a function of nanowire diameters.

Average Nanowire diameter (nm)	Ea (kJ/mol)
24	32.1
27	32.8
30	31.2
41	32.5
51	33.6
115	32.3

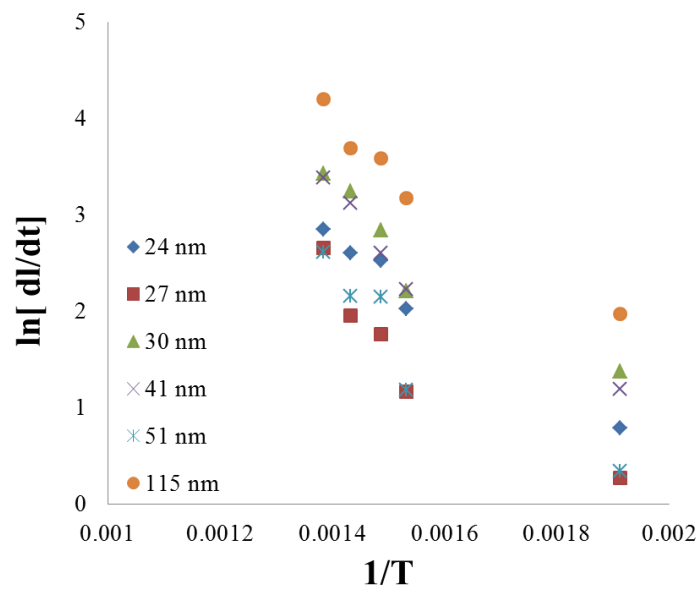


Figure 5.2.9 Arrhenius plot of growth kinetics as a function of temperature for silicon nanowires of different sizes a) 24nm, b) 30nm, c) 41nm, d) 51nm and e) 115nm for the Au-Ga alloy.

The average calculated activation energy value for the Au-Ga alloy is 32.4 kJ/mol. This activation energy value is smaller than the calculated for the Al-Ga alloy (48.6 kJ/mol). Comparing these two with the activation energy value calculated when using Gallium metal (33.5 kJ/mol) and reduced Gallia (35.4 kJ/mol) it can be stated that:

$$E_a (\text{Au-Ga}) < E_a (\text{Ga metal}) < E_a (\text{reduced Gallia}) < E_a (\text{Al-Ga})$$

$$32.4 \text{ kJ/mol} < 33.5 \text{ kJ/mol} < 35.4 \text{ kJ/mol} < 48.6 \text{ kJ/mol}$$

This result explains the preference of Au for silicon nanowire growth based on growth kinetics data and estimated activation barrier. However, the differences in the estimated activation barrier values are small, it is difficult to conclude the beneficial role of gold in both lowering the synthesis temperature and enhancing the kinetics. But, the segregation behavior of Au-Ga alloys into molten phase as shell and the solid phase as core, it presents as an interesting system for growing nanotubes of different materials systems using VLS mode,

Remarkably, the use of Au-Ga alloys led to small nanowire diameters comparing to Gallium. This is could be explained by the preference of Gallium to agglomerate in to bigger droplets as the temperature increases. Table 5.2.1 shows the lowest temperature reached for the synthesis of silicon nanowires using different catalyst as well as the calculated activation energy for the proposed approach and the data available in the

literature. It is important to mention as reference that the activation energy for Si CVD when using SiH_4 is 144-167kJ/mol¹³⁸.

Table 5.2.3 Summary of the silicon nanowire growth temperatures and kinetics obtained in this work compared with that from literature.

Catalyst	Lowest synthesis temperature for silicon nanowires (this work) [°C]	Type of growth	Lowest synthesis temperature for silicon nanowires (reported) [°C]	Activation energy [kJ/mol]	Reported activation energy for the neutral gas process [kJ/mol]
Gallium metal	210	Bulk nucleation	NA	NA	NA
	335	Tip led	500-600 ⁵⁶	33.5	
Reduce Gallia	180 ⁵⁵ with chloro-silanes chemistry	Tip led	NA	35.4	NA
	200 with SiH ₄ chemistry				
30% Au-70% Ga alloy	200	Tip led	380 with pure Au ²⁸	32.4	89 kJ/mol for pure Au using SiH ₄ ¹³⁹ 59kJ/mol for 75% Au-25% Ga alloy using SiH ₄ ¹⁴⁰
30% Al-70% Ga alloy	300	Tip led	350 with pure Al ⁸	48.6	255.2 kJ/mol for pure Al using SiH ₄ ¹⁴¹
	200	Bulk nucleation	NA	NA	

As it can be observed from this table the use of plasma and the use of an appropriate cocatalyst, in this case Au, can make possible the synthesis of silicon nanowires at lower temperatures that the reported in the literature with pure metals. Also the activation energies are considerably smaller due to the cocatalyst effect as well as the synergism between the molten metals and plasma.

5.3 Segregation behavior of Ga alloys

The alloys of 30 wt. % Al/Au and 70wt. %Ga exhibit segregation into two phases: a liquid phase and a solid phase. The segregation led to core-shell type droplet with solid phase in the core and liquid alloy as shell.

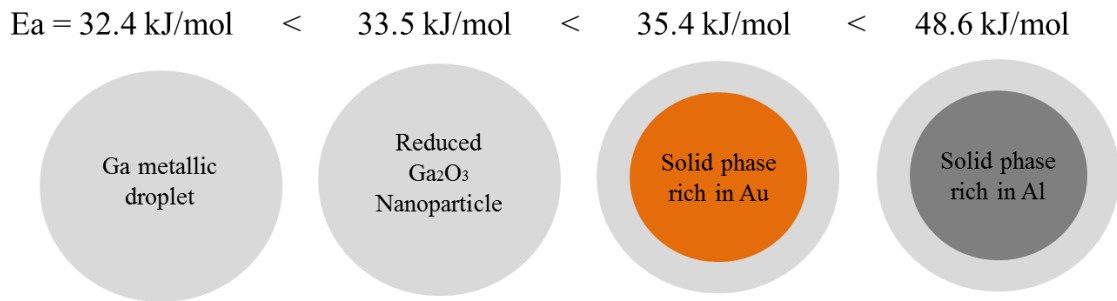


Figure 5.3.1 Schematics illustrating segregation behavior of phases in various Ga alloys.

The core-shell segregation results from the tendency of the low surface tension component to be at the surface¹⁴². Surface tension is caused by the inward attraction of molecules at a boundary. This attraction produces curvature of free liquid surfaces, and causes a pressure difference to exist at the curved boundary.

Table 5.3.1 Surface tension values for Gallium, Aluminum and Gold¹⁴³.

Metal	Surface Tension ¹⁴³ mN/m
Ga	711
Al	850–1100
Au	1145

As it can be observed from Table 5.3.1, despite the fact that Al is one of the most widely used metals, there is still a great uncertainty on the intrinsic value of its surface tension. This is undoubtedly due to the high sensitivity of surface properties of molten Al to oxygen¹⁴⁴. Surface tension of Al at a temperatures close to its melting point measured by different authors and different techniques and its resulting value lies within the range 850–1100 mN/m (Table 5.3.1).

The low surface tension of the Ga comparing with Al and Au explains the tendency of the Gallium rich phase (the liquid phase) to be on the surface of the alloy covering the Al or Au solid rich phase respectively. Regarding the activation energy it is possible to observe that there is not a remarkable difference when using Ga₂O₃ reduced nanoparticles, molten Ga and Au-Ga alloy for the growth of silicon nanowires. However, it is important to remember that at the shell of the catalytic metal particle exists a rich Ga molten metal that can explain the lack of difference.

Nevertheless, the case of Al is quite different since the activation energy for this molten alloy is higher. The wt. % of Aluminum in the top liquid phase, where the reaction for the growth of silicon nanowires happens, is smaller than the wt. % of Gold when comparing these two alloys. The difference in the activation energy value can be only attributed to a better cocatalytic effect of Au comparing with Al. Contrary to gold, which is chemically stable, aluminum is reactive in the ambient air. Aluminum can be easily oxidized to form aluminum oxide Al_2O_3 . Aluminum oxide is a strong material that is extremely hard to reduce. The presence of aluminum oxide, which is not taken into account in the analysis of the binary phase diagram, disturbs the VLS crystal mechanism by preventing the diffusion of silicon vapor through the molten alloy¹⁴⁵. This layer is a diffusion barrier for silicon atoms. Despite this we prepared our alloy in an inert atmosphere rich in Argon, and post heated it in order to spread it on the substrates at ambient conditions. This resulted in a small diffusion of oxygen in to the alloy that promptly could react with Al. This small oxygen content can be observed in Figure 5.1.10 EDX analysis of an Al-Ga droplet of a silicon nanowire synthesized at 500 °C. Furthermore, the activation energy value for the synthesis of silicon nanowires when using pure Al has been calculated to be $\approx 255.2 \text{ kJ/mol}$ ¹⁴¹. This value can explain the preference of Au as cocatalyst for the growth of silicon nanowires when used along with Ga. Since for pure Au the activation energy has been calculated to be 89 kJ/mol , which is clearly a smaller value. However, the cocatalytic effect of Al and Au needs to be further studied and completed as a proposed future work by making an exhaustive analysis of these alloys at different temperatures.

5.4 Summary

Several experiments were conducted to understand the growth of silicon nanowires using Al-Ga and Au-Ga alloy with and without the presence of plasma. The results suggest that the synthesis of silicon nanowires is possible with Al-Ga alloy at 300 °C in the tip led fashion and at 200 °C in the bulk fashion. In the case of the Au-Ga alloy, the silicon nanowires could be grown as temperatures as low as 200 °C with Ga at their tips. A general characteristic of the silicon nanowires synthesized using Al-Ga and Au-Ga alloy is their narrow nanowire diameter distribution and this is attributed to the small size droplets formed when using these alloys. When comparing the calculated activation energy for the synthesis of silicon nanowires using different catalysts we found that:

$$E_a (\text{Au-Ga}) < E_a (\text{Ga metal}) < E_a (\text{reduced Gallia}) < E_a (\text{Al-Ga})$$

$$32.4 \text{ kJ/mol} < 33.5 \text{ kJ/mol} < 35.4 \text{ kJ/mol} < 48.6 \text{ kJ/mol}$$

As it can be observed there is no remarkable difference in the activation energy values for different Ga sources and the Au-Ga alloy. In the case of the Au-Ga alloy this might be due to the rich Ga molten phase that is in the surface of the catalyst (where the reaction takes place) that makes the behavior to be more Ga likely.

However, the case of the Al-Ga alloy is quite different due to the promptly tendency of Al to form an oxide monolayer when exposed to ambient conditions, this along with the huge energetic barrier that has been calculated for pure Al for the synthesis of silicon nanowires (≈ 255.2 kJ/mol) could be leading to the observed detrimental cocatalytic effect of Al compared with Au.

CHAPTER 6

PLASMA-MOLTEN SYNERGISTIC EFFECTS

In this chapter, the interaction of plasma excited gas phase with molten gallium is studied using hydrogen adsorption measurements. Specifically, hydrogen and nitrogen plasma chemistry is studied to determine their interaction with molten gallium. The results are then analyzed to understand the potential of molten metals as catalysts for plasma-catalysis.

6.1 The absorption of hydrogen in Gallium

The hydrogen absorption experiments were performed using a modified reactor setup. The reactor setup included a pack of quartz capillary tubes for supporting high amount of Ga droplets. The reactor is tested as a batch reactor to determine the pressure changes with and without plasma excitation. The capillaries were cleaned to reduce any interaction of gases. In the case where the capillaries were clean, it was possible to observe a slight increase in the overall reactor pressure until it reached a constant value and then after shutting down the plasma, the pressure dropped. The increase in pressure observed when the plasma was turned on is due to increase in the number of moles of the gas phase with plasma excitation. For example, two moles of hydrogen radicals produced per every mole of molecular hydrogen disassociated.

The pressure change for the reactor containing packed, clean quartz tubes is shown in Figure 6.1.1 (a) by the green dotted line. The two blue dots represent the time when the plasma was turned on and off, respectively. The red line shows the experiment performed when the reactor was packed with capillaries covered with gallium. The observed pressure behavior of the reactor with the presence of Ga is remarkably different. Once the plasma was turned on, a clear reduction in the pressure was observed until it reached a constant value. When the plasma was turned off, a clear increase in the overall pressure was detected. This is for the case of hydrogen, however, similar behavior was observed for nitrogen (Figure 6.1.2).

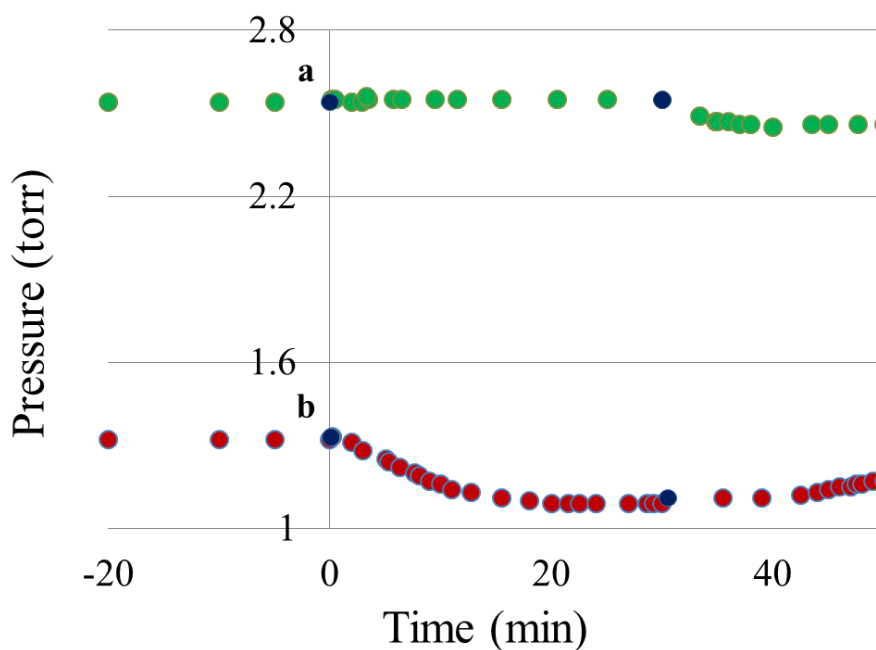


Figure 6.1.1 Pressure change in the reactor as a function of time when a) the reactor chamber was packed with clean capillaries b) the reactor chamber was packed with capillaries covered with Ga when using hydrogen at 300 °C and 70 W.

The interaction of hydrogen and nitrogen with Ga in the presence of plasma can be observed in Figure 6.1.2. Figures 6.1.2 (a) and 6.1.2 (b) at different plasma powers and Figures 6.1.2 (c) and 6.1.2 (d) show pressure behavior with nitrogen plasma at different plasma powers at constant temperature of 400 °C.

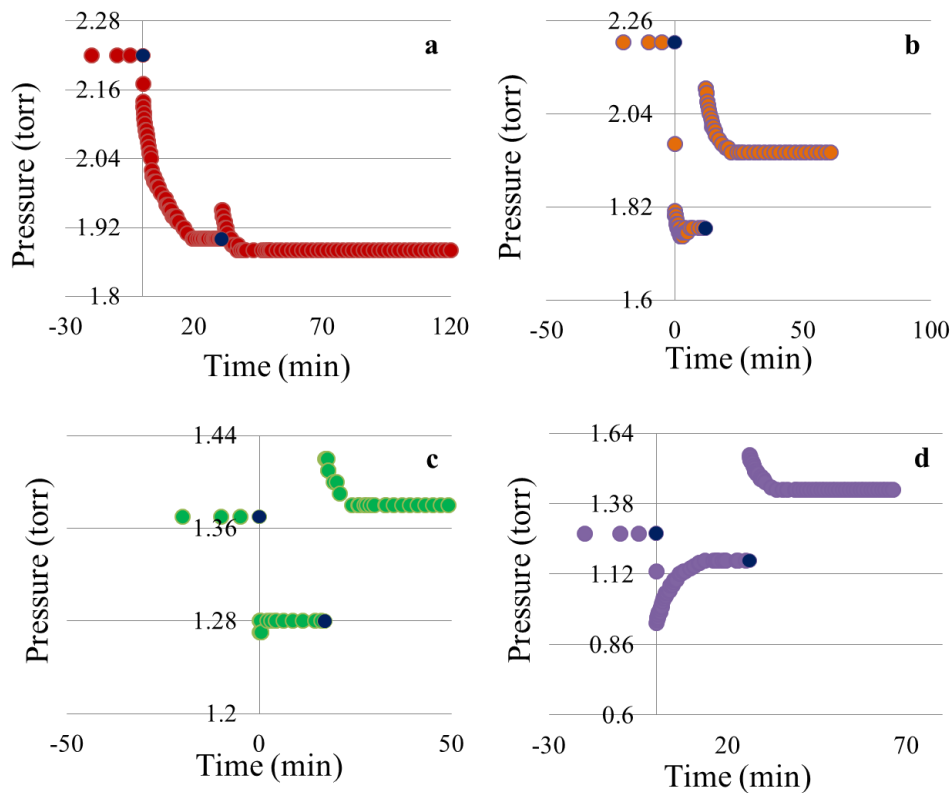


Figure 6.1.2 Pressure change as a function of time when using hydrogen and capillaries covered with Ga in the presence of plasma at a) 70 watts, b) 140 watts. Pressure change as a function of time when using nitrogen and capillaries covered with Ga in the presence of plasma at a) 70 watts, b) 140 watts.

The calculated amount of hydrogen absorbed in milimoles with different plasma powers and temperatures is shown in Figure 6.1.3. As it can be observed from the plot, for the case of 70 watts, the amount of hydrogen absorbed decreases considerably at 300 °C and keeps going down as the temperature increases from this point. This temperature then, marks the point where the hydrogen desorption becomes important. When the plasma power is doubled to 140 watts the trend is clearer and the amount of hydrogen absorbed diminish as temperature increases. This, again is attributed to the increased rate of hydrogen desorption at high temperatures. However, it is important to notice that 400° C does not follow this trend at both plasma powers. And it is possible to observe an important absorption of hydrogen in molten Ga at this condition.

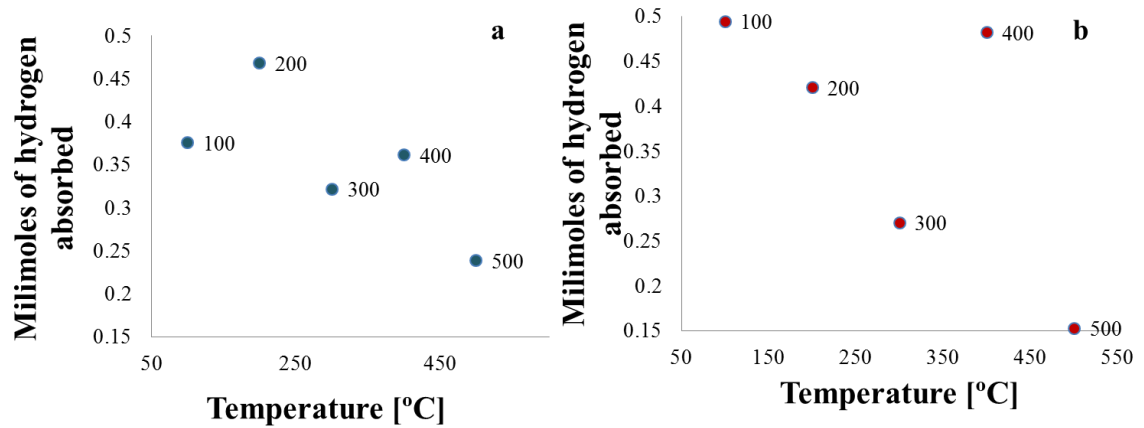


Figure 6.1.3 Milimoles of hydrogen absorbed at different temperatures when using a) 70 watts and b) 140 watts.

The same measurements were performed but when using nitrogen in the presence of plasma. Figure 6.1.4 (a) shows the measurements using 70 W and Figure 6.1.4 (b) the

measurements at 140 W. As it can be observed at high temperatures i.e. around 800 °C, the change in pressure is almost negligible meaning that the absorption of nitrogen is near zero. However, for the particular case of 800 °C and 900 °C at 70 watts and 140 watts, it is possible to observe the presence of a black layer covering the quartz tubes and a blackish change in color in the capillaries covered with Gallium.

For both cases of hydrogen and nitrogen absorption it can be observed that the lower the temperature, the higher the amount of hydrogen/nitrogen absorbed. Also as the plasma power increases, the absorbed amount of nitrogen/hydrogen decreases. The existence of this interaction at low temperatures is of great importance since it can lead to make possible the synthesis of ammonia at mild conditions.

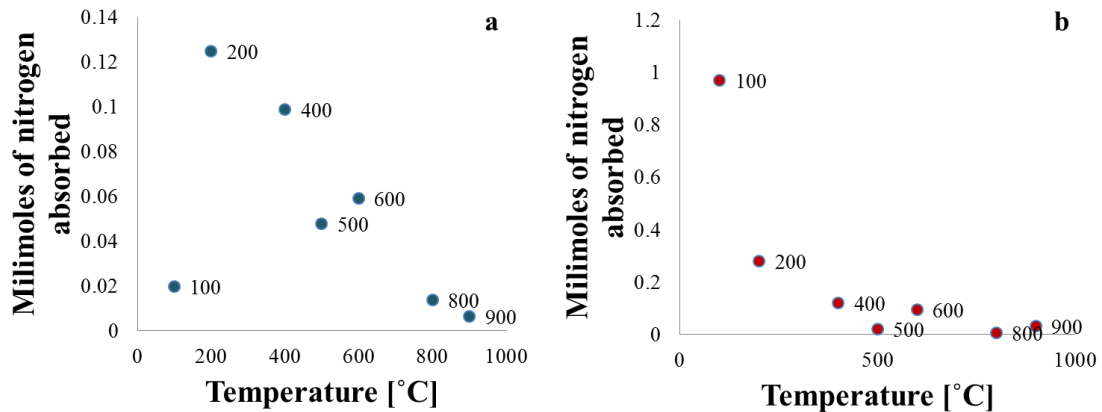


Figure 6.1.4 Milimoles of nitrogen absorbed at different temperatures when using a) 70 watts and b) 140 watts.

As it can be observed, from the calculations of the amount of hydrogen and nitrogen absorbed the number of milimoles is higher at lower temperatures. This low temperature range is where the reaction for the growth of silicon nanowires occur. The

remarkable pressure change observed at these low temperatures indicating a higher absorption of hydrogen and nitrogen species due to the interaction of hydrogen with Ga in the presence of plasma can be an indication of the successful synthesis of silicon nanowires at these temperatures.

6.2 The GaN formation at 800 °C and 70 watts

As previously mentioned, the experiments on the interaction of nitrogen with Ga in the presence of plasma at temperatures higher than 800 °C lead to the formation of a blackish layer on the tube as well as in the covered capillaries. In order to determine the resulting deposit, a quartz substrate covered with a thick Gallium layer was exposed to nitrogen plasma at 800 °C and 70 watts. The reaction was performed using the reactor in a continuous flow configuration and the pressure was set at 1.2 torr. Figure 6.2.1 shows the pictures of the reactor using nitrogen plasma and the quartz substrate covered with Gallium. From this image, it is clear to observe the formation of a black product from the interaction of nitrogen with Gallium at 800 °C and 70 watts.

XRD analysis of the resulting deposit shows the characteristic peaks for the GaN. See Figure 6.2.1 (a). Figure 6.2.1 (b) shows the SEM image of the hexagonal GaN crystals. This quick analysis helped us to determine the temperature at which the interaction of nitrogen with Gallium goes beyond a physisorption leading to the formation of GaN.

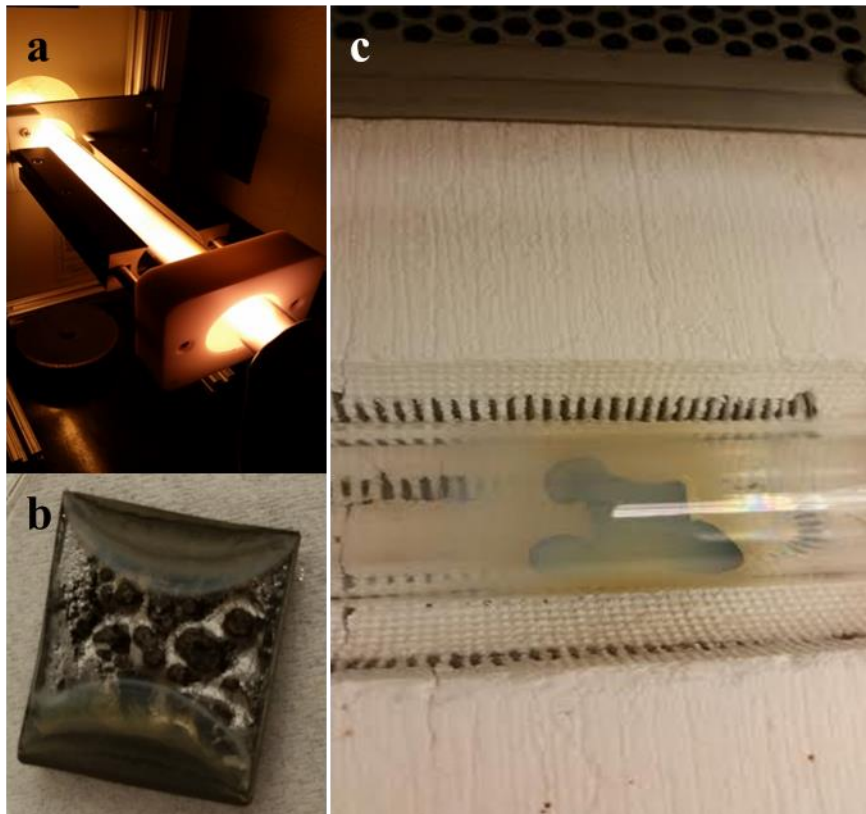


Figure 6.2.1 Pictures showing a) the reactor using nitrogen plasma, b) the quartz substrate covered with a thick Gallium film after plasma exposure and c) quartz tube after plasma exposure.

XRD analysis of the resulting deposit shows the characteristic peaks for the GaN (figure 6.2.2 9 (a)). Figure 6.2.2 (b) shows the SEM image of the hexagonal GaN crystals overlapped.

This quick analysis helped us to determine the temperature at which the interaction of nitrogen with Gallium goes beyond a physisorption leading to the formation of GaN.

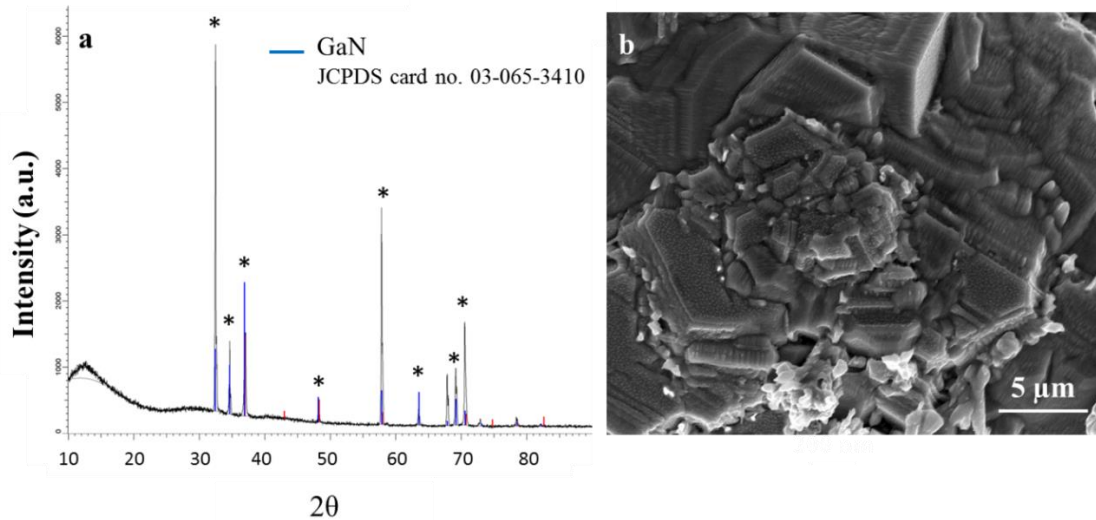


Figure 6.2.2 a) XRD diffraction pattern for the GaN film formed at 800 °C, 70 watts and 1.2 torr, b) SEM image of the formed GaN film.

6.3 First computational studies

The Vienna Ab initio Simulation Package (VASP) is used understanding the interaction of atomic hydrogen with molten gallium. VASP computes an approximate solution to the many-body Schrödinger equation, either within density functional theory (DFT), solving the Kohn-Sham equations, or within the Hartree-Fock (HF) approximation, solving the Roothaan equations. Hybrid functionals that mix the Hartree-Fock approach with density functional theory are implemented as well. In VASP, central quantities, like the one-electron orbitals, the electronic charge density, and the local potential are expressed in plane wave basis sets. The interactions between the electrons and ions are described using norm-conserving or ultrasoft pseudopotentials, or the projector-augmented-wave method. To determine the electronic groundstate, VASP

makes use of efficient iterative matrix diagonalisation techniques, like the residual minimisation method with direct inversion of the iterative subspace (RMM-DIIS) or blocked Davidson algorithms. These are coupled to highly efficient Broyden and Pulay density mixing schemes to speed up the self-consistency cycle.

The model preparation was set as follows:

- a. Initial Starting structure is Gallium bulk (orthorhombic) cut sample with 216 atoms.
- b. Annealed it very high temperature (3500K) to destroy the crystalline phase.
- c. Cooled down the sample quickly to 350K (Fast quenching).
- d. Cooled down slowly to 300K (melting temperature of Gallium is 303K).
- e. Calculate the radial distribution function to measure the nearest neighbor distance.
- f. All the simulation is done using the VASP package.

6.3.1 Computational method

The calculation of the quantum-mechanical total energy of the system and subsequent minimization of that energy with respect to the electronic and nuclear coordinates help in predicting the electronic and geometric structure of a solid. To calculate the interaction between atoms, the total energy and forces of a system, an appropriate interatomic potential is needed. Density functional theory [DFT] based ab-initio modeling is a more accurate method which originates from the fundamental view of electronic structure of the material. Due to the huge number of electrons it is impossible

to directly solve the many body hamiltonian and obtain many-particle wavefunction of solids. DFT is a many body theory which is based on the idea of using only the density as the basic variable for describing many electron systems.

The formulation of DFT based on two Hohenberg-Kohn theorems¹⁴⁶. The first Hohenberg-Kohn theorem proves that the ground state density $n(r)$ determines all properties of the system, such as external potential, the total energy, wavefunction for all states except a constant shift of energy. The second theorem indicates that there is a universal functional for total energy in term of the electron charge density, $E[n]$, which will be globally minimized by the ground state electron density. Based on these two theorems, we could write¹⁴⁷

$$E[n] = F[n] + \int d^3r V_{ext}(r)n(r)$$

$V_{ext}(r)$ is the external potential functional $F[n]$ contains all internal energies of the interacting electron gas. In 1965, according to Kohn-Sham approach¹⁴⁸, the charge density $n(r)$, kinetic energy T_s , and Hatree energy (the classical electrostatic interaction) $E_{Hartree}[n]$, of an independent particle system with single-electron wavefunction representation are expressed as

$$n(r) = 2 \sum_{i,occ} |\psi_i|^2$$

$$T_s = -\frac{\hbar^2}{2m} \sum_{i,occ} \langle \psi_i | \nabla^2 | \psi_i \rangle$$

$$E_{Hartree}[n] = \frac{1}{2} \int d^3r d^3r' \frac{n(r)n(r')}{|r-r'|}$$

Thus the Hohenberg-Kohn expression will be re-written as

$$E[n] = T_s[n] + \int d^3r V_{ext}(r)n(r) + E_{Hartree}[n] + E_{xc}[n]$$

The first three terms of this equation reflect the contribution of a non-interacting many particle system. The last term $E_{xc}[n]$ contains all non-classical interaction of the many body system. By applying the variational principle, we obtain the Kohn-Sham equation

$$H_{KS}(r)\langle\psi_i\rangle = \epsilon_i\langle\psi_i\rangle$$

With

$$H_{KS}(r) = -\frac{\hbar^2}{2m}\nabla^2 + V_{KS,eff}(r)$$

$V_{KS,eff}(r)$ is the effective potential depend on electron density $n(r)$, with the form

$$V_{KS,eff} = V_{ext}(r) + \frac{\delta E_{Hartree}}{\delta n(r)} + \frac{\delta E_{xc}}{\delta n(r)} = V_{ext}(r) + V_{Hartree}(r) + V_{xc}(r)$$

There are different approximate functionals to describe the exchange-correlation potential such as local density approximation (LDA), generalized-gradient approximations (GGAs) and Hybrid functional. If the approximate form of $V_{ex}(r)$ is determined, then the true ground state density and energy could be obtained by solving Kohn-Sham eigenvalue problem. In real calculation Kohn-Sham equation is solved self-consistently. With the initial guess of electron density, the effective potential is calculated

and the Hamiltonian is determined. After solving Kohn-Sham equation, the new electron density will be obtained from electron eigenstates. The new density will be used as input for a new iteration, until the electron density is converged.

Ab-initio Molecular Dynamics is used as a major tool in this modeling part. In MD simulation scheme, the internal force and velocity of the atoms in a system will be calculated with appropriate pseudopotential. Through Newton's second law, the coordinates of atoms at any given time will be determined. By controlling the temperature (means atomic kinetic energy), the system will be annealed or relaxed to seek suitable local energy minima, representation of the amorphous phase. The final model will be the one with a minimum total energy.

The MD simulation is first performed at temperature well above the melting temperature which forces the system to lose memory of the initial configuration and represent liquid state. Then the system is brought to a lower temperature with an appropriate quench rate. Finally the system is quenched to 0K and relaxed to an energy minimum. This method is time consuming especially for big systems and the model contain an exaggerated concentration of defects, such as wrong bonds over and under-coordinated atoms.

The simulation presented in this work are performed with the Vienna Ab-initio Simulation package (VASP) based on Density functional theory using a plane wave basis¹⁴⁹, with local density approximation and Vanderbilt's ultrasoft potential^{149, 150, 149}.

6.3.2 Model preparation and result discussion

To construct a realistic model of liquid gallium, we began with bulk [Orthorhombic crystal structure] cut 216 atoms sample. The initial configuration was melted at 3000K and equilibrated for 1000 steps. Then the system is quenched to 350K and then slowly quenched from 350K to 300K and equilibrated at 300K (figure 6.3.1).

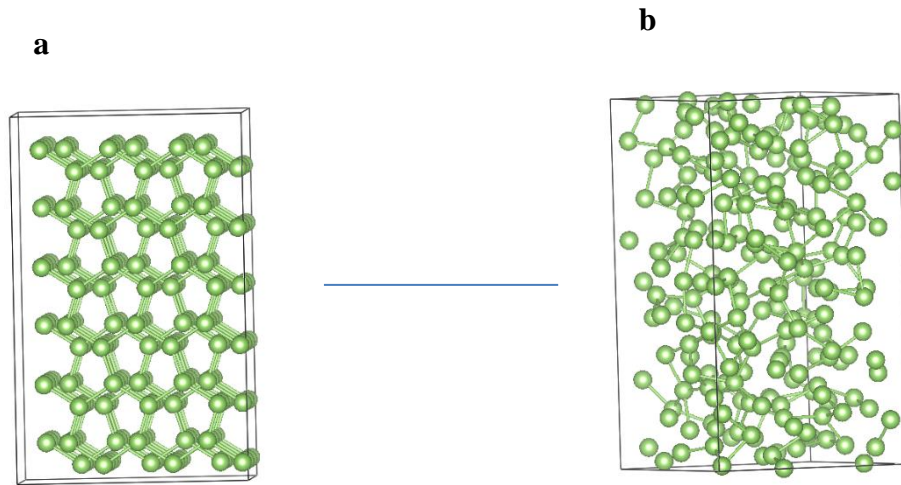


Figure 6.3.1 Simulation results for hydrogen activity in Ga using VASP at 300K and 600K.

The most popular and simple position distribution function is radial distribution function. The radial distribution function $g(r)$, gives the probability of finding a particle in the distance r from another particle.

$$g(\vec{r}) = \rho^{-2} V^{-1} N(N-1) \langle \delta(\vec{r} - \vec{r}_{ij}) \rangle$$

ρ is the density of the model, V is the volume of the model. r_{ij} is the distance between the two atoms. For amorphous material, the radial distribution function contains important

local structural information. I calculated total radial distribution functions (RDFs) of this model. The first sharp peak of the RDF (Figure 6.3.2) is the contribution from Ga-Ga correlations. The experimental partial RDF data is obtained from reference¹⁵¹ and our calculated average Ga-Ga bond length result is agree with the experimental first peak around 2.8 Å.

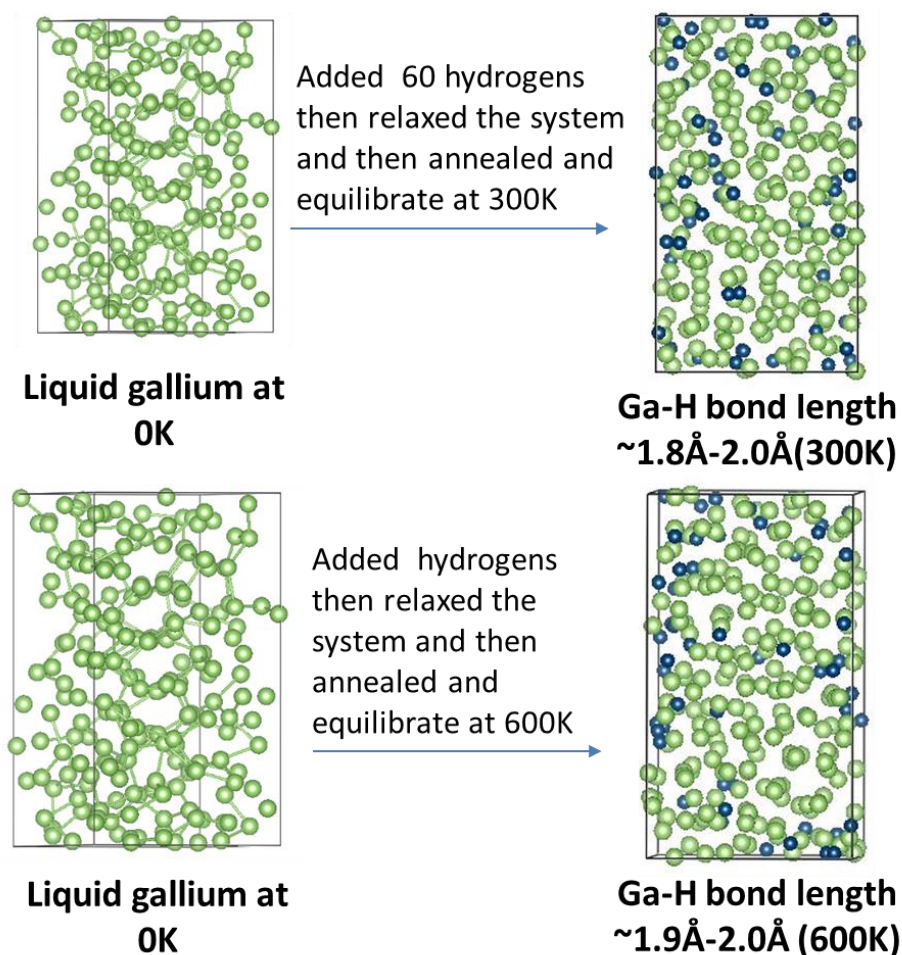


Figure 6.3.2 (a) Left side image showing liquid gallium at 0K and right side image showing hydrogenated molten gallium system at 300K (b) Left side image showing

liquid gallium at 0K; right side image showing hydrogenated molten gallium system at 600K.

To investigate the Ga and H interaction, we quenched the model again to reach the 0K and relaxed it at 0K. Added 60 hydrogens at the undercoordinated site of the model to investigate the interaction between Ga and H at 300K and 600K (Figure 6.3.2). The molten Ga -H system was annealed at 300K and 600 K and equilibrated by running another 5 picoseconds. Figure 6.3.2 illustrates that the hydrogens are distributed in the middle of the cell as well as at the surface of the cells at 300 K. Only three hydrogens are trapped inside the cell and other are moved on the surface at 600 K (Figure 6.3.2). Therefore we studied the hydrogen dynamics by calculating the mean square displacement [MSD] for this system. The mean square displacement plot (Figure 6.3.3) shows that the Ga and hydrogen atoms are less diffusive at 300K. The hydrogens inside the cells are mostly trapped in between the Ga atoms. MSD of hydrogen atoms at 600K result shows almost a linear increase with time illustrating very diffusive nature of H. Only three hydrogens trapped inside the cell and other hydrogens are moving at the surface or boundary of the model at 600K. This is in agreement with the experimental observation of a smaller amount of hydrogen absorbed on Ga at higher temperatures. As we observe through the modeling of the interaction of hydrogen with Ga, hydrogen is more diffusive at high temperatures and tends to be on the Ga surface rather than in the slab. Thus, the simulated behavior of hydrogen in Ga correlates with our experimental observations.

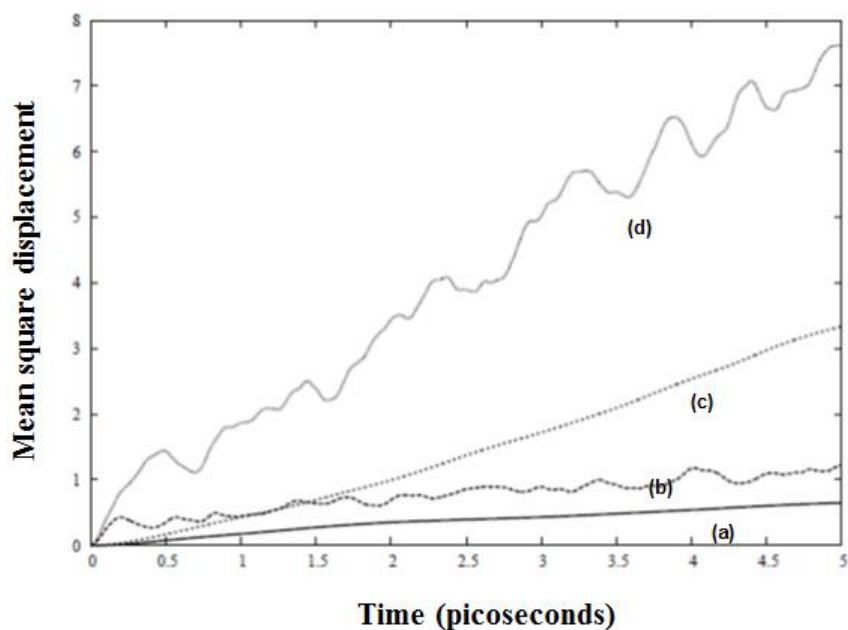


Figure 6.3.3 (a) and (b) Mean square displacement plots for gallium and hydrogen atoms at 300K. (c) and (d) Mean square displacement plots for gallium and hydrogen atoms at 600K.

6.4 The interaction of hydrogen with metals

The formation of Ga-H species has been observed as the result of the interaction of supported Ga catalysts with molecular hydrogen at high temperatures⁶⁰. Also, the formation of gallium hydrogen species on the surface of Ga₂O₃ at elevated temperatures has been reported. In the latter case, a clear understanding of the hydrogen adsorption is considered of great importance for the design of molecular sensors and alkane dehydrogenation-aromatization catalysts⁶¹. The GaH species on the Ga₂O₃ surface have

been experimentally detected by FTIR (Fourier Transform infrared spectroscopy) and its formation had been attributed to the H adatom that binds the unsaturated Ga atoms⁶².

The production of GaH species is favored at high temperatures since the oxygen vacancies creation on the Ga₂O₃ increase with temperature.

The formation of surface Ga-H on GaN (0001) has been also a topic of intensive research in order to gain a better understanding of the GaN surface structure. In this case, it has been found that molecular hydrogen does not react with the GaN (001) surface while atomic hydrogen exposure results in the formation of surface Ga-H⁶³. The changes in the electronic structure of GaN (001) had been determined by electron-energy-loss spectroscopy (EELS), Auger electron spectroscopy (AES), and low-energy electron diffraction (LEED) as indicators of the surface Ga-H presence⁶³.

However, it is important to mention that the formation of the surface Ga-H species has been reported at high temperatures. The interaction between Gallium and hydrogen occurs only when the hydrogen molecules are excited enough to interact with Gallium. The modeling of the hydrogen behavior on Ga stabilized δ -Pu at low temperatures, less than 300° C, has shown that the regions of high Ga concentration showed a dramatic decrease of the hydrogen diffusivity, and H atoms would never enter these regions⁶⁵. As discussed in Chapter 4, the formation of Ga-H species on the surface of molten gallium is an important step for selective dissolution of silicon in to molten Ga in the presence of plasma⁵⁵. Aluminum is another metal that has been previously reported to interact with molecular hydrogen at high temperatures. This interaction leads to the formation of hydrides at temperatures around ~ 1100 °C¹²⁵. The idea of the occurrence of

metal hydrides can be supported by the reports of transition metal hydrides which are well-established complexes that are key intermediates in several homogenous and heterogeneous Au catalyzed reactions¹³³. Particularly, Gold hydrides have been postulated as intermediates in numerous homogeneously catalyzed hydrogenations^{134, 135} and hydrosilylations¹³⁶. Despite the widely use of Gold as catalyst, the importance of its hydrides have attracted much attention just recently¹³⁷ due to its importance in the catalytic process. In fact, the strong interaction of Gold with hydrogen has been applied for pulling gold nanowires using a hydrogen clamp, in this clear example of interaction of hydrogen with Gold a hydrogen molecule can be incorporated in to a gold nanocontact, making a hydrogen clamp that is strong enough to pull a chain of gold atoms¹⁵².

Furthermore, in the presence of plasma it is important to consider the recombination of atomic H. Wood and Wise¹⁵³ were the first that proved that the actual density of atomic hydrogen in various plasma sources is determined by the recombination probability of atoms on the walls $\gamma(0 \leq \gamma \leq 1)$. The historical importance of this work is primarily based on the determination of the recombination coefficients of hydrogen on different metallic substrates in a simplifying way, without considering surface properties such as crystallographic structure and chemical coverage.

However, it was clearly stated that the value of γ depends on the temperature. In accordance with that, a free atom is more likely to recombine with one adsorbed on a surface. This means that a hydrogenated surface exhibits a high recombination coefficient¹⁵⁴. Therefore, we can point the recombination on the surface as well as in the bulk as potential pathways for net reduction in moles as observed in Figure 6.4.1. The

overall interaction of atomic hydrogen with molten Ga can be visualized as follows: (i) surface adsorption of hydrogen on molten Ga; (ii) diffusion of H or Ga-H in to bulk; (iii) surface recombination between gas phase atomic hydrogen and surface adsorbed species; (iv) recombination inside bulk; and (v) desorption of atomic hydrogen.

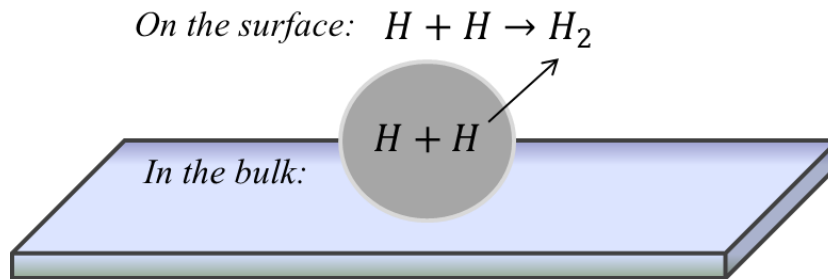


Figure 6.4.1 Schematic illustrating recombination of atomic hydrogen on the Ga surface and in the bulk as a means of reduction of the total number of moles.

The recombination of atomic hydrogen on the surface and in the bulk can lead to a reduction in the overall number of moles which can explain the observed decrease in reactor pressure with plasma. This recombination leads to the formation of molecular hydrogen. The adsorption of hydrogen both on surface and bulk can provide enough concentrations of hydrogen for promoting reactions such as selective dissolution and hydrogenation and hydrogen mediated reduction reactions with molten metals such as Ga in the presence of plasma.

6.5 Summary

The absorption/adsorption of nitrogen and hydrogen in Ga in the presence of plasma confirms high amount of hydrogen in molten Ga and its role in selective dissolution for one-dimensional growth. As the temperature increased, the net decrease in pressure reduced indicating desorption of atomic hydrogen is enhanced. This is contrary to the case when the plasma power increases, where the absorbed amount of nitrogen/hydrogen decreases. The modelling results confirm the significant interaction of atomic hydrogen with molten Ga with formation of high amounts of adsorbed hydrogen on surface, rapid diffusion through bulk and steady state concentrations of hydrogen inside bulk. As the temperatures increased, theoretical simulations predict that the diffusion of hydrogen is fast and lower steady state concentrations inside bulk Ga.

CHAPTER 7

THE CAPACITY AND DURABILITY OF SILICON NANOWIRES AND
AMORPHOUS SILICON NANOTUBE THIN FILM ANODE FOR LITHIUM ION
BATTERY APPLICATIONS

In this chapter, the silicon nanowire arrays grown using plasma-Ga catalysis approach has been investigated for their capacity as anodes for lithium ion battery applications. In addition, silicon nanotube thin films are prepared using a novel method involving plasma and Zinc Oxide nanowire film as sacrificial template. The resulting silicon nanotube thin films have also been investigated as anodes for lithium ion battery applications. In this chapter, the state of the art on silicon nanomaterials for LIBs applications is discussed. In order to understand the significance of this work, state of the work on silicon based nanostructured materials for lithium ion battery anodes is reviewed in detail here.

7.1 Lithium ion battery technology and nanostructured silicon based materials

Li ion technology have gained widespread importance as portable rechargeable batteries for a wide range of applications due to their high specific energy density (100-200 Wh/Kg), high volumetric energy density (200-400 Wh/L), small size and lighter weight batteries¹⁵⁵. A Li ion battery consists of a cathode and anode separated by an electrolyte permeable separator. The space between the electrodes is filled with a non-aqueous electrolyte. The Li ion insertion into the lattice is referred as intercalation, while

Li ion removal as deintercalation. During the charge cycle, Li ions are deintercalated from the cathode, diffuse through the electrolyte and intercalate into the anode. Electrons move in the external circuit from the cathode to the anode. During the discharge cycle, the process is reversed.

Some important terminology used in Li ion batteries:

Specific Capacity: The specific capacity is defined as the amount of charge a Li ion battery contains per unit weight of the active electrode material. It is expressed in mAh/g and depends on the current rate.

Coulombic Efficiency: The coulombic efficiency gives an indication of the current (or charge) wasted in undesirable side reactions such as electrolyte decomposition, transformation or corrosion of electrode materials of the battery. And it is given by the following equation:

$$\% \text{ Coulombic efficiency} = \frac{\text{discharge capacity}}{\text{charge capacity}} \times 100$$

C-rate: The C-rate is a way to express the charge or discharge current rate of a battery. A discharge rate of 1C indicates that the current corresponding to this discharge rate would cause the battery to be discharge in 1 hour.

Solid-Electrolyte Interface (SEI): The solid-electrolyte interface is a passivating layer formed on the electrodes due to the electrode-electrolyte reactions. This layer is ionically conducting and electronically insulating and has a negative impact on the mechanical stability of the electrodes.

Challenges with silicon nanomaterials as anodes for Li ion batteries: Silicon is a promising host for lithium due to its high theoretical specific capacity $\sim 4200 \text{ mAhg}^{-1}$ but suffers from volume expansion up to 400 % on full lithium insertion. The stress and strain associated with such large volume changes leads to the mechanical degradation of the electrode^{156, 157, 158} which further dramatically reduces the battery capacity and life time. Previous studies demonstrated that the tendency to fracture can be reduced or avoided by shrinking the materials size to the nanometer scale^{159, 160}. The improved performance of nanometer size materials is due to the smaller domain size compare to the critical size for the fracture which is estimated to be about 300 nm for Si¹⁶¹.

Using the above mentioned hypothesis, several 0-D and 1-D morphologies at nanoscale have been tried; they include nanoparticles¹⁶², nanowires^{163, 164}, Si thin films^{165, 166} and silicon/graphene^{63, 167} composites. In the case of Si thin films, the main advantage is that they are free from conductive additives and binders. Yet, the mechanical fracture⁷⁸ limits silicon thin films for use in battery applications. Silicon nanoparticles dispersed in conductive binders have been investigated as anodes¹⁶⁸. When using traditional binders very thick SEI layers grew on Si nanoparticles electrodes which results in an overall decay of the material performance¹⁶⁹. Proper modifications to the silicon nanoparticles along with appropriate designed conducting binders can increase the cycle life performance^{61, 62}. However the cost of these binders and the weight of inactive materials are potential issues for practical applications.

1-D nanostructures such as silicon nanowires have shown up to 80% theoretical capacity but only for a few cycles¹⁶⁴. Low durability with cycling has been attributed to

several processes such as: the formation of metal silicides from the substrate-silicon reactions ¹⁷⁰, ¹⁷⁰, the detachment of nanowires from the current collector due to mismatched volume changes between the substrate and the nanostructure during lithiation and delithiation ¹⁷¹ and the low yield of synthesized nanowires ¹⁷².

Silicon nanotubes are attractive nanostructures for lithium ion battery applications due to the hollowness that offers additional space for the expansion during lithiation/delithiation process preventing the mechanical pulverization of silicon. For silicon nanotubes synthesis, the use of zinc oxide nanorod arrays as templates for the development of closed capped silicon nanotube arrays as anodes has been reported. The closed tip vertical silicon nanotube arrays with diameters around 80 nm size have a direct electrical contact back to the underlying substrate. Even so, the resulting silicon tube arrays showed good performance, the synthesis requires deposition of ZnO nanorod array on the substrate. This is accomplished by the deposition of a seeding layer of Zn by metalorganic chemical vapor deposition followed by incubating in an aqueous solution. In addition, it is difficult to make thicker electrodes with the desired tap density. Another study reported the synthesis of a free-standing silicon nanotube mat using polymer nanofibers as templates prepared by electrospinning.¹¹⁴ Even so, this method can make long nanofibers in large numbers, the subsequent steps needed for the formation of the double wall SiO_x-Si requires several heating steps, making it less scalable.

Also, carbon coated silicon nanotubes synthesized by reductive decomposition of SiCl₄ on an alumina template followed by etching is another noteworthy method for the synthesis of nanotubes as anodes¹⁷³. These nanostructures showed a Coulombic

efficiency of 89% since the carbon coating stabilizes the Si-electrolyte interface and the opened nanotube morphology offers an increased surface area available for Li ions to intercalate both in the interior and exterior of the nanotubes. However, the synthesis process requires steps of huge energy needs, such as annealing at temperatures near 1000°C which prevents the possibility of making this process scalable as well.

7.2 Synthesis and electrochemical characterization of silicon nanowire arrays grown on stainless steel substrates

Silicon nanowire arrays were synthesized on stainless steel substrates using reduced Gallia particles and plasma excitation. The three main steps in this synthesis were: 1) the reduction of the Gallia nanoparticles at 700 °C for 1h using a mixture of 10% H_2 /Ar; 2) the nanowire growth reaction at 400 °C for 1h using a mixture of 2% SiH_4 / H_2 ; and 3) the removal of the Gallium tip at 800 °C for 1h using a mixture of 10% H_2 /Ar. Figure 7.2.1 shows SEM images of the synthesized nanowires before and after cycling. As seen in SEM figures, the nanowires before cycling showed no tips on the nanowires indicating that the Ga was evaporated. The average diameter for these nanowires is 300nm. The morphology of the nanowire arrays is preserved after cycling and did not undergo pulverization.

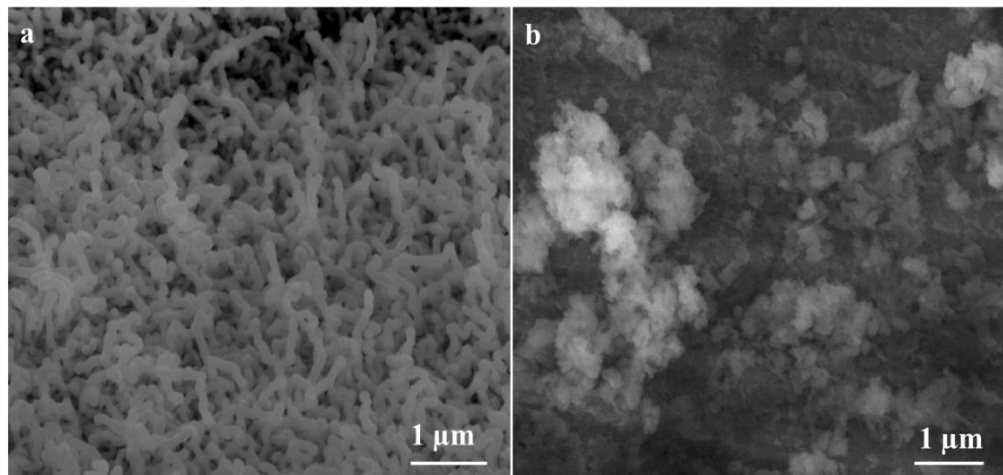


Figure 7.2.1 SEM images of silicon nanowires on stainless steel for lithium ion batteries a) before cycling and b) after cycling.

Figure 7.2.2 showed another sample with loading of 0.7 mg and the charge-discharge of Silicon tube at the voltage range of 2.2V-0.002V with a current of 100 mA/g. It has initial discharge capacity of 3243 mAh/g during the first cycle. During the second, it delivers discharge capacity of 1757 mAh/g. After 12 cycles, it still retains the discharge capacity of 1406 mAh/g. The initial discharge capacity is 3200 mAh g⁻¹, lower than the theoretical value for silicon. This might be attributed to the small oxygen content in this sample detected in the EDS analysis.

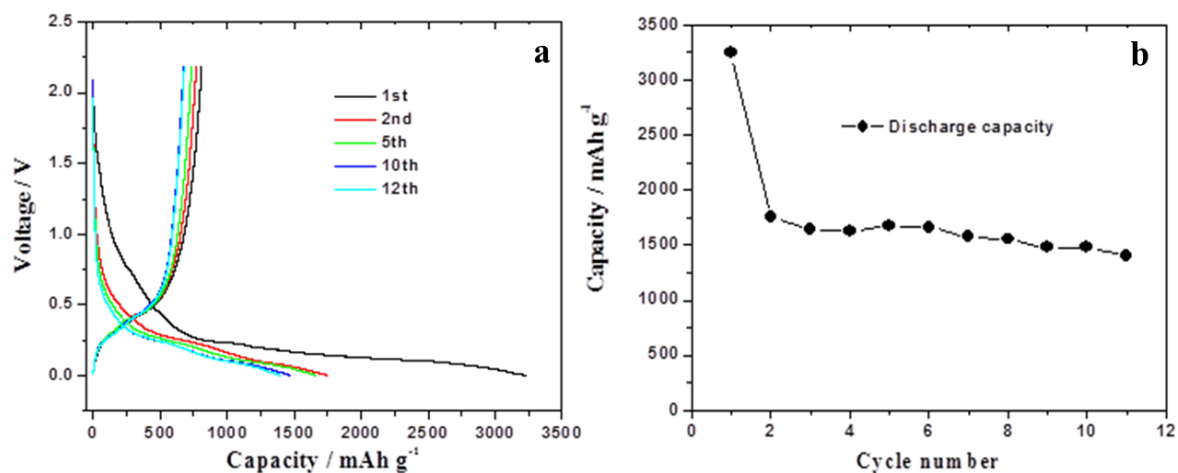


Figure 7.2.2 a) Charge-discharge curves of Silicon tube at the voltage range of 2.2 V-0.002V with a current of 100 mA/g. b) Discharge capacities versus cycle number of Silicon tube at the voltage range of 2.2 V-0.002V with a current of 100 mA/g.

7.3 Synthesis and electrochemical characterization of silicon nanotube thin films

Herein, we are proposing the use of bulk produced zinc oxide nanowire powders as cheap templates for silicon nanotube thin films synthesis. The use of this sacrificial layer combined with low temperature silicon film deposition, results in an overall cheap, fast and reproducible approach for the synthesis of nanotube thin films. Here, the ZnO nanowire powders are produced in large quantities by atmospheric plasma approach⁷⁸ and are used to make a thin film that serves as the template for producing silicon nanotubes.

Then, a silicon layer is deposited using plasma enhanced chemical vapor deposition (PECVD) on the ZnO nanowire thin film followed by the removal of the ZnO nanowires in the same reactor just by switching gases. The use of plasma allows a low temperature operation route making it suitable for producing nanotube thin films on thin metal foils. The study here investigated the cyclability of silicon nanotube thin films

produced using ZnO nanowire film as sacrificial layer without the use of any additional binders and conducting polymers. Even further, the open-ended morphology is expected to offer an increased surface area for intercalation. Another advantage of this approach is that one can increase the thickness and packing density of the nanotube films for increased loading (g/cm^2) and tap density as required. Potentially, this approach offers a scalable approach for synthesizing silicon nanotubes films with desired loading for lithium ion batteries applications.

The SEM images of the resulting silicon nanotubes from the starting ZnO nanowires are shown in Figure 7.3.1. The wall thickness of the nanotubes is approximately $\sim 30\text{nm}$ with silicon deposition for 30 minutes. The TEM images of silicon tubes obtained after in-situ removal of ZnO are shown in Figure 7.3.1(d). The resulting silicon nanotube walls are found to be polycrystalline based on transmission electron microscopy (TEM) analysis. The compositional line profile analysis revealed that the ZnO is completely absent from silicon tubes within the detection limit. The most beneficial feature of the vapor phase process seems to be the complete removal of ZnO and the absence of SiO_x layer formation inside nanotube walls. This is an important consideration as one would expect that the oxygen released during the decomposition of zinc oxide could form a silica layer. As it can be observed from Figure 7.3.1(c) for 2 hours removal duration, a portion of ZnO nanowires was present in the cores (Figure 7.3.1 (c)). The removal of ZnO nanowires was also investigated by chemical dissolution using a formic acid solution of pH 6 over several hours (typically overnight). Even though the ZnO nanowires were removed completely, the samples showed a highly

oxygen rich silicon nanotubes. These samples however, did not exhibit good performance, showing low capacities ~ 600 mAh/g and holding just a few cycles. Thus, the wet chemistry approach results in the diffusion of oxygen in to silicon nanostructures when removing the sacrificial layer. The data suggests that in-situ removal method is more efficient while avoiding the oxygen diffusion into silicon tube wall. As silicon is deposited from the vapor phase on ZnO nanowire thin film, the resulting nanotube walls are well connected (Figure 7.3.2). Further, there is no need for additional annealing step and use of any conductive binder. In addition, the adhesion of the silicon nanotube thin film on the substrate is also good due to continuity of the film.

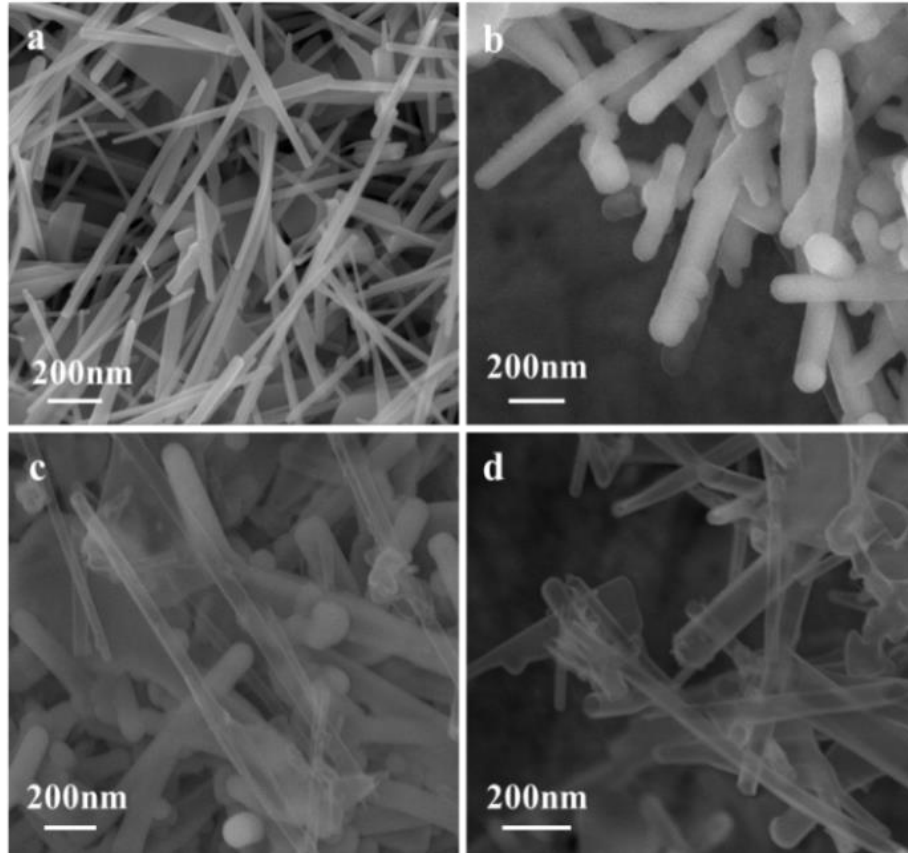


Figure 7.3.1 a) A SEM image of ZnO nanowires used as sacrificial template. b) A SEM image of ZnO nanowires covered with Si film. c) A SEM image of Si nanotubes after ZnO nanowires removal for 2 hours d) A SEM image of silicon nanotubes after removal of ZnO core using a mixture of 2% H₂ in Ar for 5 hours at 600 °C.

Figure 7.3.2 shows the SEM images of the synthesized silicon nanotubes connected to each other forming a web-like network. Figure b shows a closer view to the net showed in figure a.

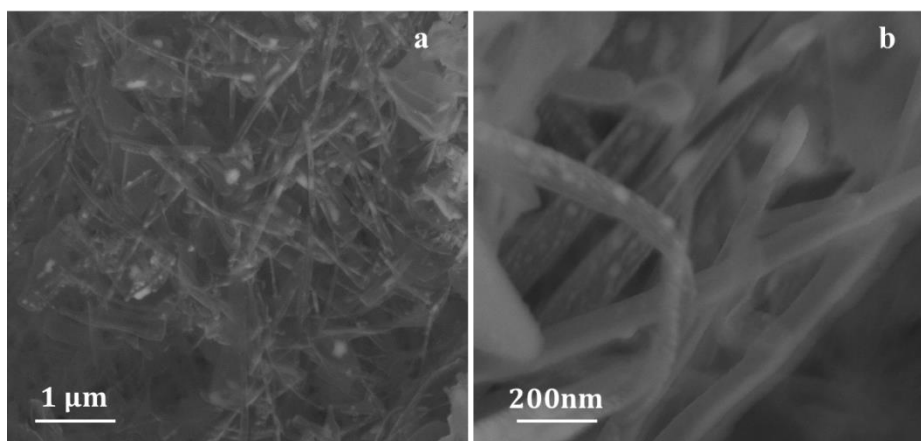


Figure 7.3.2 a) and b) SEM images of silicon nanotubes showing silicon nanotubes connected to each other.

Figure 7.3.3 shows the testing results for the 2 hours removal sample. For this sample the zinc oxide nanowires were not removed completely. Thus the performance was not as good as the 5 hours removal sample.

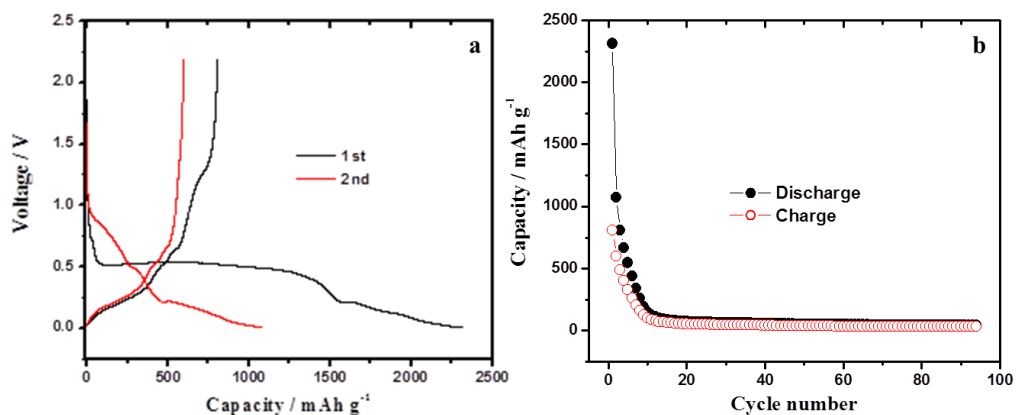


Figure 7.3.3 a) Charge-discharge curves of Silicon tube at the voltage range of 2.2-0.2 V with current density of 100 mA/g. b) Capacities vs. cycle number of silicon tube electrode at the voltage range of 2.2-0.2 V with current density of 100 mA/g for the sample of 2 hours removal.

Raman spectra for the resulting silicon nanotube film samples showed a peak centered at 510 cm^{-1} . This nc-Si:H sample showed a high first cycle capacity of $\sim 4600\text{ mAh/g}$. The observation of a first cycle capacity higher than that theoretically allowed has been reported before for other nanoscale materials systems such as tin oxide¹⁷⁴ and silicon nanowires¹⁷². Contrastingly, the Raman peak was observed around 507 cm^{-1} for the sample just covered with silicon without removing the zinc oxide nanowires (Figure 7.3.4), indicating possible oxygen diffusion during the silicon deposition in the sample. Surprisingly, the samples that do not show the characteristic Raman peak around 510 cm^{-1} peak exhibited low capacity and short life time

Figure 7.3.4 shows the Raman peaks for the sample where the zinc oxide nanowires were removed for 5 hours and the sample that was just covered with silicon without removing the zinc oxide nanowires. As it can be observed the sample that undergoes the removal of the nanowires for 5 hours exhibits a Raman peak with a value of 510 cm^{-1} , whereas the sample that still has the zinc oxide nanowires showed a value of 507 cm^{-1} indicating the possible diffusion of oxygen into the silicon film.

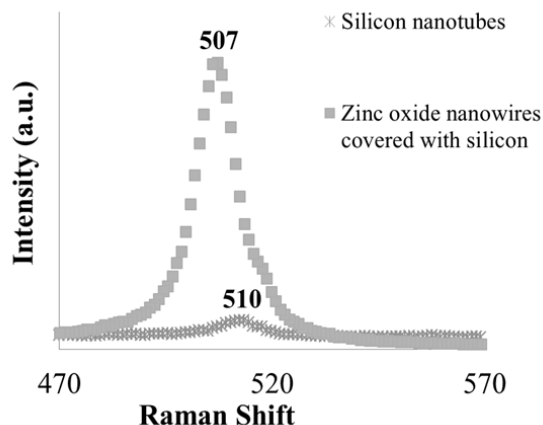


Figure 7.3.4 Raman spectra for zinc oxide nanowires covered with Si without removal step and typical Raman spectra for a sample treated 5 hours with a mixture of H_2/Ar for nanowire removal.

Silicon nanotube thin film samples without removing ZnO nanowire cores were also tested. This sample retained a capacity of 1500 mAh g^{-1} for 10 cycles. The calculated theoretical capacity for then ZnO nanowires covered with Si is around 1560 mAh g^{-1} . Thus, it is also possible to use them as high capacity anodes.

In previous reports, it was found that the room temperature dc conductivity σ of nanocrystalline Si:H (nc-Si:H) is in the range of 10^{-3} - $10^{-1} (\Omega\text{cm})^{-1}$ (higher than crystalline silicon).^{175, 169}. Since there is no binder or conductive additive used in the samples for testing, the conductive behavior of the samples is attributed to the presence of the nc-Si:H. It is important to mention that after cycling, the Raman peak shifted showing a value of 474 cm^{-1} indicating the presence of amorphous Si:H (a-Si:H)¹⁷⁶ (figure 7.3.5). The intermediate value of 510 cm^{-1} can be attributed to an intermediate, tiny

nanocrystalline component attributed to the bond dilation at the grain boundaries or either to the formation of thermodynamically stable nanocrystallites¹⁷⁷.

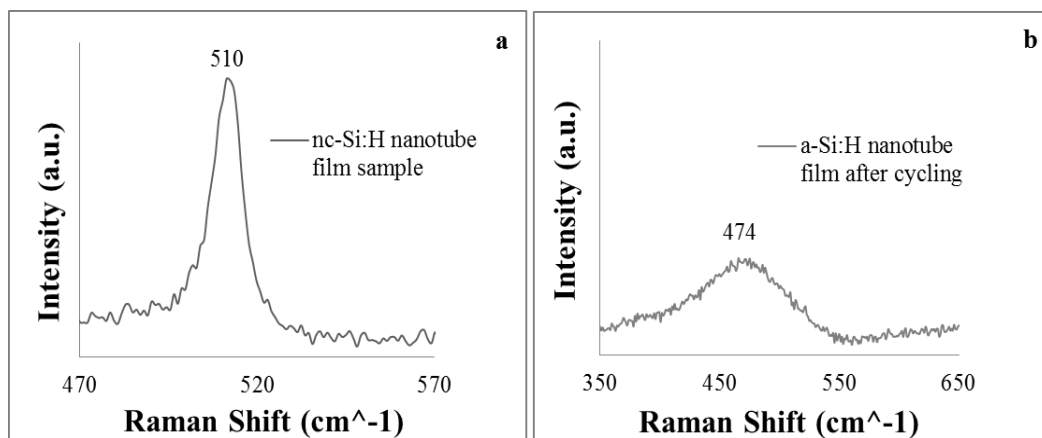


Figure 7.3.5 Raman spectra of nc-Si:H nanotubes films. a) Before cycling b) After cycling.

The lithium intercalation-de-intercalation cycling behavior is shown in Figure 7.3.6. The charge–discharge capacity curves of silicon nanotube anode electrode tested at the voltage range of 2.2-0.002 V using current of 100 mAh g⁻¹ are shown in Figure 7.3.6 (a). It has an initial discharge capacity of 4600 mAh g⁻¹ during the first initial cycle.

Higher capacity could result from higher amount of lithium incorporation at defects within silicon tube wall surfaces. Such behavior has been observed in other anode materials systems^{164, 174}. The first cycle charging (lithium alloying) has a slope at the region between 0.3-0.002 V. After the first cycle, the charge and discharge profile shows the sloping curves of lithium intercalation with Li_xSi. The average charge potential is around ~0.2 V and discharge potential of ~0.4 V, suggesting a low average potential of ~0.1 V, which means silicon nanotube anode is a good electrode with low

charge/discharge hysteresis. The discharge capacity vs. cycle number of silicon nanotube electrode was shown in Figure 7.3.6 (b). After 20 cycles, it still retains the capacity of 3600 mAh g⁻¹. The Figure 7.3.6 (c) shows the discharge capacities vs. cycle number of silicon nanotube electrode at the different current densities of 100, 500, 1000, 2000, and 4200 mA g⁻¹. It shows the first initial discharge capacities of 4600, 2700, 2200, 1800, and 1200 mAh g⁻¹ at the current densities of 100, 500, 1000, 2000, and 4200 mA/g respectively. The cyclic voltammetry of the silicon nanotube anode electrode at the voltage range of 2.2 C-0.002 V with a scan speed of 5 mV s⁻¹ is shown in Figure 7.3.6 (d). The charge current shows the formation of Li-Si alloy, which begins at the voltage of 0.15V and become large at 0.1V. During discharge, the current peak appears at 0.54V.

During the second cycle, the peak potential at 0.15 V shifted to lower voltage indicating the crystal to amorphous phase change. We observe large capacities mainly below 0.5 V from the silicon nanotube electrode from cyclic voltammetry data may be due to the Li_xSi. The cathodic peak at 0.25 could be attributed to the decomposition of Li_xSi to Si and Li_x.

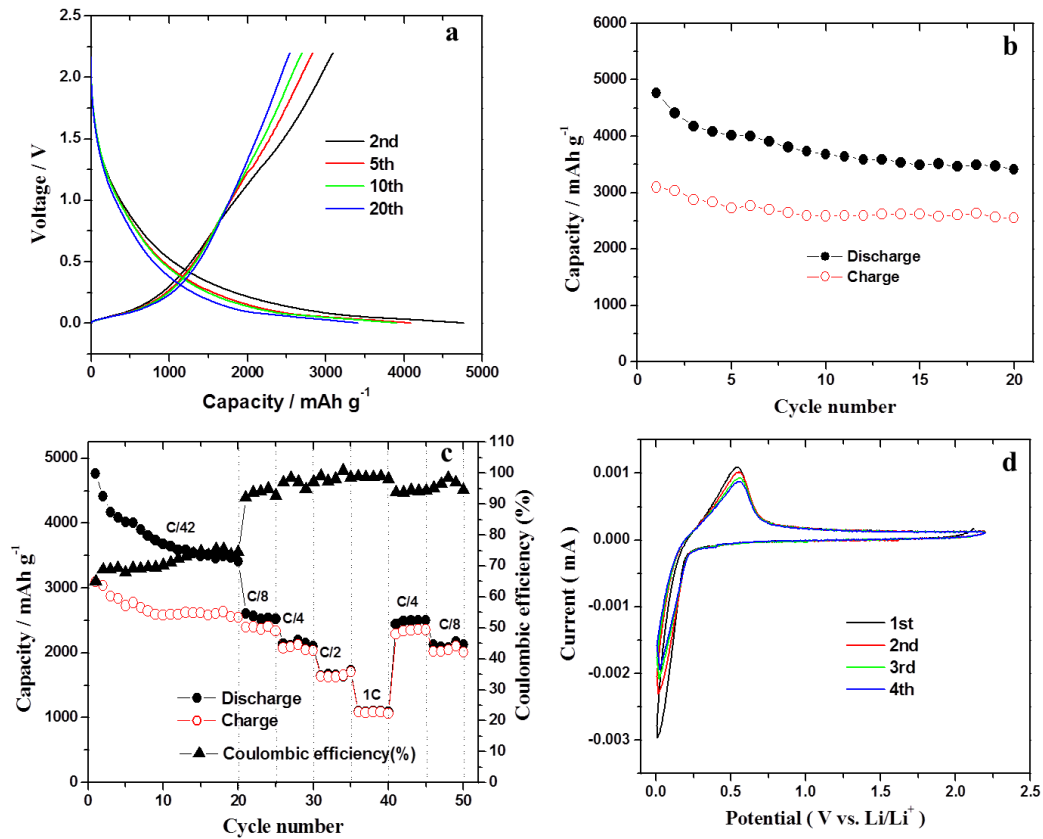


Figure 7.3.6 a) First charge-discharge curves of silicon tube at 0.024C. b) Discharge capacities vs. cycle number of silicon tube at a current of 100 mA/g c) Discharge capacities vs. cycle number of silicon tube at different rate of 500mA/g, 1000mA/g, 2000mA/g, 4200mA/g d) Cyclic voltammetry of silicon tube at the scan rate of 1mV/s.

The charge-discharge capacities versus cycle number of silicon nanotube thin film are shown in Figure 7.3.7. In this plot it is possible to observe an initial discharge capacity of 4766 mAh/g and a charge capacity of 3095 mAh/g using C/24 rate during the first cycles which corresponds to a coulombic efficiency of 65%. However, the coulombic efficiency jumped up to 97% at higher C rates > C/8. At low rates, the sample spends a much longer time in the electrolyte during alloying and de-alloying reactions.

During the first Li^+ insertion, silicon tube exhibited a high capacity of 4766 mAh/g, which is higher than the theoretical capacity of silicon >4200 mAh/g. However, the first discharge capacity is not fully released after de-insertion due to the massive irreversibility of the first lithiation step. This phenomena can be attributed mainly to the irreversible reduction of the electrolyte to form a surface passivation layer on the active particles; namely solid electrolyte interphase⁶². The large difference in charge- discharge capacities of silicon tube could also be due to the lithium storage on defects such as edges and hydrogen containing surface groups^{62, 63}.

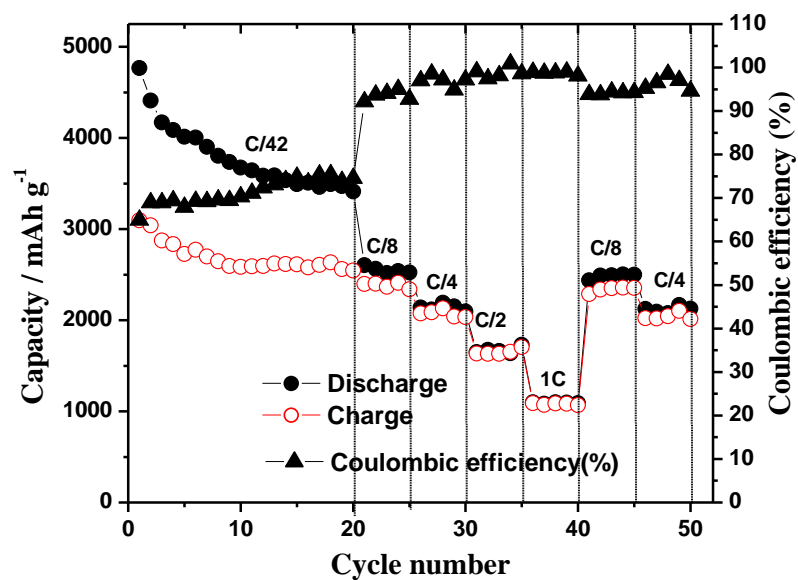


Figure 7.3.7 Coulombic efficiency as a function of cycles for silicon nanotube thin films.

Silicon nanotube thin film samples without removing ZnO nanowire cores were also tested (Figure 7.3.8). This sample retained a capacity of 1500 mAh g^{-1} for 10 cycles (S4). The calculated theoretical capacity for then ZnO nanowires covered with Si is around 1560 mAh g^{-1} . Thus, it is also possible to use them as high capacity anodes.

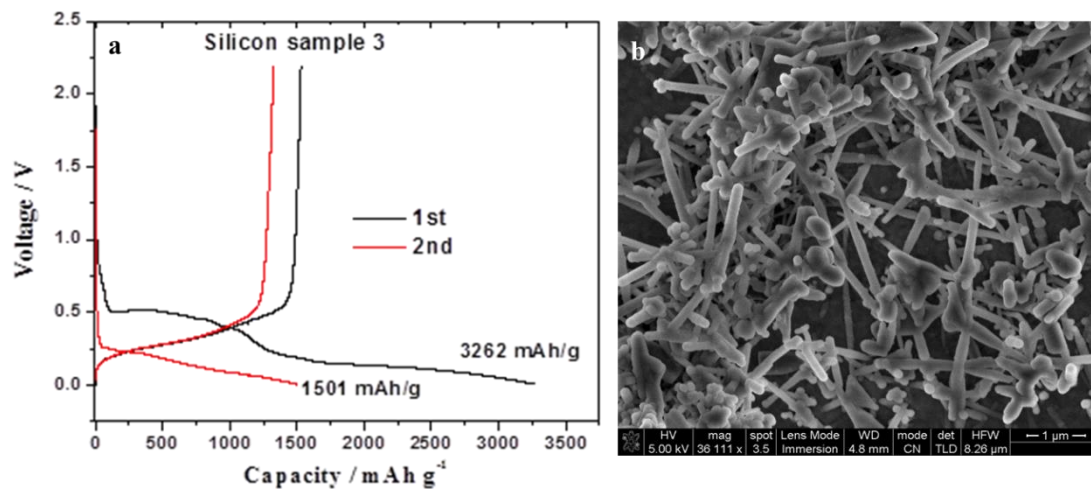


Figure 7.3.8 Zinc oxide nanowires covered with silicon a) Charge discharge curve of zinc oxide nanowires covered with silicon at voltage range of 2.2-0.002 V with current density of 100 mA/g. b) SEM image showing the Zinc oxide nanowires covered with silicon.

The silicon nanotubes preserved their morphology after cycling as shown in the TEM images in Figure 7.3.9. Also, the compositional line profile shows that the walls are rich in silicon and poor in oxygen. While the silicon content decreases corresponding to the void space characteristic of the nanotubes. However, the Raman analysis indicates that the Si transforms into an amorphous phase after the cycling. Previous reports observed this behavior after one cycle^{178, 179}. The mechanical resistance of these nanostructures can be attributed to their small size and thin wall thickness comparing to other synthesized silicon nanotubes. In this case, due to the short length of the resulting nanotubes, it is possible that the electrolyte can diffuse inside of the tubular structure.

Furthermore, the formation of a uniform thin solid electrolyte layer both inside and outside of the tubular structures can lead to an enhanced lifetime in terms of cycling.

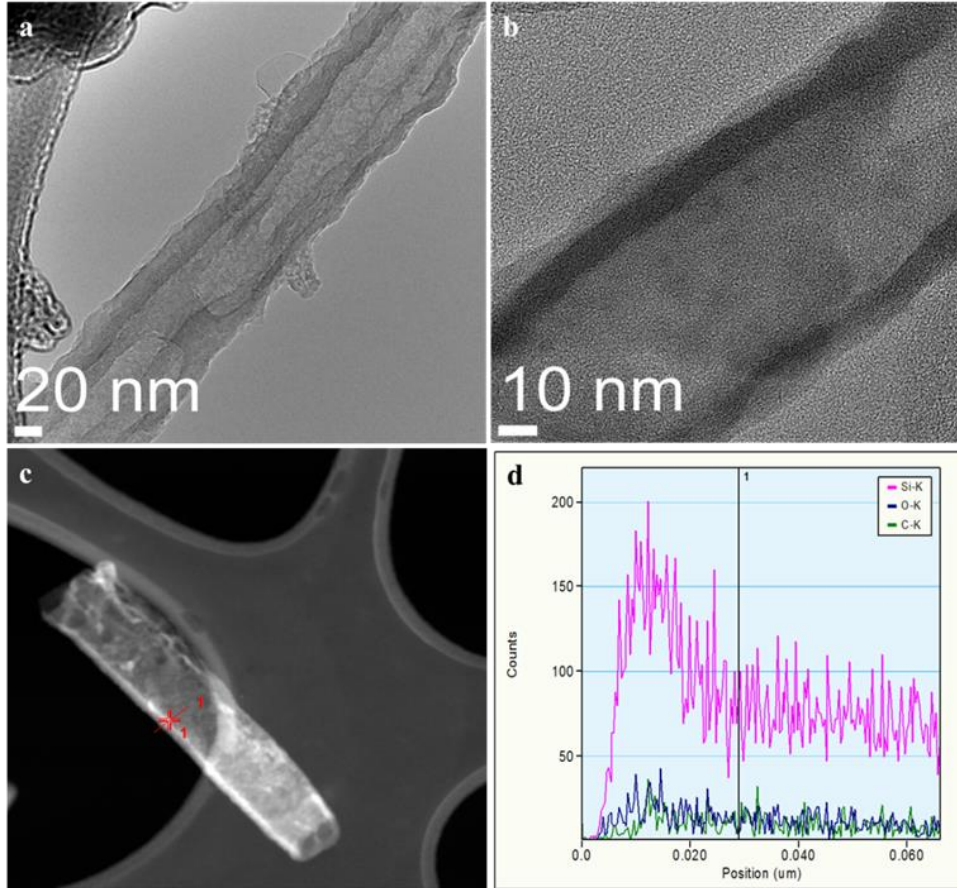


Figure 7.3.9 a) and b) TEM images of silicon nanotubes after cycling c) and d) compositional line profile analysis.

In the following the Table 7.3.1 the performance of our synthesized silicon nanotube thin films is compared with other reports on silicon nanostructures as anodes for LIBs applications. As it can be observed the performance obtained is very competitive with the existing silicon nanostructures considering also, the low temperature synthesis

required as well as the ZnO nanowires as cheap molds for the nanotube synthesis. It is important to notice that most of the silicon nanostructures that had been used as anodes in LIBs either require the use of binders, such as the case of silicon nanoparticles or coatings such as the silicon nanotubes and nanowires as observed in the first column of the table where the nanostructure is described. The use of binders and coatings help to increase the lifetime of the battery by avoiding their mechanical failure. In our case, either our nanowires or nanotubes used any of these two which results in an overall simple and cheap way to synthesize silicon anodes. Furthermore, typically the reported silicon nanowires are synthesized using gold as catalyst, which requires higher growth temperatures and costly gold removal process due to the high chemical stability of gold.

Table 7.3.1. State of the art of silicon nanostructures as anodes in LIBs.

Silicon nanostructure	Performance	Rate
Silicon nanoparticles with NaCMC as binder ¹⁸⁰	1200 mAh g ⁻¹ for 70 cycles	C/28
Silicon particles with pure poly(acrylic acid) (PAA) ¹⁸¹	2500 mAh g ⁻¹ for 100 cycles	C/20
Silicon nanoparticles with alginate as binder ¹⁸²	2000 mAh g ⁻¹ for 100 cycles	1C
Porous silicon nanoparticles ¹⁸³	2780 mAh g ⁻¹ for 100 cycles	0.2C
Coated silicon nanoparticles with microporous carbon by a simple encapsulation ¹⁸⁴	1200 mAh g ⁻¹ for 40 cycles	0.55C
Yolk-shell of carbon on silicon nanoparticles ¹⁸⁵	1100 mAh g ⁻¹ for 1000 cycles	1C
Silicon/graphene composite ¹⁸⁶	1400 mAh g ⁻¹ at 0.25 C for 200 cycles 1000 mAh g ⁻¹ at 0.5 C for 200 cycles	0.25C and 0.5C respectively
Silicon nanoparticles into mesoporous carbon ¹⁸⁷	700 mAh g ⁻¹ for 50 cycles	1C
Carbon coated silicon nanotubes ¹⁷³	3247 mAh g ⁻¹ for 200 cycles	5C
Arrays of sealed silicon nanotubes ¹⁸⁸	2924 mAh g ⁻¹ for 50 cycles	0.2C
Double-walled Si/SiO _x nanotubes ¹⁸⁹	600 mAh g ⁻¹ for 6000 cycles	12C
Si NWs obtained via a plasma-enhanced chemical vapor deposition (PE-CVD) ¹⁷¹	600 mAh g ⁻¹ for 70 cycles	2C
Carbon-Silicon Core-Shell Nanowires ¹⁹⁰	2000 mAh g ⁻¹ for 50 cycles	C/5
Our silicon nanotube thin films ¹⁹¹	2000 mAhg-1 for 50 cycles	C/8

7.4 Summary

Silicon nanotube thin films (~20 micron) without any conducting binders were synthesized directly on stainless steel substrate and were investigated as anodes for lithium ion batteries. Our results suggest that the silicon nanotube thin film retained its morphology with cycling, suggesting they were able to compensate mechanical stresses through volumetric expansions in the radial direction. The use of ZnO nanowire thin films as templates on metal substrates allowed the synthesis of high load silicon nanotubular structures (1 – 1.5 mg/cm²). Even without using conducting binders, these electrodes showed good performance (3600 mAh g⁻¹ at 100 mA/g for 20 cycles and 1200 mAh/g at 1C and 2000 mAh/g at C/8 after 50 cycles). Our data suggests that the performance depends upon the nature of the silicon nanotube wall, i.e., nc-Si:H phase versus the presence of oxygen. The silicon nanotubes using wet chemical dissolution of ZnO nanowire cores contained significant amounts of oxygen and did not perform well with electrochemical cycling.

Regarding the application of silicon nanowires to lithium ion batteries it is possible to settle that the low yield $\approx 0.7\text{mg/h}$ limits their practical applications as anodes for LIBs. However we were able to synthesize silicon nanowires smaller than 300nm in diameter which is Critical fracture size of Si. Despite this as a preliminary conclusion it is possible to attribute the nanowires lost of mechanical integrity due to the mismatched volume changes between the material and the metal substrate. However this should be further studied.

CHAPTER 8

CONCLUSIONS

In this work, plasma-molten metal synergistic effects were investigated for the synthesis of silicon nanowires at low temperatures. The conclusions for this dissertation are detailed below.

Gallium cannot catalyze the silicon nanowire growth without the use of plasma excitation even at high temperatures. With the help of gentle plasma excitation, the Ga droplets can catalyze the growth of silicon nanowires at temperatures as low as 200 °C. Ga droplets with diameters larger than 200 nm resulted in nanowires with sizes smaller than droplet diameter due to non-wetting of Ga droplets on substrates. The growth kinetics was found to be limited by dissolution kinetics under the pressures of less than 0.5 torr. A model is proposed to explain the plasma-Ga synergistic effect which involves the formation of Ga-H as intermediate for the dehydrogenation of silyl species from the gas phase. The model implies that the atomic hydrogen interacts with molten Ga and forms Ga-H species both on the surface and in the bulk. The size of Ga droplets and resulting silicon nanowires could be controlled using reduced Gallia nanoparticles.

The alloys of Gallium with aluminum and gold also catalyze the growth of silicon nanowires at low temperatures but only under the presence of gentle plasma. The estimated activation energy barrier values from growth kinetics data indicate that there is no remarkable difference in the activation energy for pure Ga and Ga-Au alloy. This is

attributed to the formation of a Ga rich shell on the Au-Ga alloy droplet surface that makes the behavior to be more Ga likely. In the case of the Al-Ga alloy, the estimated activation barrier (~48.6 kJ/mol) is more than that obtained for pure Ga or Ga-Au alloys (~34 kJ/mol). No definite conclusion can be drawn to explain the difference but the ease of oxidation of aluminum is suspected to cause higher activation barrier.

The interaction of hydrogen with Ga in the presence of plasma was confirmed by monitoring pressure changes. First principles modeling confirmed the significant interaction of atomic hydrogen with molten Ga with formation of high amounts of adsorbed hydrogen on surface, rapid diffusion through bulk and steady state concentrations of hydrogen inside bulk. Theoretical results are consistent with experimental observations on the hydrogen interactions with molten Ga under the presence of plasma.

The synthesis of silicon nanotubes using plasma for lithium ion batteries is demonstrated. The silicon nanotube thin film electrode exhibited an initial discharge capacity near the theoretical value for silicon. These nanotubes accommodated large volume changes with lithiation and exhibit stable capacity retention. The presence of hydrogenated nanocrystalline silicon (nc-Si:H) is shown to be essential for the silicon nanotube thin film performance for lithium ion battery applications. This procedure results in an overall cheap a reproducible process that can lead to a potential scalability.

In summary, the work described in this dissertation resulted in the development of a low temperature growth process that combines the use of plasma and a low melting metal. Furthermore, the studies yielded insight into plasma-molten metal synergistic

effect which could be exploited for other vapor-liquid-solid growth methods and also for reactions of great importance.

CHAPTER 9

RECOMMENDATIONS FOR FUTURE WORK

The studies presented in this dissertation suggest some potential directions for future work. Specifically, the studies presented with interaction of hydrogen and nitrogen with molten Ga in the presence of plasma excitation suggest potential way for synthesis of ammonia at mild conditions. Similarly, such interaction of hydrogen and nitrogen with molten Ga in the presence of plasma could lead to other interesting applications in the plasma catalysis field.

9.1 Plasma catalysis synthesis of ammonia

Recently, the use of plasma catalysis has emerged as a promising alternative for the synthesis of ammonia at milder conditions. The non-equilibrium plasma approach allows the generation of NH radicals when using a N_2/H_2 mixture making possible to obtain ammonia. Besides, it has been observed to enhance the ammonia yield when the metal catalyst is placed in the plasma region indicating a synergism between the catalyst and the plasma^{19, 192}.

This synergism has been confirmed by the measurement of the species formed, both in the plasma flame and the catalyst surface when using an ECR plasma. By changing the nature of the catalytic surface it was possible to register a change in the species present. Once the activated species of diatomic nitrogen and the NHx species

undergo surface adsorption on the catalyst they lead to ammonia desorption by reacting with hydrogen¹⁹³. When using plasma and iron wires combined it has been observed that the ammonia production is doubled in a period of 3h at 5torr and 620 ± 50 K. It has been concluded that the use of plasma catalysis results in two orders of magnitude higher yields than the process without the discharge¹⁹⁴.

It can be observed from the previous mentioned reports, that in plasma catalysis it is not the dissociative adsorption of nitrogen the rate limiting step for ammonia production as it is for traditional catalysis. This is mainly because, in the absence of plasma the normal N₂ triple bond is hard to dissociate into atoms even using a catalyst. Furthermore, at high temperatures it has a low sticking probability leading to the dissociative adsorption of N₂ as the rate limiting step.

In the case of plasma catalysis the excitation of N₂ changes completely the situation. The excited N₂* molecule is highly reactive due to its bi-radical nature. It can stick without fail to the surface and it is likely to dissociate into adatoms N (atomic). In this case it is the nitride formation that imposes a major limitation¹⁹⁵. In this case the coexistence of hydrogen is necessary to successfully lead to the synthesis of ammonia. The adsorbed H (atomic) or the hydrogen from the gas phase will combine with N (atomic) to yield NH and NH₂, then the valence of the nitrogen is filled and NH₃ is desorbed from the surface. The whole process can be summarized as follows:

N₂ → N₂* excitation

$N_2^* \rightarrow 2N$ (atomic) dissociative adsorption

N (atomic) + $3H/H$ (atomic) $\rightarrow NH_3$ surface reaction over catalyst

When using Ga and hydrogen/nitrogen in the presence of plasma it is possible to observe the adsorption of these gases in the molten metal. As shown in Figure 9.1.1, both gases can be adsorbed on the surface of Ga when it is exposed to plasma. The set up for these experiments consists in a batch reactor with a pressure sensor. Once the temperature and the pressure of the system is stabilized and the chamber is loaded with capillaries covered with Ga the plasma power is turned on. The dramatic pressure drop when the plasma is on can be explained by the adsorption of the gas species in to the molten metal. Once the pressure is stable again, the increase in pressure when the plasma is turned off indicates the desorption of the gases proving in this way the synergism between molten metals and plasma.

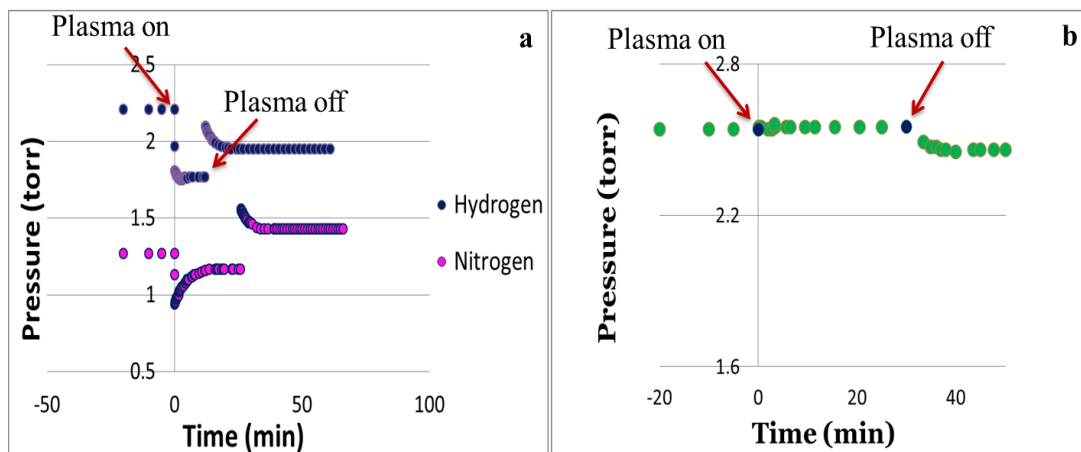


Figure 9.1.1 a) Adsorption of hydrogen and nitrogen in gallium at 400 °C and 140 W, b) Plot when there is no gallium in the reactor chamber.

As it has been pointed out is the hydrogenation of N (atomic) species that is the rate limiting step¹⁹⁶ for the case of plasma catalysis, then by having high concentrations of hydrogen on the catalyst surface it is possible to facilitate this step and lead to high yields. Our previous work has shown that Ga in the presence of plasma can act as a hydrogen sink^{55, 49}

It is expected that under the presence of plasma the excited N_2^* molecules can stick in to the molten metal surface and very likely to break further in to N (atomic). Due the high concentration of atomic hydrogen and nitrogen inside this volume it is possible to achieve high ammonia conversion efficiencies (Figure 9.1.2).

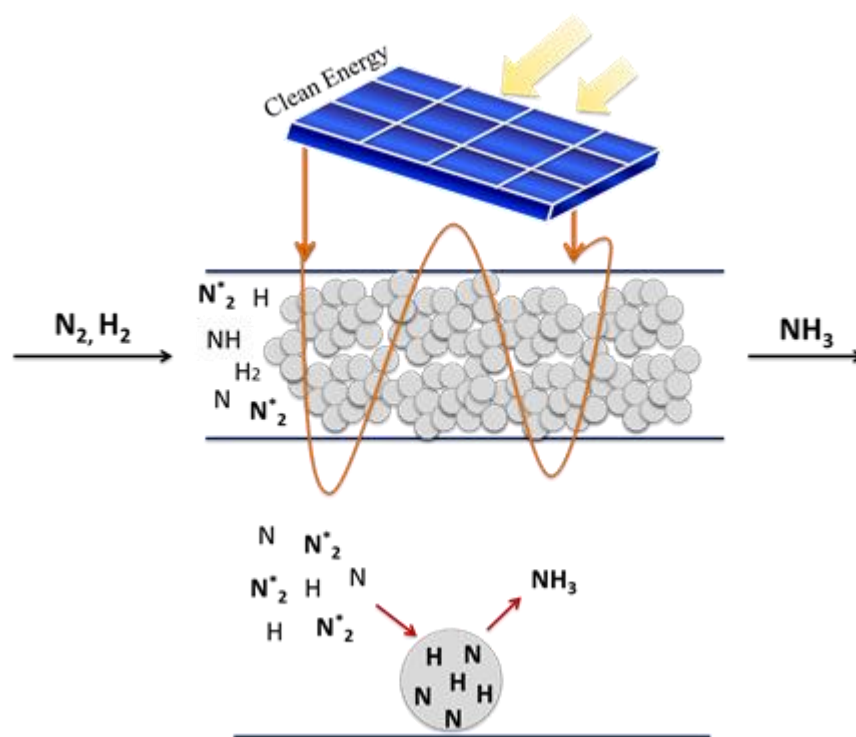


Figure 9.1.2 Schematic of the proposed set up for ammonia reaction using plasma catalysis.

The use of molten metal alloys using Ga such as Ni₅Ga₃ has been demonstrated to be particularly active and selective for CO₂ reduction to methanol at low pressures. The reaction mechanism in this case consists in a series of hydrogenation reactions that can be favored when having this molten alloy comparing with traditional precious metal catalysts¹⁹⁷. Furthermore, the Ga rich sites have shown to favor the methanol formation.

9.2 Synthesis of GaN crystals at low temperature and sub atmospheric pressure

The bulk growth of GaN requires high temperatures (typically 1200 °C) and pressures (7.5×10^5 torr) which limits this approach. The growth of GaN crystals have been demonstrated to happen at low temperature ~ 800 °C and 1.2 torr. Since this low pressure, metastable crystal growth process relies in two main phenomena: the nitrogen dissolution and crystallization out of Ga melts. It is expected that the presence of plasma helps to the dissolution of nitrogen which leads to the nucleation and growth of GaN crystals. It has been proposed that active nitrogen is generated by a plasma comprising N, N⁺, N₂^{*} and the remainder N₂⁶⁶.

Further experiments to understand the growth mechanism of these crystals can be done.

REFERENCES

1. S. Hofmann, C. D., R.J. Neill, S. Pisanec and A.C. Ferrari, Gold catalyzed growth of silicon nanowires by plasma enhanced chemical vapor deposition. *J. Applied Physics* **2003**, *94* (9).
2. Ostrikov Kostya, S. D. H., Mehdipour Hamid, Cheng Qijin, Kumar Shailesh, Plasma effects in semiconducting nanowire growth *Nanoscale* **2012**, *4* (5), 1497-1508.
3. Wu Y, C. Y., Huynh L, Barrelet C J, Bell D C and Lieber C M, Controlled Growth and Structures of Molecular-Scale Silicon Nanowires. *Nanoletters* **2004**, *4* (3), 433-436.
4. Cui Y, L. L. J., Gudixen M S, Wang J and Lieber C M Diameter-controlled synthesis of single-crystal silicon nanowires *Appl. Phys. Lett.* **2004**, *78* (2214).
5. Volker Schmidt, S. S., and Ulrich Gosele, Diameter-Dependent Growth Direction of Epitaxial Silicon Nanowires. *Nanoletters* **2005**, *5* (5), 931-935.
6. Ross, F.; Tersoff, J.; Reuter, M., Sawtooth faceting in silicon nanowires. *Physical review letters* **2005**, *95* (14), 146104.
7. Sunkara, M. K.; Sharma, S.; Miranda, R.; Lian, G.; Dickey, E., Bulk synthesis of silicon nanowires using a low-temperature vapor–liquid–solid method. *Applied Physics Letters* **2001**, *79* (10), 1546-1548.
8. Jeon, M.; Kamisako, K., Aspect of aluminum-catalyzed silicon nanowires synthesized at low temperature and effect of hydrogen radical treatment. *Journal of Alloys and Compounds* **2009**, *476* (1), 84-88.
9. Chandrasekaran, H.; Sumanasekara, G. U.; Sunkara, M. K., Rationalization of nanowire synthesis using low-melting point metals. *The Journal of Physical Chemistry B* **2006**, *110* (37), 18351-18357.
10. Sharma, S.; Sunkara, M., Direct synthesis of single-crystalline silicon nanowires using molten gallium and silane plasma. *Nanotechnology* **2004**, *15* (1), 130.
11. Sunkara, G. B. a. M. K., *J. Phys. Chem. B* **2005**, *109* (16219).
12. S. Vaddiraju, M. K. S., A.H. Chin, C.Z. Ning, G.R. Dholakia and M.Meyyappan, *J. Phys. Chem. C* **2007**, *111* (7339).
13. H.Li, A. H. C., and M. K. Sunkara, *Adv. Mater.* **2006**, *18* (216).
14. M.G. Sobacchi, A. V. S., A.A. Fridman, L.A. Kennedy, S. Ahmed, T. Krause, Experimental assessment of a combined plasma/catalytic system for hydrogen production via partial oxidation of hydrocarbon fuels. *Int. J. Hydrogen Energy* **2002**, *27* (635).
15. Y. Iwasaki, J. L., J. Zhang, T. Kitajima, M. Sakurai, H. Kameyama,, *J. Chem. Eng. Jpn.* **2006**, *39* (216).
16. T. Nozaki, T. H., K. Okazaki, *Energy Fuel* **2006**, *20* (339).
17. Spencer, L. F.; Gallimore, A. D., Efficiency of CO₂ dissociation in a radio-frequency discharge. *Plasma Chemistry and Plasma Processing* **2011**, *31* (1), 79-89.

18. Jun, K.; Jacobson, J. M. In *Effective Carbon Dioxide Reduction into Carbon Monoxide Using Millichannel Embedded in-Line Dielectric Barrier Discharge Reactor*, 14th International Conference on Miniaturized Systems for Chemistry and Life Sciences, 2010; pp 321-323.
19. Hessel, V.; Anastasopoulou, A.; Wang, Q.; Kolb, G.; Lang, J., Energy, catalyst and reactor considerations for (near)-industrial plasma processing and learning for nitrogen-fixation reactions. *Catalysis Today* **2013**, *211*, 9-28.
20. Wagner, R.; Ellis, W., Vapor-liquid-solid mechanism of single crystal growth. *Applied Physics Letters* **1964**, *4* (5), 89-90.
21. Y. Cui, L. J. L., M.S. Gudiksen, J. Wang, and C. M. Lieber, Diameter-Controlled Synthesis of Single Crystal Silicon Nanowires. *Appl. Phys. Lett* **2001**, *78*, 2214-2216.
22. Westwater, J.; Gosain, D.; Tomiya, S.; Usui, S.; Ruda, H., Growth of silicon nanowires via gold/silane vapor-liquid-solid reaction. *Journal of Vacuum Science & Technology B* **1997**, *15* (3), 554-557.
23. Purushothaman, V.; Jeganathan, K., Investigations on the role of Ni-catalyst for the VLS growth of quasi-aligned GaN nanowires by chemical vapor deposition. *Journal of nanoparticle research* **2013**, *15* (7), 1-12.
24. Zhou, G.; Yang, J. C.; Xu, F.; Barnard, J. A.; Zhang, Z. In *Quantitative VLS Growth Model and Experiments of Fe Catalyzed Si Nanowire Formation*, MRS Proceedings, Cambridge Univ Press: 2002; p F6. 3.
25. Arbiol, J.; Kalache, B.; Cabarrocas, P. R.; Morante, J. R.; Morral, A. F., Influence of Cu as a catalyst on the properties of silicon nanowires synthesized by the vapour-solid-solid mechanism. *Nanotechnology* **2007**, *18* (30), 305606.
26. Joerg V. Wittemann, W. M., Stephan Senz, and Volker Schmidt, Silver catalyzed ultrathin silicon nanowires grown by low-temperature chemical-vapor-deposition. *Journal of Applied Physics* **2010**, *107* (096105).
27. Chen, C.-C.; Yeh, C.-C.; Chen, C.-H.; Yu, M.-Y.; Liu, H.-L.; Wu, J.-J.; Chen, K.-H.; Chen, L.-C.; Peng, J.-Y.; Chen, Y.-F., Catalytic growth and characterization of gallium nitride nanowires. *Journal of the American Chemical Society* **2001**, *123* (12), 2791-2798.
28. Hofmann, S.; Ducati, C.; Neill, R.; Piscanec, S.; Ferrari, A.; Geng, J.; Dunin-Borkowski, R.; Robertson, J., Gold catalyzed growth of silicon nanowires by plasma enhanced chemical vapor deposition. *Journal of Applied Physics* **2003**, *94* (9), 6005-6012.
29. Sharma, S.; Li, H.; Chandrasekaran, H.; Mani, R.; Sunkara, M., Synthesis of inorganic nanowires and nanotubes. *Encyclopedia of Nanoscience and Nanotechnology*, ed. H. Nalwa, American Scientific Publishers, Los Angeles, CA **2004**, 327.
30. Meyyappan, M.; Sunkara, M. K., *Inorganic nanowires: applications, properties, and characterization*. CRC Press: 2009.
31. Buffat, P.; Borel, J. P., Size effect on the melting temperature of gold particles. *Physical Review A* **1976**, *13* (6), 2287.
32. Wong, Y.; Yahaya, M.; Mat Salleh, M.; Yeop Majlis, B., Controlled growth of silicon nanowires synthesized via solid-liquid-solid mechanism. *Science and Technology of Advanced Materials* **2005**, *6* (3), 330-334.

33. Ma, Z.; McDowell, D.; Panaitescu, E.; Davydov, A. V.; Upmanyu, M.; Menon, L., Vapor–liquid–solid growth of serrated GaN nanowires: shape selection driven by kinetic frustration. *Journal of Materials Chemistry C* **2013**, *1* (44), 7294-7302.
34. Elliott, R. P.; Shunk, F. A., The Au– Ga (Gold-Gallium) system. *Bulletin of Alloy Phase Diagrams* **1981**, *2* (3), 356-358.
35. Hou, W.-C.; Chen, L.-Y.; Hong, F. C.-N., Fabrication of gallium nitride nanowires by nitrogen plasma. *Diamond and Related Materials* **2008**, *17* (7), 1780-1784.
36. Wang, B.; Zheng, K.; Shao, R.; Wang, Y.; Wang, R.; Yan, Y., Structure and electrical property of gallium nitride nanowires synthesized in plasma-enhanced hot filament chemical vapor deposition system. *Journal of Physics and Chemistry of Solids* **2013**, *74* (6), 862-866.
37. Hou, W. C.; Hong, F. C.-N., Controlled surface diffusion in plasma-enhanced chemical vapor deposition of GaN nanowires. *Nanotechnology* **2009**, *20* (5), 055606.
38. Tang, W.-C.; Hong, F. C.-N., Growths of indium gallium nitride nanowires by plasma-assisted chemical vapor deposition. *Thin Solid Films* **2014**.
39. Murray, J.; Massalski, T., Binary alloy phase diagrams. *American Society for Metals, Metals Park, OH* **1986**, 173.
40. Zheng, J.; Song, X.; Li, X.; Pu, Y., Large-scale production of amorphous silicon oxynitride nanowires by nickel-catalyzed transformation of silicon wafers in NH₃ plasma. *The Journal of Physical Chemistry C* **2008**, *112* (1), 27-34.
41. Lari, L.; Murray, R.; Bullough, T.; Chalker, P.; Gass, M.; Cheze, C.; Geelhaar, L.; Riechert, H., Nanoscale compositional analysis of Ni-based seed crystallites associated with GaN nanowire growth. *Physica E: Low-dimensional Systems and Nanostructures* **2008**, *40* (7), 2457-2461.
42. Wang, Z. L.; Liu, Y.; Zhang, Z., *Handbook of Nanophase and Nanostructured Materials: Synthesis/Characterization/Materials Systems and Applications I/Materials Systems and Applications II*. Springer: 2003; Vol. 3.
43. Wang, Q.; Lu, X.; Zhang, L.; Hang, L.; Zhang, W.; Wang, Y.; Lun, S. In *Amorphous silicon-assisted self-catalytic growth of FeSi nanowires in arc plasma*, Vehicular Electronics and Safety (ICVES), 2013 IEEE International Conference on, IEEE: 2013; pp 258-262.
44. Mehdipour, H.; Ostrikov, K.; Rider, A.; Furman, S., Minimizing the Gibbs–Thomson effect in the low-temperature plasma synthesis of thin Si nanowires. *Nanotechnology* **2011**, *22* (31), 315707.
45. Ostrikov, K. K.; Levchenko, I.; Cvelbar, U.; Sunkara, M.; Mozetic, M., From nucleation to nanowires: a single-step process in reactive plasmas. *Nanoscale* **2010**, *2* (10), 2012-2027.
46. Szabó, D. V.; Schlabach, S., Microwave Plasma Synthesis of Materials—From Physics and Chemistry to Nanoparticles: A Materials Scientist’s Viewpoint. *Inorganics* **2014**, *2* (3), 468-507.
47. Kortshagen, U., Nonthermal plasma synthesis of semiconductor nanocrystals. *Journal of Physics D: Applied Physics* **2009**, *42* (11), 113001.

48. M.K. Sunkara; S. Sharma; H. Chandrasekaran; M. Talbott; K. Krogman; Bhimarasetti, a. G., Bulk Synthesis of a-SixNyH and a-SixOy Straight and Coiled Nanowires. *J. Mater. Chem* **2004**, *14*, 590-594.
49. Sharma, S.; Sunkara, M. K., Direct synthesis of gallium oxide tubes, nanowires, and nanopaintbrushes. *Journal of the American Chemical Society* **2002**, *124* (41), 12288-12293.
50. Yu, L.; O'Donnell, B.; Alet, P.-J.; Conesa-Boj, S.; Peiro, F.; Arbiol, J.; i Cabarrocas, P. R., Plasma-enhanced low temperature growth of silicon nanowires and hierarchical structures by using tin and indium catalysts. *Nanotechnology* **2009**, *20* (22), 225604.
51. Zardo, I.; Conesa-Boj, S.; Estradé, S.; Yu, L.; Peiro, F.; i Cabarrocas, P. R.; Morante, J.; Arbiol, J.; i Morral, A. F., Growth study of indium-catalyzed silicon nanowires by plasma enhanced chemical vapor deposition. *Applied Physics A* **2010**, *100* (1), 287-296.
52. Xie, X.; Zeng, X.; Yang, P.; Wang, C.; Wang, Q., < i> In situ</i> formation of indium catalysts to synthesize crystalline silicon nanowires on flexible stainless steel substrates by PECVD. *Journal of Crystal Growth* **2012**, *347* (1), 7-10.
53. Landré, O.; Songmuang, R.; Renard, J.; Bellet-Amalric, E.; Renevier, H.; Daudin, B., Plasma-assisted molecular beam epitaxy growth of GaN nanowires using indium-enhanced diffusion. *Applied Physics Letters* **2008**, *93* (18), 183109.
54. Ball, J.; Bowen, L.; Mendis, B. G.; Reehal, H., Low pressure plasma assisted silicon nanowire growth from self organised tin catalyst particles. *CrystEngComm* **2013**, *15* (19), 3808-3815.
55. Carreon, M. L.; Jasinski, J.; Sunkara, M., Low temperature synthesis of silicon nanowire arrays. *Materials Research Express* **2014**, *1* (4), 045006.
56. Zardo, I.; Yu, L.; Conesa-Boj, S.; Estradé, S.; Alet, P. J.; Rössler, J.; Frimmer, M.; i Cabarrocas, P. R.; Peiro, F.; Arbiol, J., Gallium assisted plasma enhanced chemical vapor deposition of silicon nanowires. *Nanotechnology* **2009**, *20* (15), 155602.
57. Chong, S. K.; Goh, B. T.; Aspanut, Z.; Muhamad, M. R.; Dee, C. F.; Rahman, S. A., Synthesis of indium-catalyzed Si nanowires by hot-wire chemical vapor deposition. *Materials Letters* **2011**, *65* (15), 2452-2454.
58. Meshram, N.; Kumbhar, A.; Dusane, R., Synthesis of silicon nanowires using tin catalyst by hot wire chemical vapor processing. *Materials Research Bulletin* **2013**, *48* (6), 2254-2258.
59. Rathi, S. J.; Jariwala, B. N.; Beach, J. D.; Stradins, P.; Taylor, P. C.; Weng, X.; Ke, Y.; Redwing, J. M.; Agarwal, S.; Collins, R. T., Tin-catalyzed plasma-assisted growth of silicon nanowires. *The Journal of Physical Chemistry C* **2011**, *115* (10), 3833-3839.
60. Serykh, A. I., On the formation of surface gallium hydride species in supported gallium catalysts. *Applied Surface Science* **2012**, *259*, 252-255.
61. Gonzalez, E. A.; Jasen, P. V.; Juan, A.; Collins, S. E.; Baltanás, M. A.; Bonivardi, A. L., Hydrogen adsorption on β -Ga₂O₃ (100) surface containing oxygen vacancies. *Surface science* **2005**, *575* (1), 171-180.

62. Pan, Y.-x.; Mei, D.; Liu, C.-j.; Ge, Q., Hydrogen Adsorption on Ga₂O₃ Surface: A Combined Experimental and Computational Study. *The Journal of Physical Chemistry C* **2011**, *115* (20), 10140-10146.
63. Bellitto, V.; Thoms, B.; Koleske, D.; Wickenden, A.; Henry, R., HREELS of H/GaN (0001): evidence for Ga termination. *Surface science* **1999**, *430* (1), 80-88.
64. Bellitto, V.; Thoms, B.; Koleske, D.; Wickenden, A.; Henry, R., Electronic structure of H/GaN (0001): An EELS study of Ga-H formation. *Physical Review B* **1999**, *60* (7), 4816.
65. Scott, C.; Kenny, S. D.; Storr, M. T.; Willetts, A., Modelling of dissolved H in Ga stabilised delta-Pu. *Journal of Nuclear Materials* **2013**, *442* (1-3), 83-89.
66. Angus, J. C.; Argoitia, A.; Hayman, C. C., Method for the synthesis of group iii nitride crystals. Google Patents: 1998.
67. Novikov, S.; Foxon, C., Plasma-assisted electroepitaxy of GaN layers from the liquid Ga melt. *Journal of Crystal Growth* **2012**, *354* (1), 44-48.
68. Li, H.; Chandrasekaran, H.; Sunkara, M. K.; Collazo, R.; Sitar, Z.; Stukowski, M.; Rajan, K. In *Self-oriented growth of GaN films on molten gallium*, MRS Proceedings, Cambridge Univ Press: 2004; p E11. 34.
69. Sunkara, M. K.; Sharma, S.; Chandrasekaran, H.; Talbott, M.; Krogman, K.; Bhimarasetti, G., Bulk synthesis of a-Si_xN_yH and a-Si_xO_y straight and coiled nanowires. *Journal of Materials Chemistry* **2004**, *14* (4), 590-594.
70. Mozetič, M.; Cvelbar, U.; Sunkara, M. K.; Vaddiraju, S., A method for the rapid synthesis of large quantities of metal oxide nanowires at low temperatures. *Advanced Materials* **2005**, *17* (17), 2138-2142.
71. Cvelbar, U.; Chen, Z.; Sunkara, M. K.; Mozetič, M., Spontaneous Growth of Superstructure α -Fe₂O₃ Nanowire and Nanobelt Arrays in Reactive Oxygen Plasma. *Small* **2008**, *4* (10), 1610-1614.
72. Cvelbar, U.; Ostrikov, K.; Levchenko, I.; Mozetic, M.; Sunkara, M. K., Control of morphology and nucleation density of iron oxide nanostructures by electric conditions on iron surfaces exposed to reactive oxygen plasmas. *Applied Physics Letters* **2009**, *94* (21), 211502.
73. Kumar, V.; Kim, J. H.; Jasinski, J. B.; Clark, E. L.; Sunkara, M. K., Alkali-assisted, atmospheric plasma production of titania nanowire powders and arrays. *Crystal Growth & Design* **2011**, *11* (7), 2913-2919.
74. Bhimarasetti, G.; Cowley, J. M.; Sunkara, M. K., Carbon microtubes: tuning internal diameters and conical angles. *Nanotechnology* **2005**, *16* (7), S362.
75. Bhimarasetti, G.; Sunkara, M. K.; Graham, U. M.; Davis, B. H.; Suh, C.; Rajan, K., Morphological Control of Tapered and Multi-Junctioned Carbon Tubular Structures. *Advanced Materials* **2003**, *15* (19), 1629-1632.
76. Cvelbar, U., Towards large-scale plasma-assisted synthesis of nanowires. *Journal of Physics D: Applied Physics* **2011**, *44* (17), 174014.
77. Kumar, V.; Kim, J. H.; Pendyala, C.; Chernomordik, B.; Sunkara, M. K., Gas-Phase, Bulk Production of Metal Oxide Nanowires and Nanoparticles Using a Microwave Plasma Jet Reactor. *The Journal of Physical Chemistry C* **2008**, *112* (46), 17750-17754.

78. Hatchard, T.; Dahn, J., In situ XRD and electrochemical study of the reaction of lithium with amorphous silicon. *Journal of The Electrochemical Society* **2004**, *151* (6), A838-A842.
79. Duan, X.; Huang, Y.; Agarwal, R.; Lieber, C. M., Single-nanowire electrically driven lasers. *Nature* **2003**, *421* (6920), 241-245.
80. Huynh, W. U.; Dittmer, J. J.; Alivisatos, A. P., Hybrid nanorod-polymer solar cells. *science* **2002**, *295* (5564), 2425-2427.
81. Baughman, R. H.; Cui, C.; Zakhidov, A. A.; Iqbal, Z.; Barisci, J. N.; Spinks, G. M.; Wallace, G. G.; Mazzoldi, A.; De Rossi, D.; Rinzler, A. G., Carbon nanotube actuators. *Science* **1999**, *284* (5418), 1340-1344.
82. Husain, A.; Hone, J.; Postma, H. W. C.; Huang, X.; Drake, T.; Barbic, M.; Scherer, A.; Roukes, M., Nanowire-based very-high-frequency electromechanical resonator. *Applied Physics Letters* **2003**, *83* (6), 1240-1242.
83. Huang, Y.; Duan, X.; Cui, Y.; Lauhon, L. J.; Kim, K.-H.; Lieber, C. M., Logic gates and computation from assembled nanowire building blocks. *Science* **2001**, *294* (5545), 1313-1317.
84. Johnson, J. C.; Choi, H.-J.; Knutsen, K. P.; Schaller, R. D.; Yang, P.; Saykally, R. J., Single gallium nitride nanowire lasers. *Nature materials* **2002**, *1* (2), 106-110.
85. Balandin, A. A.; Ghosh, S.; Bao, W.; Calizo, I.; Teweldebrhan, D.; Miao, F.; Lau, C. N., Superior thermal conductivity of single-layer graphene. *Nano letters* **2008**, *8* (3), 902-907.
86. (a) Martín-González, M.; Snyder, G. J.; Prieto, A. L.; Gronsky, R.; Sands, T.; Stacy, A. M., Direct Electrodeposition of Highly Dense 50 nm Bi₂Te_{3-y}Se_y Nanowire Arrays. *Nano Letters* **2003**, *3* (7), 973-977; (b) Prieto, A. L.; Martín-González, M.; Keyani, J.; Gronsky, R.; Sands, T.; Stacy, A. M., The Electrodeposition of High-Density, Ordered Arrays of Bi_{1-x}Sb_x Nanowires. *Journal of the American Chemical Society* **2003**, *125* (9), 2388-2389.
87. Kind, H.; Yan, H.; Messer, B.; Law, M.; Yang, P., Nanowire ultraviolet photodetectors and optical switches. *Advanced materials* **2002**, *14* (2), 158.
88. Lewin, M.; Carlesso, N.; Tung, C.-H.; Tang, X.-W.; Cory, D.; Scadden, D. T.; Weissleder, R., Tat peptide-derivatized magnetic nanoparticles allow in vivo tracking and recovery of progenitor cells. *Nature biotechnology* **2000**, *18* (4), 410-414.
89. Anders, S.; Toney, M.; Thomson, T.; Thiele, J.-U.; Terris, B.; Sun, S.; Murray, C., X-ray studies of magnetic nanoparticle assemblies. *Journal of applied physics* **2003**, *93* (10), 7343-7345.
90. Zhong, Z.; Qian, F.; Wang, D.; Lieber, C. M., Synthesis of p-type gallium nitride nanowires for electronic and photonic nanodevices. *Nano Letters* **2003**, *3* (3), 343-346.
91. Cui, Y.; Wei, Q.; Park, H.; Lieber, C. M., Nanowire nanosensors for highly sensitive and selective detection of biological and chemical species. *Science* **2001**, *293* (5533), 1289-1292.
92. Duan, X.; Huang, Y.; Lieber, C. M., Nonvolatile memory and programmable logic from molecule-gated nanowires. *Nano Letters* **2002**, *2* (5), 487-490.

93. Meller, A.; Nivon, L.; Brandin, E.; Golovchenko, J.; Branton, D., Rapid nanopore discrimination between single polynucleotide molecules. *Proceedings of the National Academy of Sciences* **2000**, *97* (3), 1079-1084.
94. Daiguji, H.; Yang, P.; Majumdar, A., Ion transport in nanofluidic channels. *Nano Letters* **2004**, *4* (1), 137-142.
95. Fan, R.; Wu, Y.; Li, D.; Yue, M.; Majumdar, A.; Yang, P., Fabrication of silica nanotube arrays from vertical silicon nanowire templates. *Journal of the American Chemical Society* **2003**, *125* (18), 5254-5255.
96. Garnett, E.; Yang, P., Light trapping in silicon nanowire solar cells. *Nano letters* **2010**, *10* (3), 1082-1087.
97. Chan, C. K.; Peng, H.; Liu, G.; McIlwrath, K.; Zhang, X. F.; Huggins, R. A.; Cui, Y., High-performance lithium battery anodes using silicon nanowires. *Nature nanotechnology* **2007**, *3* (1), 31-35.
98. B. Pietruzka, M. H., *Catalysis Today* **2004**, *90*.
99. Kim, H. H., *Plasma Process. Polym* **2004**, *1* (91).
100. J. Van Durme, J. D., C. Leys, H. Van Langenhove, *Appl. Catal. B: Environ* **2008**, *78* (324).
101. Y. Zhang, W. C., W. Cao, C. Luo, X. Wen, K. Zhou, *Plasma Chem. Plasma Process* **2000**, *20*.
102. X.Z. Liu, J. G. W., C.J. Liu, F. He, B. Eliasson, *React. Kinet. Catal. Lett* **2003**, *79*, 69.
103. J.G. Wang, C. J. L., Y.P. Zhang, K.L. Yu, X.L. Zhu, F. He, *Catalysis Today* **2004**, *89*.
104. X.L. Zhu, P. P. H., Y.P. Zhang, C.J. Liu, , *Ing. Eng. Chem. Res.* **2006**, *45*.
105. Z.H. Li, S. X. T., H.T. Wang, H.B. Tian, *J. Mol. Catal. A: Chem* **2004**, *211*.
106. Y.R. Zhu, Z. H. L., Y.H. Zhou, J. Lv, H.T. Wang, *React. Kinet. Catal. Lett* **2005**, *87*, 33-41.
107. Jenkinson, D. S.; Adams, D.; Wild, A., Model estimates of CO₂ emissions from soil in response to global warming. *Nature* **1991**, *351* (6324), 304-306.
108. (a) C.T. Rettner, H. E. P., H. Stein, D.J. Auerbach, *J. Vac. Sci. Technol. A.* **1988**, *6*; (b) M.B. Lee, Q. Y. Y., S.T. Ceyer, *J. Chem. Phys.* **1987**, *87*.
109. P.M. Holmblad, J. W., I. Chorkendoff, *J. Chem. Phys.* **1995**, *102*.
110. L.B.F. Juurlink, P. R. M., R. R. Smith, C.L. DiCologero, A.L. Utz, *Phys. Rev. Lett* **1999**, *83*.
111. J.H. Larsen, P. M. H., I. Chorkendoff, *J. Chem. Phys.* **1999**, *110*.
112. R.D. Beck, P. M., D.C. Papageorgopoulos, T.T. Dang, M.P. Schmid, T.R. Rizzo, *Science* **2003**, *302*.
113. J. Higgins, A. C., G. Scoles, S.L. Bernasek, *J. Chem. Phys.* **2001**, *114*.
114. Hui Wu, G. C., Jang Wook Choi, Ill Ryu, Yan Yao, Matthew T.McDowell, Seok Woo Lee, Ariel Jackson, Yuan Yang, Liangbing Hu and Yi Cui, Stable cycling of double-walled silicon nanotube battery anodes through solid–electrolyte interphase control. *Nature Nanotechnology* **2012**, *7*, 310-315.
115. Hu, J. B., Y.; Liu, Z.; Zhan, J.; Goldberg, D.; Sekiguchi, T., *Angew. Chem., Int. Ed.* **2004**, *43*, 63-66.

116. Ayyad, A.; Aqra, F., Theoretical consideration of the anomalous temperature dependence of the surface tension of pure liquid gallium. *Theoretical Chemistry Accounts* **2010**, *127* (5-6), 443-448.
117. Holmberg, V. C.; Panthani, M. G.; Korgel, B. A., Phase transitions, melting dynamics, and solid-state diffusion in a nano test tube. *Science* **2009**, *326* (5951), 405-407.
118. (a) Naechul Shin, M. C., Jane Y. Howe and Michael A. Filler, Rational Defect Introduction in Silicon Nanowires. *Nano Lett* **2013**, *13*, 1928-1933; (b) Shin, N.; Chi, M.; Howe, J. Y.; Filler, M. A., Rational Defect Introduction in Silicon Nanowires. *Nano letters* **2013**, *13* (5), 1928-1933.
119. Dhalluin, F.; Baron, T.; Ferret, P.; Salem, B.; Gentile, P.; Harmand, J.-C., Silicon nanowires: Diameter dependence of growth rate and delay in growth. *Applied Physics Letters* **2010**, *96* (13), 133109.
120. Givargizov, E., Fundamental aspects of VLS growth. *Journal of Crystal Growth* **1975**, *31*, 20-30.
121. Cui, Y.; Lauhon, L. J.; Gudixsen, M. S.; Wang, J.; Lieber, C. M., Diameter-controlled synthesis of single-crystal silicon nanowires. *Applied Physics Letters* **2001**, *78* (15), 2214-2216.
122. Seifert, W.; Borgström, M.; Deppert, K.; Dick, K. A.; Johansson, J.; Larsson, M. W.; Mårtensson, T.; Sköld, N.; Svensson, C. P. T.; Wacaser, B. A., Growth of one-dimensional nanostructures in MOVPE. *Journal of crystal growth* **2004**, *272* (1), 211-220.
123. Rudolf, D.; Storch, G.; Kaifer, E.; Himmel, H. J., Synthesis of Molecular Gallium Hydrides by Means of Low-Temperature Catalytic Dehydrogenation. *European Journal of Inorganic Chemistry* **2012**, *2012* (14), 2368-2372.
124. Zhao, J. C. L., J.P., Material for storage and production of hydrogen, and related methods and apparatus. US7833473 B2: 2010.
125. Siegel, B., Hydride formation by atomic hydrogen reactions. *Journal of Chemical Education* **1961**, *38* (10), 496.
126. Wang, Y.; Schmidt, V.; Senz, S.; Gösele, U., Epitaxial growth of silicon nanowires using an aluminium catalyst. *Nature nanotechnology* **2006**, *1* (3), 186-189.
127. Murray, J.; McAlister, A., The Al-Si (aluminum-silicon) system. *Bulletin of Alloy Phase Diagrams* **1984**, *5* (1), 74-84.
128. Ziebarth, J. T.; Woodall, J. M.; Kramer, R. A.; Choi, G., Liquid phase-enabled reaction of Al-Ga and Al-Ga-In-Sn alloys with water. *international journal of hydrogen energy* **2011**, *36* (9), 5271-5279.
129. Sobczak, N.; Sobczak, J.; Asthana, R.; Purgert, R., The mystery of molten metal. *China Foundry* **2010**, *7* (4), 425-43.
130. Bogdanović, B.; Eberle, U.; Felderhoff, M.; Schüth, F., Complex aluminum hydrides. *Scripta Materialia* **2007**, *56* (10), 813-816.
131. Schmidt, V.; Wittemann, J. V.; Senz, S.; Gösele, U., Silicon nanowires: a review on aspects of their growth and their electrical properties. *Advanced Materials* **2009**, *21* (25-26), 2681-2702.

132. Perea, D. E.; Li, N.; Dickerson, R. M.; Misra, A.; Picraux, S., Controlling heterojunction abruptness in VLS-grown semiconductor nanowires via in situ catalyst alloying. *Nano letters* **2011**, *11* (8), 3117-3122.
133. Cornils, B.; Herrmann, W. A., *Applied homogeneous catalysis with organometallic compounds*. VCH Weinheim etc.: 1996; Vol. 2.
134. Hashmi, A. S. K.; Hutchings, G. J., Gold catalysis. *Angewandte Chemie International Edition* **2006**, *45* (47), 7896-7936.
135. Arnanz, A.; Gonzalez-Arellano, C.; Juan, A.; Villaverde, G.; Corma, A.; Iglesias, M.; Sanchez, F., New chiral ligands bearing two N-heterocyclic carbene moieties at a dioxolane backbone. Gold, palladium and rhodium complexes as enantioselective catalysts. *Chemical Communications* **2010**, *46* (17), 3001-3003.
136. Corma, A.; González-Arellano, C.; Iglesias, M.; Sanchez, F., Gold nanoparticles and gold (III) complexes as general and selective hydrosilylation catalysts. *Angewandte Chemie International Edition* **2007**, *46* (41), 7820-7822.
137. Roşca, D. A.; Smith, D. A.; Hughes, D. L.; Bochmann, M., A thermally stable gold (III) hydride: synthesis, reactivity, and reductive condensation as a route to gold (II) complexes. *Angewandte Chemie International Edition* **2012**, *51* (42), 10643-10646.
138. Foster, D. W.; Learn, A. J.; Kamins, T., Deposition properties of silicon films formed from silane in a vertical-flow reactor. *Journal of Vacuum Science & Technology B* **1986**, *4* (5), 1182-1186.
139. Lew, K.-K.; Redwing, J. M., Growth characteristics of silicon nanowires synthesized by vapor-liquid-solid growth in nanoporous alumina templates. *Journal of Crystal Growth* **2003**, *254* (1), 14-22.
140. Lugstein, A.; Steinmair, M.; Hyun, Y. J.; Bertagnolli, E.; Pongratz, P., Ga/Au alloy catalyst for single crystal silicon-nanowire epitaxy. *Applied physics letters* **2007**, *90* (2), 3109.
141. Ke, Y.; Weng, X.; Redwing, J. M.; Eichfeld, C. M.; Swisher, T. R.; Mohny, S. E.; Habib, Y. M., Fabrication and Electrical Properties of Si Nanowires Synthesized by Al Catalyzed Vapor-Liquid-Solid Growth. *Nano letters* **2009**, *9* (12), 4494-4499.
142. Shih, W.-H.; Stroud, D., Theory of the surface tension of liquid metal alloys. *Physical Review B* **1985**, *32* (2), 804.
143. Kaye, G. W. C.; Laby, T. H., *Tables of physical and chemical constants: and some mathematical functions*. Longmans, Green and Company: 1921.
144. Molina, J.; Voytovich, R.; Louis, E.; Eustathopoulos, N., The surface tension of liquid aluminium in high vacuum: the role of surface condition. *International journal of adhesion and adhesives* **2007**, *27* (5), 394-401.
145. Civale, Y.; Nanver, L.; Hadley, P.; Goudena, E., Aspects of silicon nanowire synthesis by aluminum-catalyzed vapor-liquid-solid mechanism. *catalyst* **2004**, *4* (2), 2.
146. Martin, R. M., *Electronic structure: basic theory and practical methods*. Cambridge university press: 2004.
147. Hohenberg, P.; Kohn, W., Inhomogeneous electron gas. *Physical review* **1964**, *136* (3B), B864.
148. Kohn, W.; Sham, L., *J. Phys. Rev. A* **1965**, *140*, 1133-1138.

149. Kresse, G.; Furthmüller, J., Efficiency of ab-initio total energy calculations for metals and semiconductors using a plane-wave basis set. *Computational Materials Science* **1996**, *6* (1), 15-50.
150. Perdew, J. P., Density-functional approximation for the correlation energy of the inhomogeneous electron gas. *Physical Review B* **1986**, *33* (12), 8822.
151. Kresse, G.; Hafner, J., Norm-conserving and ultrasoft pseudopotentials for first-row and transition elements. *Journal of Physics: Condensed Matter* **1994**, *6* (40), 8245.
152. Csonka, S.; Halbritter, A.; Mihály, G., Pulling gold nanowires with a hydrogen clamp: Strong interactions of hydrogen molecules with gold nanojunctions. *Physical Review B* **2006**, *73* (7), 075405.
153. Wood, B. J.; Wise, H., THE KINETICS OF HYDROGEN ATOM RECOMBINATION ON PYREX GLASS AND FUSED QUARTZ1. *The Journal of Physical Chemistry* **1962**, *66* (6), 1049-1053.
154. Otorbaev, D.; Van de Sanden, M.; Schram, D., Heterogeneous and homogeneous hydrogen kinetics in plasma chemistry. *Plasma Sources Science and Technology* **1995**, *4* (2), 293.
155. Tarascon, J.-M.; Armand, M., Issues and challenges facing rechargeable lithium batteries. *Nature* **2001**, *414* (6861), 359-367.
156. Beaulieu, L. Y., Eberman, K.W., Turner, R. L., Krause, L. J. & Dahn, J. R., Colossal reversible volume changes in lithium alloys. *Electrochem. Solid State Lett.* **2001**, *4*, A137-A140.
157. Besenhard, J. O., Yang, J. & Winter, M., Will advanced lithium-alloy anodes have a chance in lithium-ion batteries? *J. Power Sources* **1997**, *68*, 87-90.
158. (a) Hatchard, T. D. D., J. R., In situ XRD and electrochemical study of the reaction of lithium with amorphous silicon. *T. D. Hatchard and J. R. Dahn* **2004**, *151*, A838-A842; (b) Weydanz, W. J., Wohlfahrt-Mehrens, M. & Huggins, R. A., A room temperature study of the binary lithium-silicon and the ternary lithium-chromium-silicon system for use in rechargeable lithium batteries. *J. Power Sources* **1999**, *81*, 237-242.
159. Verbrugge, M. W. C., Y. T., Stress and strain-energy distributions within diffusion-controlled insertion-electrode particles subjected to periodic potential excitations. *J. Electrochem. Soc.* **2009**, *156*, A927-A937.
160. Cheng, Y. T. V., M. W., The influence of surface mechanics on diffusion induced stresses within spherical nanoparticles. *J. Appl. Phys.* **2008**, *104*.
161. Graetz, J.; Ahn, C.; Yazami, R.; Fultz, B., Highly reversible lithium storage in nanostructured silicon. *Electrochemical and Solid-State Letters* **2003**, *6* (9), A194-A197.
162. Kim, H., Han, B., Choo, J. & Cho, J., Three-dimensional porous silicon particles for use in high-performance lithium secondary batteries. *Angew. Chem. Int. Ed* **2008**, *47*, 10151-10154.
163. Cui, L. F., Yang, Y., Hsu, C. M. & Cui, Y., Carbon-silicon core-shell nanowires as high capacity electrode for lithium ion batteries. *Nanoletters* **2009**, *9*, 3370-3374.
164. Beaulieu, L.; Eberman, K.; Turner, R.; Krause, L.; Dahn, J., Colossal reversible volume changes in lithium alloys. *Electrochemical and Solid-State Letters* **2001**, *4* (9), A137-A140.

165. Takamura, T.; Ohara, S.; Uehara, M.; Suzuki, J.; Sekine, K., A vacuum deposited Si film having a Li extraction capacity over 2000 mAh/g with a long cycle life. *Journal of Power Sources* **2004**, *129* (1), 96-100.
166. Chen, L.; Xie, J.; Yu, H.; Wang, T., An amorphous Si thin film anode with high capacity and long cycling life for lithium ion batteries. *Journal of Applied Electrochemistry* **2009**, *39* (8), 1157-1162.
167. Zhao, X.; Hayner, C. M.; Kung, M. C.; Kung, H. H., In-Plane Vacancy-Enabled High-Power Si-Graphene Composite Electrode for Lithium-Ion Batteries. *Advanced Energy Materials* **2011**, *1* (6), 1079-1084.
168. Chan, C. K.; Peng, H.; Liu, G.; McIlwrath, K.; Zhang, X. F.; Huggins, R. A.; Cui, Y., High-performance lithium battery anodes using silicon nanowires. *Nature nanotechnology* **2008**, *3* (1), 31-35.
169. Street, R. A., *Hydrogenated amorphous silicon*. Cambridge University Press: 2005.
170. Jayaprakash, N.; Kalaiselvi, N.; Doh, C., A new class of tailor-made Fe 0.92 Mn 0.08 Si 2 lithium battery anodes: Effect of composite and carbon coated Fe 0.92 Mn 0.08 Si 2 anodes. *Intermetallics* **2007**, *15* (3), 442-450.
171. Nguyen, H. T.; Yao, F.; Zamfir, M. R.; Biswas, C.; So, K. P.; Lee, Y. H.; Kim, S. M.; Cha, S. N.; Kim, J. M.; Pribat, D., Highly Interconnected Si Nanowires for Improved Stability Li-Ion Battery Anodes. *Advanced Energy Materials* **2011**, *1* (6), 1154-1161.
172. Chan, C. K.; Patel, R. N.; O'Connell, M. J.; Korgel, B. A.; Cui, Y., Solution-grown silicon nanowires for lithium-ion battery anodes. *ACS nano* **2010**, *4* (3), 1443-1450.
173. Park, M.-H.; Kim, M. G.; Joo, J.; Kim, K.; Kim, J.; Ahn, S.; Cui, Y.; Cho, J., Silicon nanotube battery anodes. *Nano Letters* **2009**, *9* (11), 3844-3847.
174. Cheng, Y.-T.; Verbrugge, M. W., The influence of surface mechanics on diffusion induced stresses within spherical nanoparticles. *Journal of Applied Physics* **2008**, *104* (8), 083521.
175. Hu, G.; O'Connell, R.; He, Y.; Yu, M., Electronic conductivity of hydrogenated nanocrystalline silicon films. *Journal of applied physics* **1995**, *78* (6), 3945-3948.
176. Kawai, Y.; Ikegami, H.; Sato, N.; Matsuda, A.; Uchino, K., *Industrial Plasma Technology: Applications from Environmental to Energy Technologies*. John Wiley & Sons: 2010.
177. Kaneko, T.; Wakagi, M.; Onisawa, K. i.; Minemura, T., Change in crystalline morphologies of polycrystalline silicon films prepared by radio-frequency plasma-enhanced chemical vapor deposition using SiF₄+ H₂ gas mixture at 350 C. *Applied physics letters* **1994**, *64* (14), 1865-1867.
178. Li, H. H., X.; Chen, L.; Zhou, G.; Zhang, Z.; Yu, D.; Jun Mo, Y.; Pei, N. , *Solid State Ionics* **2000**, *135*, 181-191.
179. Limthongkul, P. J., Y. I.; Dudney, N. J.; Chiang, Y. M. , *Acta Mater.* **2003**, *51*, 1103-1113.
180. Bao, Z.; Weatherspoon, M. R.; Shian, S.; Cai, Y.; Graham, P. D.; Allan, S. M.; Ahmad, G.; Dickerson, M. B.; Church, B. C.; Kang, Z., Chemical reduction of three-

- dimensional silica micro-assemblies into microporous silicon replicas. *Nature* **2007**, *446* (7132), 172-175.
181. Magasinski, A.; Zdyrko, B.; Kovalenko, I.; Hertzberg, B.; Burtovyy, R.; Huebner, C. F.; Fuller, T. F.; Luzinov, I.; Yushin, G., Toward efficient binders for Li-ion battery Si-based anodes: polyacrylic acid. *ACS applied materials & interfaces* **2010**, *2* (11), 3004-3010.
182. Kovalenko, I.; Zdyrko, B.; Magasinski, A.; Hertzberg, B.; Milicev, Z.; Burtovyy, R.; Luzinov, I.; Yushin, G., A major constituent of brown algae for use in high-capacity Li-ion batteries. *Science* **2011**, *334* (6052), 75-79.
183. Kim, H.; Seo, M.; Park, M. H.; Cho, J., A Critical Size of Silicon Nano-Anodes for Lithium Rechargeable Batteries. *Angewandte Chemie International Edition* **2010**, *49* (12), 2146-2149.
184. Gao, P.; Fu, J.; Yang, J.; Lv, R.; Wang, J.; Nuli, Y.; Tang, X., Microporous carbon coated silicon core/shell nanocomposite via in situ polymerization for advanced Li-ion battery anode material. *Physical Chemistry Chemical Physics* **2009**, *11* (47), 11101-11105.
185. Liu, N.; Wu, H.; McDowell, M. T.; Yao, Y.; Wang, C.; Cui, Y., A yolk-shell design for stabilized and scalable Li-ion battery alloy anodes. *Nano letters* **2012**, *12* (6), 3315-3321.
186. Ge, M.; Fang, X.; Rong, J.; Zhou, C., Review of porous silicon preparation and its application for lithium-ion battery anodes. *Nanotechnology* **2013**, *24* (42), 422001.
187. Park, J.; Kim, G.-P.; Nam, I.; Park, S.; Yi, J., One-pot synthesis of silicon nanoparticles trapped in ordered mesoporous carbon for use as an anode material in lithium-ion batteries. *Nanotechnology* **2013**, *24* (2), 025602.
188. Song, T.; Xia, J.; Lee, J.-H.; Lee, D. H.; Kwon, M.-S.; Choi, J.-M.; Wu, J.; Doo, S. K.; Chang, H.; Park, W. I., Arrays of sealed silicon nanotubes as anodes for lithium ion batteries. *Nano Letters* **2010**, *10* (5), 1710-1716.
189. Wu, H.; Chan, G.; Choi, J. W.; Yao, Y.; McDowell, M. T.; Lee, S. W.; Jackson, A.; Yang, Y.; Hu, L.; Cui, Y., Stable cycling of double-walled silicon nanotube battery anodes through solid-electrolyte interphase control. *Nature nanotechnology* **2012**, *7* (5), 310-315.
190. Cui, L.-F.; Yang, Y.; Hsu, C.-M.; Cui, Y., Carbon– silicon core– shell nanowires as high capacity electrode for lithium ion batteries. *Nano Letters* **2009**, *9* (9), 3370-3374.
191. Carreon, M. L.; Thapa, A. K.; Jasinski, J. B.; Sunkara, M. K., The Capacity and Durability of Amorphous Silicon Nanotube Thin Film Anode for Lithium Ion Battery Applications. *ECS Electrochemistry Letters* **2015**, *4* (10), A124-A128.
192. Tanaka, S.; Uyama, H.; Matsumoto, O., Synergistic effects of catalysts and plasmas on the synthesis of ammonia and hydrazine. *Plasma Chemistry and Plasma Processing* **1994**, *14* (4), 491-504.
193. Kiyooka, H.; Matsumoto, O., Reaction scheme of ammonia synthesis in the ECR plasmas. *Plasma chemistry and plasma processing* **1996**, *16* (4), 547-562.
194. Uyama, H.; Nakamura, T.; Tanaka, S.; Matsumoto, O., Catalytic effect of iron wires on the syntheses of ammonia and hydrazine in a radio-frequency discharge. *Plasma chemistry and plasma processing* **1993**, *13* (1), 117-131.

195. Nomura, O.; Oyama, H.; Sakamoto, Y. In *Ammonia synthesis exploiting a plasma-wall interaction*, Proceedings of the international ion engineering congress, Kyoto, Japan, 1983; pp 1481-4.
196. Mizushima, T.; Matsumoto, K.; Ohkita, H.; Kakuta, N., Catalytic effects of metal-loaded membrane-like alumina tubes on ammonia synthesis in atmospheric pressure plasma by dielectric barrier discharge. *Plasma Chemistry and Plasma Processing* **2007**, 27 (1), 1-11.
197. Studt, F.; Sharafutdinov, I.; Abild-Pedersen, F.; Elkjær, C. F.; Hummelshøj, J. S.; Dahl, S.; Chorkendorff, I.; Nørskov, J. K., Discovery of a Ni-Ga catalyst for carbon dioxide reduction to methanol. *Nature chemistry* **2014**.

CURRICULUM VITAE

Maria L. Carreon

Assistant Professor

Russell School of Chemical Engineering

University of Tulsa. Tulsa, OK 74104

Office: 918-631-2424

Email: maria-carreon@utulsa.edu

Nationality: Mexican

Educational Background and Professional Experience

2010-2015. PhD in Chemical Engineering. (GPA 3.5/4.0)

University of Louisville, US.

Thesis Title: *“Plasma Catalysis using low melting point metals”*

2008-2010. MS in Chemical Engineering. (GPA 3.8/4.0).

Universidad Michoacana, MEXICO.

Thesis Title: *“Nanocrystalline Mesoporous Titania Catalysts for the selective oxidation of benzyl alcohol to benzaldehyde”*

2002-2007. BS in Chemical Engineering (GPA 3.6/4.0).

Universidad Michoacana, MEXICO.

Thesis Title: *“Measurement of the thermoelectric potential coefficient for the characterization of the anisotropy of Ti-6Al-4V samples”*

Fellowships, Honors and Awards

Fall 2014-Spring 2015. Academic Scholarship. Society of Hispanic Professional Engineers (SHPE) Foundation.

Fall 2014-Spring 2015. Tuition Award. University of Louisville School of Interdisciplinary and Graduate Studies.

2014-2015. Hispanic Engineer Graduate Student Ambassador. SHPE-UofL chapter.

2014-2015. SHPE-UofL chapter vice-president.

2014. Spring 2014 Grant Writing Academy. School of Interdisciplinary and Graduate Studies (SIGS) and Arts and Sciences Research (January-April).

2013-2015. Conn Center Fellowship.

2012-Present. RE3 Renewable Energy Club Communications Officer.

2011. Recognition for outstanding Academic Accomplishment. UofL Chapter of the Society of Hispanic Professional Engineers (SHPE). (April)

2011. Kokes Award. 22th North American Catalysis Society Meeting. Detroit, MI. (June)

2008-2010. CONACYT Fellowship award to pursue MS studies.

2009. Best Poster Presentation Award. 6th Materials Science Engineering Forum. Material Research Institute, MEXICO. (December)

2009. Kokes Award. 21th North American Catalysis Society Meeting. San Francisco, California. (June)

2009. Santander Fellowship award to pursue a research stay at the UAeMEX-UNAM, Toluca, MEXICO. (February-July)

2007-2008. CONACYT Fellowship award as Undergraduate Research Assistant in the Project "Non Destructive Techniques for the Detection of defects in metals by magnetic sensing"

2007. UNAM Fellowship award to pursue a research stay at the IIM, UNAM Campus Morelia, MEXICO. (October)

2004. French Embassy Fellowship “Decouverte de la France”, Paris and L’Auvergne, FRANCE. (July-August)

2004. Best undergraduate student class 2003-2004. Universidad Michoacana, MEXICO. (May)

2002. Chemistry Olympiad State Award. Third Place. XI Chemistry Olympiad State Competition, Michoacan, MEXICO.

Refereed Publications

1. Carreon, Maria L., et al., Photocatalytic degradation of organic dyes by mesoporous nanocrystalline anatase. *Materials Chemistry and Physics* **2011**. 125(3), 474-478.
2. Carreon, Maria L., S.G. Li, and M.A. Carreon, ALPO-18 membranes for CO₂/CH₄ separation. *Chemical Communications*, **2012**. 48(17), 2310-2312.
3. Carreon, Maria L., Jasinski, J.B. and Sunkara, M. K. Low temperature synthesis of silicon nanowire arrays. *Mater. Res. Express*, **2014** (1), 1-14.
4. Carreon, Maria L., Thapa, Arjun K., Jasinski, Jacek B. Sunkara, Mahendra K. The capacity and durability of silicon nanotube thin film anode for lithium ion battery applications. *ECS Electrochemistry Letters*, **2015**, 4 (10) A124-A128.
5. Carreon, Maria L., Indira Chaudhuri and Mahendra K. Sunkara. The interaction of H₂ and N₂ with molten Gallium in the presence of plasma. (*in preparation*).

Conference Proceedings

Maria L. Carreon, Jacek Jasinski and Mahendra K. Sunkara. “Synthesis of Silicon Nanowires Using Ga as Catalyst”. 23rd North American Meeting of the Catalysis Society. Louisville, Kentucky. June 2-7, 2013.

Maria L. Carreon, Jacek Jasinski and Mahendra K. Sunkara. “Low temperatura Synthesis of Si Nanowires Arrays”. 2012 MRS Fall Meeting. Boston Massachusetts. November 25-30, 2012

Maria L. Carreon, Moises A. Carreon and Paul Ratnasamy. "Synthesis and characterization of Zeolitic Imidazolate Framework-8 by Evaporation Induced Self Assembly". 22nd North American Catalysis Society Meeting. Detroit, MI. June 5-10, 2011.

Maria L. Carreon et al. "Catalytic Processes to clean water" Proc. XXXI AMIDIQ National Meeting. ISBN 978-1-4020-8741-7. Oaxaca, MEXICO. May 2010.

Maria L. Carreon et al. "TiO₂ mesostructured Catalysts for dyes degradation". Proc. Materials Science and Engineering Forum. Vol. 6. (2009). 102-107. ISBN 970-9798-05-7. Morelia, MEXICO. December 2009.

Maria L. Carreon, Jaime Espino and Moises A. Carreon. "Titania mesostructured catalysts for the selective oxidation of benzyl alcohol to benzaldehyde." 21st North American Meeting of the Catalysis Society. San Francisco, California. June 7-12, 2009.

Maria L. Carreon et al. "Titania mesostructured catalysts". Proc. Materials Science and Engineering Forum. Vol. 5. (2008). 18-22. ISBN 970-9798-04-9. Morelia, MEXICO. December 2008.

Maria L. Carreon et al. "Mesostructured Titania: Synthesis and Characterization" Proc. IX National Microscopy Congress. Guanajuato, MEXICO. November 2008.

Maria L. Carreon et al. "Characterization of plastic deformation by magnetic sensing". Proc. 3rd State Congress of Science and Technology. Morelia, MEXICO. October 2007.

Maria L. Carreon et al. "Texture Characterization of Ti-6Al-4V samples cold rolled by magnetic sensing". Proc. XXVIII AMIDIQ National Meeting. ISBN 978-970-764-267-6. Colima, MEXICO. May 2004.

Languages

English, Spanish and French (Full command)

2001. Diplome d'Etudes en Langue Francaise (DELF) 1er Degre.

2003. Diplome d'Etudes en Langue Francaise (DELF) 2eme Degre.

Experimental Skills

Experience using gas permeation system, PECVD reactor, GC-MS, SEM, XRD, FTIR, UV-vis, HRTEM, Raman, BET, NIR Spectroscopy, Sputtering, Atomic Layer Deposition, Glove box, Battery tester system.

Teaching Experience

2004-2005. French Instructor at Alliance Francaise, Mexico.

Spring 2012. Transport Phenomena. Chemical Engineering Department. University of Louisville.

Fall 2013-Summer 2014. Analytical Chemistry Instructor. Chemistry Department, University of Louisville.

Spring 2015. Chemical Vapor Deposition. Chemical Engineering Department. University of Louisville.

Fall 2015. Co-teach ES 3073 Heat Transfer. Chemical Engineering Department. University of Tulsa.